Citywide Measurements of Nitrogen Dioxide (NO$_2$) Using a Combination of Remote Sensing and In-situ Measurement Techniques

Ying Zhu

München, 2018

Citywide Measurements of Nitrogen Dioxide (NO₂) Using a Combination of Remote Sensing and In-situ Measurement Techniques

Stadtweite Messungen von Stickstoffdioxid (NO₂) mit einer Kombination aus Fernerkundung und In-situ-Messverfahren

Dissertation an der Fakultät für Physik
der Ludwig-Maximilians-Universität München

vorgelegt von

Ying Zhu

aus Wuhan, China

München, Aug. 2018

Erstgutachter: Prof. Dr. Mark Wenig

Zweitgutachter: Prof. Dr-ing. Jia Chen

Datum der Abgabe: 01.08.2018

Datum der mündlichen Prüfung: 05.10.2018

Kurzfassung

Die hohen NO_2-Werte wurden weltweit in Städten beobachtet und können negative Auswirkungen auf die menschliche Gesundheit haben. Da sich die NO_2-Konzentration schnell mit der Zeit ändert und eine sehr starke räumlich-zeitliche Variabilität aufweist, ist es wichtig, ihre Verteilung zu verstehen. Diese Arbeit zielt darauf ab, die räumliche und zeitliche Verteilung von NO_2 mit mehreren optischen Differenzabsorptionsspektroskopie-Instrumenten (DOAS) zu untersuchen, um die Verschmutzungs-Hotspots zu identifizieren und eine langfristige Bodenbeobachtung durchzuführen, die mit Satellitendaten verglichen werden kann.

Um die räumliche und zeitliche Variabilität der Straßenniveaukonzentrationen von NO_2 zu untersuchen, wurde ein Messsystem etabliert, das Fernerkundung und In-situ-Mess techniken kombiniert. Diese Studie wurde in München und Hongkong durchgeführt, die beide dicht besiedelte Städte mit hohem Verkehrsaufkommen sind. Mit dieser Kombinationstechnik wurde ein neuer Algorithmus entwickelt, der zeitliche Veränderungen und räumliche Muster trennen und unabhängig voneinander analysieren kann. Konkret wurden Tageszyklen, wöchentliche Muster sowie ortsaufgelöste Langzeitveränderungen untersucht, um das Quellmuster auf verschiedenen Zeitskalen zu untersuchen. Zwei Messkampagnen wurden durchgeführt, eine im Juni und Juli 2016 in München und eine im März 2017 in Hongkong. Die Daten der Hongkonger Messkampagne im Dezember 2010 wurden ebenfalls analysiert. Mobile Messungen wurden während des Tages durchgeführt, um die Nicht-Stoßzeiten, die Stoßzeiten morgens und abends abzudecken. Um räumliche Muster zu vergleichen, wurde die Akkumulation von NO_2, die beim Anhalten an Ampeln gemessen wurde, herausgefiltert. Auf diese Weise konzentriert sich diese Arbeit auf die Änderungen der räumlichen Verteilung von NO_2, anstatt Verkehrsflussmuster zu vergleichen. Für die Erzeugung von zusammengesetzten Karten wurde der Tageszyklus normalisiert, indem die mobilen Daten mit übereinstimmenden stadtweiten, pfadgemittelten Messungen skaliert wurden.

In dieser Studie wurden mehrere Datensätze verwendet, einschließlich der OMI-Satelliten daten und der lokalen stationären Überwachungsdaten. Die Münchner Langzeit-LP-DOAS-Daten der monatlichen Durchschnitts- und Satellitenmessungen waren beim Vergleich der Daten der OMI-Überführungszeit gut korreliert. Bei der Ermittlung von Umwelt verschmutzungsschwerpunkten in München waren die On-Road-Konzentrationen von NO_2 auf Autobahnen und in der Innenstadt wesentlich höher als im übrigen Gebiet. Das NO_2-Niveau und die Verkehrszählungsdaten, die vom Kreisverwaltungsreferat (KVR) in München angeboten wurden, zeigten eine ähnliche Reduzierung am Wochenende während der Hauptverkehrszeiten. Die mit Auto-Multi-AXis (MAX) DOAS und dem Satelliten OMI gemessene Säulendichte von NO_2 zeigte eine vergleichbare räumliche Verteilung, die in der Innenstadt ein höheres Niveau aufwies. In Hongkong wurden ausgeprägte räumliche Strukturen in Langzeit-Differenzkarten beobachtet, die in den meisten gemessenen Bereichen einen abnehmenden Trend von NO_2 aufwiesen, mit Ausnahme eines zunehmenden Trends in der Umgebung von U-Bahnhöfen. Die Analyse des Wochenend-Effekts zeigte, dass die NO_2-Werte in den meisten Teilen von Hongkong an Sonntagen deutlich reduziert waren, während in Shopping-Malls ein gegensätzlicher Trend festgestellt wurde.

Als weitere Implikationen müssen bei der Diskussion stadtweiter Trends die räumlichen Unterschiede berücksichtigt und lokale Punktmessungen relativiert werden. Die visualisierten Datensätze können einen besseren Einblick in die NO_2-Eigenschaften von Straßen in München und Hongkong geben, was zur Identifizierung stark verschmutzter Gebiete beiträgt und eine nützliche Datenbank für die Stadtplanung und die Planung von Umweltschutzmaßnahmen darstellt.

Abstract

The high NO_2 levels have been observed worldwide in cities and can have negative influence on human health. Since NO_2 concentration changes rapidly with time and has a very strong spatio-temporal variability, it is vital to understand its distribution. This work aims to investigate the spatial and temporal distribution of NO_2 using multiple Differential Optical Absorption Spectroscopy (DOAS) instruments so as to identify the pollution hotspots and have a long-term ground observation that could be compared with satellite data.

In order to look into the spatial and temporal variability of street level concentrations of NO_2, a measuring system was established combining open path remote sensing and in-situ measurement techniques. This study was implemented in Munich and Hong Kong, which are both densely populated cities with a high volume of traffic. With this combination technique, a new algorithm was developed which allowed to separate temporal changes and spatial patterns and analyze them independently. Specifically, diurnal cycles, weekly patterns as well as spatially resolved long term changes were examined in order to study the source patten on different time scales. Two measurement campaigns have been conducted, one in June and July 2016 in Munich and one in March 2017 in Hong Kong. The data of the Hong Kong measurement campaign in December 2010 was also analyzed. Mobile measurements were performed during the daytime to cover non-rush hours, morning and evening rush hours. To compare spatial patterns, the accumulation of NO_2 measured when stopping at traffic lights was filtered out. In this way, this work focuses on the changes of NO_2 spatial distribution instead of comparing traffic flow patterns. For the generation of composite maps, the diurnal cycle has been normalized by scaling the mobile data with coinciding citywide path-averaged measurements.

Several data sets were used in this study including the Ozone Monitoring Instrument (OMI) satellite data and the local stationary monitoring data. The Munich long-term LP DOAS data of monthly average and satellite measurements were well correlated when comparing the data of the OMI overpass time. For identifying pollution hotspots in Munich, on-road concentrations of NO_2 were much higher on motorways and the city center than the rest of the area. The NO_2 level and the traffic count data offered by the Department of Public Order (KVR) of Munich showed similar weekend reduction during rush hour peaks. The column density of NO_2 measured by car-based Multi-AXis (MAX) DOAS and the satellite OMI observed comparable spatial distribution which displayed a higher level in the city center. In Hong Kong, pronounced spatial structures were observed in long-term difference maps, which exhibited a decreasing trend of NO_2 in most measured areas except an increasing trend around subway stations. Analysis of the weekend effect showed that NO_2 levels for most part of Hong Kong were significantly reduced on Sundays, whereas an opposite trend was revealed around shopping malls.

As further implications, the spatial differences have to be considered when discussing city-wide trends and can be used to put local point measurements into perspective. The visualized data sets can provide a better insight into on-road NO_2 characteristics in Munich and Hong Kong, which helps to identify heavily polluted areas and represents a useful database for urban planning and the design of pollution control measures.

Contents

Contents

1 Introduction

The Earth's atmosphere is an approximately 100 km thick layer of gases surrounded mainly by nitrogen (78 %) and oxygen (21 %). The mixture of different gases like oxygen, carbon dioxide and water vapor creates a warm climate and supports life on Earth. Despite that the atmosphere has natural variations over the past centuries, human activities especially the development of industrialization have a pronounced impact on the composition of tropospheric aerosols. Air pollutants released into the atmosphere have been causing abundant changes such as ozone holes, acid rain and global warming (Crutzen and Arnold, 1986; Likens et al., 1996; Cox et al., 2000). These changes have upset the balance of nature and could lead to unpredictable and serious consequences on the health of most plants, animals, and humans (Seinfeld and Pandis, 2012). Therefore, more and more researchers are motivated to study the physical and chemical processes of the atmosphere changes. The research efforts to understand the anthropogenic influence on the atmosphere and plants have been increasing rapidly over the past few decades.

The urban air quality is of great social concern and attracts particular attention since the famous 'Great smog of London' episode occurred in early December 1952. It was mainly caused by serious particulate matter emissions and high photochemical oxidation of SO_2 emitted from combustion sources, which indirectly lead to around 4000 excess deaths in London within 4 days (Wilkins, 1954; Lodge et al., 1969; Finlayson-Pitts and Pitts Jr, 1999a). The Los Angeles and the San Joaquin Valley are notorious for their smog which is primarily due to photochemical formation of large amounts of ozone, carbonyl compounds, and organic aerosol from car exhausts and industrial emissions of nitrogen oxides, carbon monoxide, and volatile organic compounds (VOCs) (Haagen-Smit, 1952; Finlayson-Pitts and Pitts Jr, 1999b; Warneke et al., 2012). As mentioned above, there are other numerous examples indicating the impacts of the emission and transformation of gases on the atmosphere. Developing countries like India and China continue to experience high levels of air pollution, as a result of rapid industrial growth and weak environmental regulation.

1.1 Nitrogen dioxides in the atmosphere

Nitrogen oxides (NO_x), defined as the sum of nitric oxide (NO) and nitrogen dioxide (NO_2), is released into the atmosphere from both natural and anthropogenic sources. On a global scale, the contributions of natural and anthropogenic NO_x sources are about equal in magnitude (Logan, 1983; Zhang et al., 2003a). Major NO_x sources include fossil fuel combustion, biomass burning, lightning and oxidation of ammonia (Bond et al., 2001; Zhang et al., 2003b). NO_x has a strong influence on the atmospheric level of hydroxyl

radicals (OH) in terms of being responsible for the oxidation processes of most trace gases. For instance, VOC degradation products can react with NO_x and form organic nitrates or nitrites (e.g. peroxy acetyl nitrate (PAN) or methyl nitrite), which are more detrimental to human health than the primary oxides of nitrogen. Hence, observing and controlling the emission level of the primary oxides of nitrogen are vital solutions to report and govern the air pollution by trace gases.

NO_2 is one of the major air pollutants from combustion processes which can be stationary or mobile. It plays a key role in both tropospheric and stratospheric chemistry. It participates in the catalytic formation of tropospheric ozone (O_3), contributes to the formation of secondary aerosols (Jang and Kamens, 2001; Huang et al., 2014) and causes acid rain as well. Atmospheric NO_2 in high concentration is known to be toxic to humans. With regards to urban environments, traffic emission is always one of the major sources of air pollution, particularly NO_x. NO accounts for the majority of direct traffic emission which is subsequently oxidized to form NO_2, although some NO_2 is emitted directly (Kirchstetter et al., 1999; Henderson et al., 2007; Ban-Weiss et al., 2008). NO_2 level is often strongly correlated with those of other toxic pollutants. Its concentration can be easily and precisely measured which is helpful to induce a brief assessment about the general air quality. In addition, it is a short-lived species with a strong local character and concentrations that can vary strongly, both in space and time. It also changes with weather patterns that may change the transport, dispersion, deposition and formation of air pollutants in the atmosphere.

1.2 The importance of measurements

For studying about the physical and chemical processes in the atmosphere and the relationship between global and regional air quality, measurements of weather conditions (e.g. pressure, temperature, humidity, wind speed and so on), trace gases mixing ratios(e.g. ozone(O_3), carbon dioxide (CO_2), NO_x and so on) and other relevant parameters are essential approaches to gather information. In this thesis, we focus on the study of trace gases especially NO_2 concentrations and quantities in the atmosphere with the aim of monitoring long-term NO_2 gradual changes and analyzing regional pollution distribution.

1.2.1 Observation methods

Common measurement methods can be characterized by temporal and spatial scales. For instance, long-term observation is applied to follow the evolution of chemical changes; measurement campaigns as regional and episodic studies seek to investigate certain cases of air pollution; whereas in-situ investigation with a high time-resolution mainly aims to capture local, regional or global scale phenomena.

Long-term observations become necessary considering the notable changes in weather conditions. The changes of composition of our atmospheric environment has been observed for a long time. According to the measurement data from the Mauna Loa Observatory of National Oceanic atmospheric Administration (NOAA)(Keeling et al., 1976; NOAA,

2018), the portion of global CO_2 in the atmosphere keeps rising since the 1950s (Malhi and Grace, 2000; Baldocchi et al., 2001). Additionally, a steady decline of the total amount of ozone have been observed in 1975 by the World Meteorological Organization (WMO) and the stratospheric ozone depletion has become a new issue of atmosphere science. Therefore, long-term observations are frequently used for monitoring trends of stratospheric and global tropospheric trace gases.

In addition, air pollution by anthropogenic activities mostly has regional characteristics. For studying and capturing these diversities, episodic studies combined with high time resolution in-situ measurements are widely applied to investigate the causes and consequences of regional air pollution. For example, many studies that focus on the impact of 2008 Beijing Olympic Games on the atmosphere environments included studying trends of O_3 and greenhouse gases (Wang et al., 2009b, 2010), species of particular matters (Huang et al., 2010b), compositions of aerosols (Zhang et al., 2009c; Guo et al., 2013), on-road emissions (Wang et al., 2009a; Wang and Xie, 2009) and so on.

This PhD work mainly focuses on the urban NO_2 distribution which combined all three measurement methods in order to comprehensively monitoring the urban NO_2 environment and provide a consistent city NO_2 distribution map. Two cities, Munich, Germany, and Hong Kong, China, were selected as study areas. The measurement data avaliable online by each city environmental monitoring station network were used for comparison.

1.2.2 Previous NO_2 measurements

With the growing knowledge of atmosphere science and the development of technology, stationary monitoring networks are established in many countries. Most monitoring stations utilize the ChemiLuminescence (CL) technique for NO_x measurements. The NO_2 concentration is determined indirectly by calculating the difference between NO_x and NO concentrations. For the NO_x measurement, it firstly converts the NO_2 in the gas sample to NO by a molybdenum converter. Then NO in the gas sample reacts with O_3 (generated by an O3 generator) to generate excited state of NO_2. The NO_x concentration can be determined by measuring the CL radiation emitted by the excited NO_2. Similar procedure is applied for the NO measurement except for converting the NO_2 in the sample air at the beginning. The advantage of CL technique is the low background emission which could avoid the noise caused by light scattering. However, the sensor has relatively short lifetime and the signals are affected by the consumption of CL reagents (Knight and Greenway, 1994; Zhang et al., 2005). According to lots of previous research studies and reports, e.g. Barker et al. (1961); Lawther et al. (1962); Katz et al. (1969), about the relationship between human health and air pollutants, the Air Quality Guideline (AQG) of World Health Organization (WHO) has been first published in 1987 as reference tools for air quality management. In addition, the latest edition (Krzyzanowski and Cohen, 2008) recommends NO_2 concentration upper limits of 40 $\mu g/m^3$ (≈ 19.5 ppbv) in the annual mean and 200 $\mu g/m^3$ (≈ 97.4 ppbv) in the hourly mean values to be set for protection of human health. Recordings in publications and reports described in the following sections show that the critical values from the guideline have been exceeded widely all over the world and many times over many years.

1.2.2.1 Previous NO$_2$ measurements in Europe and Munich
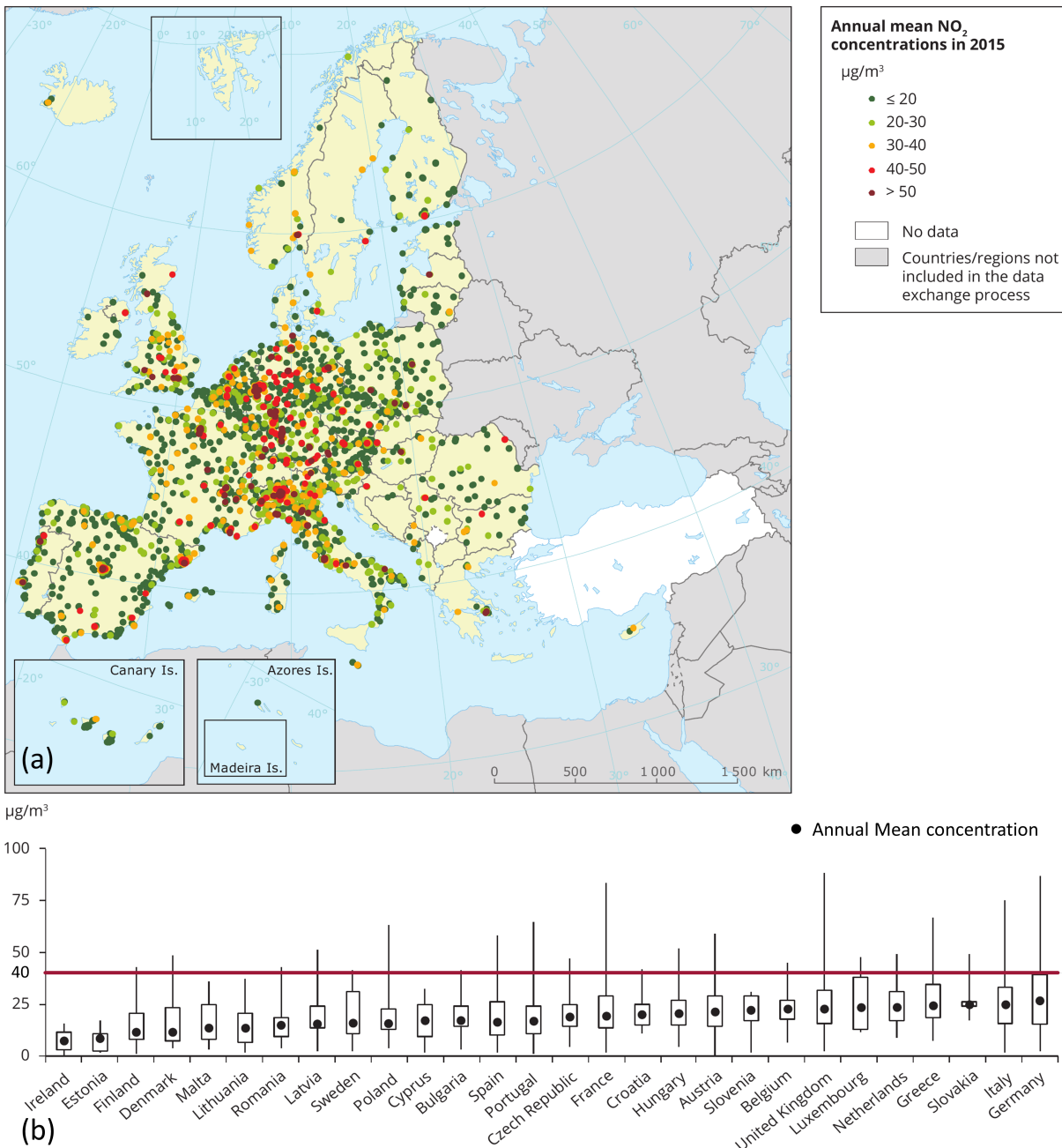
Figure 1.1: NO$_2$ concentrations of Europe, 2015 (EEA, 2017). (a) Red and dark red dots correspond to values above the EU annual limit value and the WHO AQG (40 μg/m^3). (b) The rectangles mark represent 25 % to 75 % of the stations, NO$_2$ levels are within coinciding range.

According to the European Environment Agency report 2017 (Figure 1.1(a)), NO$_2$ data in 2015 measured by 2680 stations located in all EU-28 Member States and nine
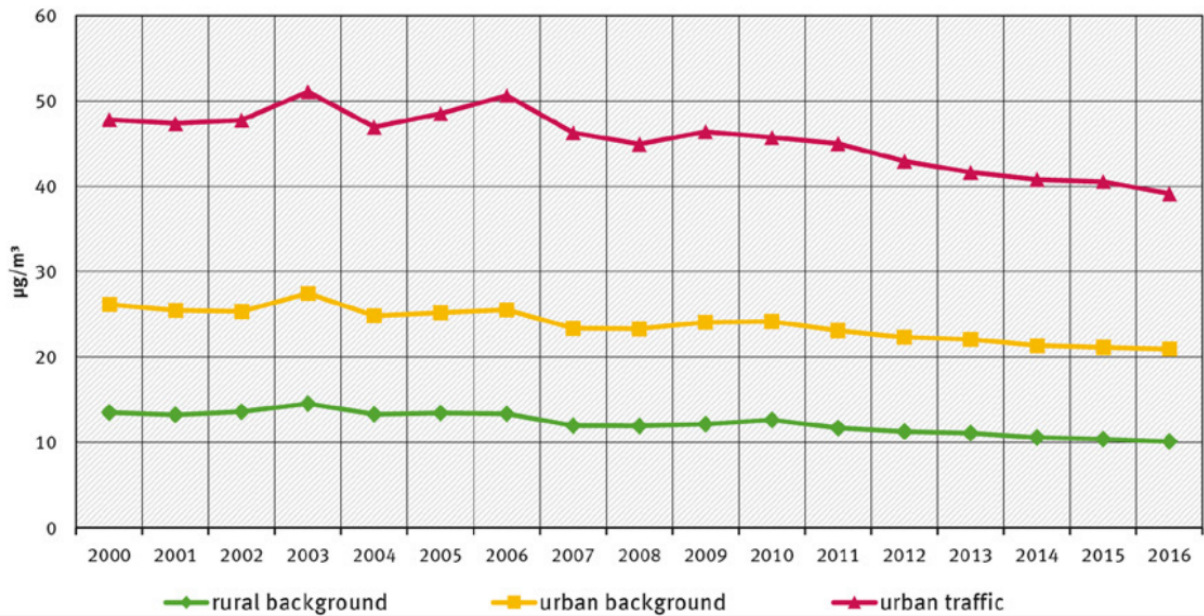
Figure 1.2: The trend of annual averaged NO_2 concentration from 2000 to 2016 in Germany. The air monitoring stations selected were those with continuous measuring (UBA, 2017).

other reporting countries had a minimum 75 % coverage of valid data. Twenty-two of the EU-28 (see Figure 1.1(b)) recorded NO_2 concentrations above the annual limit value. It indicated that the stations with high NO_2 concentrations above the annual limit value were widely distributed across Europe. Especially, Germany had a relatively higher NO_2 pollution in 2015 comparing to most European countries. Furthermore, all exceeded NO_2 concentrations were not observed at rural background stations, instead they were mainly observed in urban or suburban stations. More specifically, 89 % exceeded values were observed at traffic stations. Meanwhile, the air quality report 2016 of German environment agency (Umwelt Bundesamt) also pointed out that the air pollution in urban conurbations were primarily determined by the traffic and episodes of high NO2 levels were frequently recorded at the urban traffic stations (shown in Figure 1.2).

The conclusion that traffic is a major source of NO_2 is based upon the reaction between NO emission and O_3 in the air for forming NO_2, which has been confirmed by the Bavarian Environment Agency (LfU). The trend of the NO_2 annual mean concentration from 2000 to 2014 at monitoring stations located in busy streets of Bavarian cities and locations with values higher than the annual mean are shown in Figure 1.3. It indicated that the on-road NO_2 concentration limits were exceeded in most Bavarian cities for the entire period, in particular for the annual NO_2 level of Munich (Landshuter Allee) which was more than twice as much as the annual limit NO_2 value of WHO AQG.
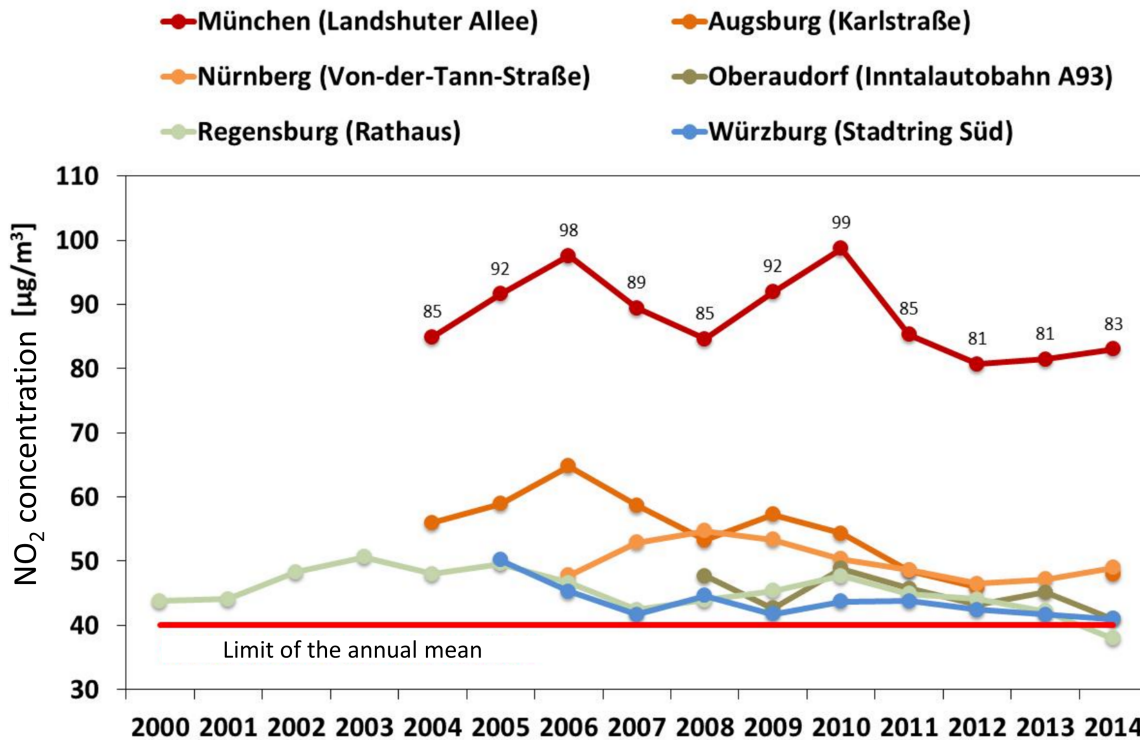
Figure 1.3: NO_2 concentrations of air monitoring stations with heavy traffic in Bavaria, Germany from 2010 to 2014 (LfU, 2015).

1.2.2.2 Previous NO_2 measurements in Asia and Hong Kong

Due to extremely rapid economic growth, air pollution in Asia has become a serious problem in recent decades. According to World Energy Outlook Special Report 2016, the number of premature deaths attributed to outdoor air pollution continued to grow, especially in developing countries in Asia which accounted for almost 90 % of the rise. Cofala et al. (2012) reported that East Asia (including China, Japan, South Korea, North Korea, and Mongolia) contributed about 29 % to the global NO_x emissions, much more than those of the United States and Europe. Anthropogenic emission of NO_x has levelled up across East Asia since 2000 (Zhang et al., 2009b) and it will continue to increase by 2030 (Cofala et al., 2007; Wang et al., 2014).

In addition, NO_x emissions in China have dominated the changes within East Asia in recent years. Zhang et al. (2009b) showed that the NO_x emissions in China accounted for about 81.7 % of the total emissions in East Asia till 2006. Duan et al. (2016) also indicated NO_x emitted by China was 12 times of NO_x emission in Japan in 2008. From 2005 to 2010, the emissions of NO_x increased by 25 % in China while the ones in East Asia other than China even decreased by 13 % - 17 % (Wang et al., 2014). Plenty of evidence has been provided by many observations that the air pollutant emitted by China not only affecting domestic air composition, but also being transported to neighboring and downwind regions (Russo et al., 2003; Jacob et al., 2003; Kang et al., 2010).

Hong Kong is a harbor city on the eastern side of the Pearl River estuary in East Asia and south of the mainland China. In Hong Kong, vehicle emissions are the main source of NO$_x$. According to the Hong Kong Emission Inventory Report 2015, road transport has been one of the top three sources of total NO$_x$ emission in Hong Kong since 1997. Similar to many other metropolitan cities, a decreasing trend of ambient and roadside NO$_x$ levels is recorded in Hong Kong (Carslaw, 2005; Keuken et al., 2009; Tian et al., 2011), which is contributed from the effective vehicular emission control measures in the past. However, the pollution levels measured at both ambient and roadside air quality monitoring stations are still occasionally exceeded the WHO guideline values of $40\,\mu$g/m^3 (annual) and $200\,\mu$g/m^3 (hourly) for NO$_2$, with more frequent exceedance of hourly NO$_2$ with high values observed at roadside stations. A rising trend of NO$_2$/NO$_x$ ratio with reduction of NO$_x$ is recorded at the roadside monitor stations in Hong Kong, which means the reduction rate of NO$_2$ is slower than NO in recent years (Tian et al., 2011). Such a trend can be particularly detrimental to Hong Kong because a large fraction of the population is exposed to the traffic-related primary pollutants in the street canyons. In other words, the release of excessive anthropogenic NO$_2$ has immediate or chronic direct or indirect influence on our living environment and physical health.

1.3 Motivation of the citywide NO$_2$ study

With the development of economic globalization and regional integration, dense urban areas represented by large and mega cities are forming. Anthropogenic air pollution accounts for a larger proportion of pollution than before. Urban circles have high population density and the episodes of high NO$_2$ levels were observed in the worldwide cities. High level NO$_2$ has the negative influence on human health. In addition, the dwell time, the diffusion and the depletion of pollutants depend not only on weather conditions (e.g. radiation transformation, wind, temperature and humidity), but also on urban structure (e.g. vegetation coverage, building height and density). In order to implement effective counter-measures, it is vital to understand the distribution of trace gases in both large and small scales to identify the pollution hotspots. Therefore, capturing the spatio-temporal distribution of trace gases and other pollutants could be an efficient method to be implemented in addition to continuous ground based point measurements.

Vehicular NO$_x$ emission is one of the main air pollution sources in most cities which is described in 1.2.2. Vehicular NO$_2$ is primarily emitted at the tail pipe and secondarily formed from oxidation of NO emission involving ozone and volatile organic compounds (VOCs) in the ambient (Muilwijk et al., 2016; Chang et al., 2016). The increase of NO$_2$/NO$_x$ ratio could be related either to the upgrades of vehicle engines and catalytic filters or to changes in the composition and ambient level of VOCs. However, NO$_2$ concentration changes rapidly with time and has a very strong spatio-temporal variability, which is often unknown in urban areas (Longley et al., 2015). Regular roadside air quality monitoring stations are not sufficient to capture these variations and could not provide an overview of the roadside pollution situation representative for Hong Kong or Munich. Therefore, it is necessary to perform on-road mobile measurements for better understand-

ing the pollutant distribution and spatial coverage of NO_2 for the entire city.

This thesis aims to assemble the spatio-temporal distributions of NO_2 concentrations using multiple Differential Optical Absorption Spectroscopy (DOAS) and Cavity attenuated phase shift spectroscopy (CAPS) instruments. Each of the three Long-Path DOAS (LP DOAS) instruments is equipped with a blue Light Emitting Diode (LED) as light source and a corresponding retro reflector arrays located from several hundred meters up to kilometers distance to the telescope of the instrument. A precise NO_2 roof-level concentration along the light path can be determined by recording the spectrum of the reflected light beam and continuously observing atmospheric NO_2. A Two Dimensional (2-D) scanning Multi-AXis DOAS (MAX DOAS) with a rotating prism scans the sky to capture the NO_2 profiles above roof-top level. A compact car-based MAX DOAS with a fixed viewing direction is used to capture the mobile slant column of NO_2, together with a CE DOAS and a CAPS measuring on-road NO_2 near the ground, in order to determine the NO_2 variability. The results are used for the validation of satellite data, and the intercomparison among different techniques. They are also useful for chemical transport model simulations and can be as input for parameter estimators to determine dynamical modes like transport and source terms inside the measurement volume.

Moreover, with the combination use of LP DOAS and CE DOAS, a representative high-resolution spatial distribution map of street level NO_2 that mainly focuses on traffic emission makes identifying city pollution hotspots possible. It could meanwhile provide valuable information for urban planning as well as benefit the development of pollution control measures. With regards to obtaining the pollutant information, on-road mobile CE DOAS measurements have been successfully deployed in Munich, Germany and Hong Kong, China. As common characteristics, traffic is one of most dominant emission sources for both cities, and these two cities are typical urban structures with relatively high buildings, dense population and city vegetation areas. Different locations of Munich and Hong Kong allowed us to investigate the difference of the local pollution transport properties between the inland city (Munich) and the harbor city (Hong Kong).

2 Observation techniques

There are plenty of experimental approaches for measuring and interpreting absorption spectra. This chapter will mainly explain the fundamental physical base of absorption spectroscopy and its applications, and also describe the technical solutions that realize this method. The absorption spectrum is the variation of the absorption intensity as a function of frequency or wavelength. Absorption spectroscopy, particularly in ultraviolet-visible and infrared wavelength range, is widely applied as a measurement technique in analytical chemistry. It measures the absorption of electromagnetic radiation due to its interaction with a sample, for determining the composition of the sample and quantifying the amount of one or several substances present. This technique is also employed in the field of molecular and atomic physics, astronomical spectroscopy and remote sensing. In addtion, some other observation methods used in this study will be also briefly introduced.

Table 2.1: Summary of the experimental methods used in this study.

Experimental Method	Measurement quantity	Measurement Technique
ChemiLuminescence (CL)	Concentration	In-situ
LP DOAS	Integrated concentration along the light path	Active remote sensing
CE DOAS	Concentration	Active in-situ
Multi-AXis DOAS (MAX DOAS)	Column density, Vertical profile	Passive remote sensing
Satellite DOAS	Column density	Passive remote sensing
CAPS	Concentration	Active in-situ
Dual-beam UV absorption	Concentration	Active in-situ

Table 2.1 lists the experimental methods for this study. According to the light sources, the experimental methods are distinguished into active and passive. Active methods use artificial light, while passive methods rely on natural light sources. Their measurement quantities are also listed. A more detailed overview of these methods are presented in following sections.
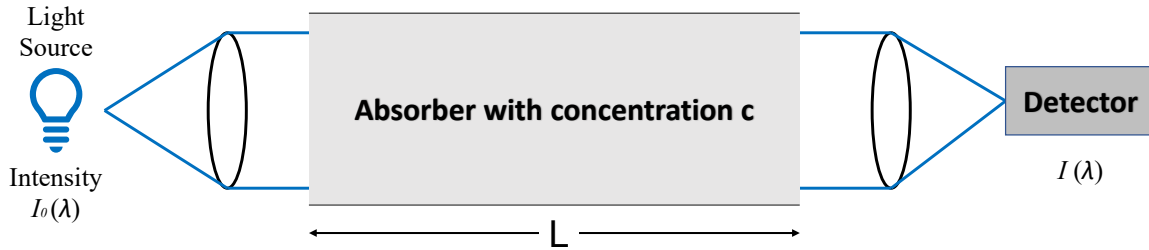
Figure 2.1: A light beam passes through a volume of length L having the absorber with concentration c. The intensity at the end is measured by a detector

2.1 Classic absorption spectroscopy

Absorption spectroscopy has the advantage of its specific and quantitative character. It is widely used in chemical analysis. The Beer–Lambert–Bouguer Law is the key to quantify the amount of substances based on an absorption spectrum. The law in different forms was successively introduced by Pierre Bouguer in 1729 (Bouguer, 1729), Johann Heinrich Lambert in 1760 (Lambert, 1760) and August Beer in 1852 (Beer, 1852). First, Lambert indicated the absorbance of a material sample is directly correlated to its thickness. Then, another attenuation relationship was discovered by August Beer between the absorbance and the concentration of the attenuating species in the material sample. Nowadays, the Beer–Lambert–Bouguer law merges the two attenuation relationships and is applied in many present quantitative trace gas analytical applications in the atmosphere. The basic principle of absorption spectroscopic trace gas detection is shown in Figure 2.1. It describes the absorption of electromagnetic radiation by matter. In order to analyze gaseous (or liquid) absorbers, a formulation of the Beer–Lambert–Bouguer law can be written as:

$$I(\lambda) = I_0(\lambda) \cdot \exp\left(-\sigma(\lambda) \cdot \int c(s)ds\right) = I_0(\lambda) \cdot \exp\left(-\sigma(\lambda) \cdot c \cdot L\right) \qquad (2.1)$$

where $I_0(\lambda)$ is the initial intensity of the incident radiation by a light source and $I(\lambda)$ denotes the intensity of the transmitted light with absorption cross section of $\sigma(\lambda)$, while the concentration of the absorbing gas $c(s)$ integrates along the light path L, or using c to represent an uniform concentration of the absorber. The absorption cross-section at wavelength $\lambda, \sigma(\lambda)$, is a nature of any absorbing species. The optical path length can be easily measured. So, the average trace gas concentration of the absorbing gas can be retrieved by measuring the ratio $\frac{I_0(\lambda)}{I(\lambda)}$. The deformation of equation 2.1 is:

$$c = \frac{ln\left(\frac{I_0(\lambda)}{I(\lambda)}\right)}{\sigma(\lambda) \cdot L} = \frac{D}{\sigma(\lambda) \cdot L} \qquad (2.2)$$

Here, D is defined as the natural logarithm of the ratio $\frac{I_0(\lambda)}{I(\lambda)}$ and called the optical density of the absorbing layer. Through measuring the intensities with $(I(\lambda))$ and without $(I_0(\lambda))$ the absorber in an artificial light source and combining the known quantities of

the absorption cross-section of the species and the absorbing light path, the species' concentration can be calculated. This equation is the foundation of most absorption spectroscopic applications.

2.2 Differential Optical Absorption Spectroscopy (DOAS)

For open atmosphere, the Beer–Lambert–Bouguer law can not directly be applied due to several difficulties. First, the initial intensity $I_0(\lambda)$ from a light beam is hard to be determined, as it has to overcome the difficulty of removing the absorbing gas from the atmosphere. Second, the absorbing species is not the only reason for light attenuation. Scattering on molecules and aerosols is another reason, which has to be corrected as a factor. Third, the total absorption contains the absorptions of several species, which makes it difficult to measure a desired species. The solution lies in measuring the so-called 'differential' absorption, which measures the difference between the absorptions at two or more wavelengths. More details will be introduced subsequently in this section.

The differential optical absorption spectroscopy (DOAS) technique can be described by the expanding deformation of the Beer–Lambert–Bouguer Law (equation 2.3). Note that, aerosol extinction processes including Rayleigh (ε_R) and Mie (ε_M) scattering, the effect of turbulence and additional signal attenuation of the light beam through the instrument's optics (b), show very broad spectral characteristics, which vary smoothly with the wavelength λ. On the contrary, certain trace gases exhibit narrowband absorption structures, which vary rapidly with the wavelength λ (Axelsson et al., 1990). So, one absorption band can be separated into 2 parts: broadband and narrowband. Same goes for the absorption cross-section that $\sigma_i(\lambda) = \sigma_{ib}(\lambda) + \sigma_i'(\lambda)$. The threshold between broadband and narrowband cross-sections depends on the observed wavelength interval and the width of the absorption bands to be detected. Generally, the broadband structures of the spectrum are filtered by dividing through a fitted polynomial or a smoothed spectrum. As shows in equation 2.5, all broadband effects are fitted into a polynomial $A(\lambda)$ with a specified degree by means of a non–linear least squares fitting algorithm (Stutz and Platt, 1996). Commonly $\sigma_i'(\lambda)$ is called differential absorption cross-section. The slant column density (SCD) is used to represent the concentration of the absorbing species integrated along the whole volume in equation 2.6. A quantity $I_0'(\lambda)$ is defined as the intensity without the differential absorption component shown in equation 2.7. Likewise, the differential optical density D' can be defined as the logarithm of the ratio $\frac{I_0'(\lambda)}{I(\lambda)}$ (shown in equation 2.8). Then the Beer–Lambert–Bouguer law can again be applied to the narrowband trace gas absorptions.

$$I(\lambda) = I_0(\lambda) \cdot \exp\left(-L\sum \sigma_i(\lambda) \cdot c_i + \varepsilon_M(\lambda) + \varepsilon_R(\lambda) + b(\lambda)\right) \tag{2.3}$$

$$= I_0(\lambda) \cdot \exp\left(-L\sum \sigma_i'(\lambda) \cdot c_i + \sigma_{ib}(\lambda) \cdot c_i + \varepsilon_M(\lambda) + \varepsilon_R(\lambda) + b(\lambda)\right) \tag{2.4}$$

$$= I_0(\lambda) \cdot \exp\left(-\sum \sigma_i'(\lambda) \cdot c_i \cdot L\right) \cdot A(\lambda) \tag{2.5}$$

$$= I_0(\lambda) \cdot \exp\left(-\sum \sigma_i'(\lambda) \cdot SCD_i\right) \cdot A(\lambda) \tag{2.6}$$

$$= I_0'(\lambda) \cdot \exp\left(-\sum \sigma_i'(\lambda) \cdot SCD_i\right) \tag{2.7}$$

Since the absorption structure of each trace gas is unique and determined in the laboratory, it is possible to discriminate the different absorptions of several trace gases in the sum of equation 2.8 by measuring the radiation intensity at multiple wavelengths. DOAS instruments normally measure the intensity from $500\,\mathrm{nm}$ to $2000\,\mathrm{nm}$ individual wavelengths in order to retrieve the concentrations of various absorbing trace gases in the atmosphere. Another advantage of measuring the absorbing intensity over broad wavelength band is the enhancement of the detection limit about trace gases with low concentrations or absorptions.

$$D'(\lambda) = ln\left(\frac{I_0'(\lambda)}{I(\lambda)}\right) = L \cdot \sum \sigma_i'(\lambda) \cdot c_i \tag{2.8}$$

The absorption cross-sections of following atmospheric trace gases are frequently measured by DOAS technique: O_2, O_3, O_4, NO_2, NO_3, SO_2, HONO, HCHO, CHOCHO, BrO, OBrO, ClO, OClO, IO, OIO and so on (Pfeilsticker and Platt, 1994; Hönninger et al., 2004; Lee et al., 2005; Sinreich et al., 2007; Huang et al., 2010a; Irie et al., 2011; Li et al., 2013). Most trace gases are only absorbed in a certain wavelength range. The same wavelength range, however, sometimes has numerous of simultaneous absorbers such as O_3, SO_2, NO_2, HONO, HCHO, and BrO, which all show absorption features at wavelengths from $300\,\mathrm{nm}$ to $400\,\mathrm{nm}$. As explained in equation 2.8, the separation and selective detection becomes possible in the real atmospheric measurement since the absorption cross-section of each trace gas is unique.

The DOAS method can be utilized in a variety of different setups. Depending on the DOAS applications' light sources, they are divided into active and passive DOAS. An active DOAS relies on artificial light coupled to an optical system that sends and receives light, such as LP DOAS and Cavity-Enhanced DOAS (CE DOAS) that has a more compact setup. Typical applications of passive DOAS are multi-axis DOAS (MAX DOAS), satellite borne DOAS, imaging DOAS, direct sunlight DOAS and so on. They all utilize natural light sources, e.g. the sun or the moon, which has been scattered and partly absorbed in the atmosphere to derive profile information of gases and aerosols. In addition, passive DOAS consists of direct light DOAS and scatter light DOAS.

The advantages of active DOAS and direct light passive DOAS are their high accuracy (because they are only based on the absorption cross-section) and great sensitivity (because of a long enough light path which contributes little to the error). In contrast, the

accuracy of scatter light passive DOAS can be influenced by more uncertainties. First, the determination of the absorption path length is a major challenge. Second, the temperature dependence of the various absorption cross-sections has to be taken into account. Besides, the Fraunhofer bands which mostly have much larger optical densities than those of the trace gas absorptions, is another error in passive DOAS and need to be accurately removed. In addition, the artificial light used by active DOAS is always available, while the natural light (as the light source for passive DOAS) has its limitation of being detected and usually restricts operations to daylight hours only. However, the convenience of passive DOAS is its relatively much simpler experimental setup (no light source, smaller telescope, etc.).

Some of the DOAS applications mentioned above are detailed described in following subsections. In addition, the DOAS system in our study areas is also introduced. The Munich spatio-temporal DOAS measuring system combines three different types of DOAS instruments (CE DOAS, LP DOAS and MAX DOAS). The measurement system is installed on the roof of the building of the Meteorological Institute Munich (MIM) at Ludwig Maximilian University (LMU) at the center of Munich (Figure 2.2).
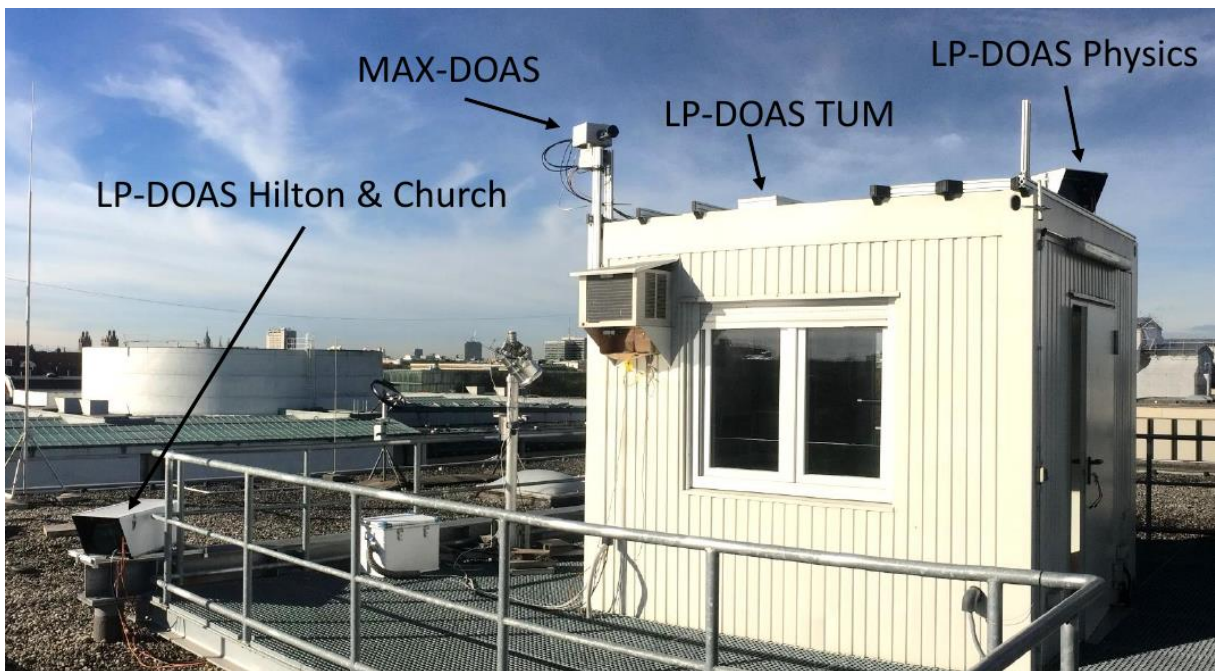
Figure 2.2: Photo of the actual experimental setup of the DOAS instruments on the roof of LMU, Munich.

Three LP DOAS instruments scans retro reflector arrays in different directions and distances capturing the horizontal variations at roof-top level. A 2-D scanning MAX DOAS scans the sky to capture the volume above roof-top level. This instrument is equipped with a diffuser allowing direct sun DOAS measurements as well. A CE DOAS is used to determine the NO_2 variability on the ground. The LP DOAS and MAX DOAS runs continuously, whereas the CE DOAS is used at different times of the year/week/day

under varying meteorological conditions to determine typical NO_2 distributions. The aim of this system is to assemble spatio-temporal distributions of NO_2 concentrations and this chapter will describe the general setup for each type of DOAS instruments.

2.2.1 Long Path DOAS (LP DOAS)

Long Path Differential Optical Absorption Spectroscopy (LP DOAS) is the classical active DOAS system. The instrument measures the average absorptions of trace gases along an extended volume air, from few hundreds meters up to several kilometers in the open atmosphere. Measured absorption spectra are converted to SCDs and divided by the defined measurement path length and the air density in order to quantify the trace gas concentration. Its original design consists of an emitting unit (including an artificial light source and a telescope) and a receiving unit (including a spectrometer and a telescope). Many investigations about atmospheric trace gases e.g. NO_2, O_3, CH_2O, have used this kind of setup since the 1980s (Perner and Platt, 1980; Platt et al., 1981; Harris et al., 1982). However, it requires both sides of optical elements to be aligned and power supply at both locations which is normally complicated for field measurement campaigns.

Modern designs of LP DOAS, introduced by Axelson et al. (1990), use the same main mirror to merge the transmitting and receiving telescope into one device in order to simplify the setup. The sketch of a coaxial LP DOAS setup is shown in Figure 2.3(a). The most important step in operating such a coaxial setup is the accurate alignment of the optical elements including the light source A, plane mirrors B and E, the main mirror C and the receiving fiber F. These parts have to be precisely fixed at certain relative positions and orientations. Light is emitted from the artificial light source (e.g. a xenon arc lamp or a high power LED) via plane mirror (B in Figure 2.3(a)) towards the main mirror (C in Figure 2.3(a)). The nearly parallel light beam then is directed to a retro reflector array (D in Figure 2.3(a)) and reflected back to the telescope. The reflected light via plane mirror E is focused onto the receiving fiber and then transmitted to the spectrograph. This setup, on the one hand, doubles the light path and thus lowers the detection of optical density of trace gas. On the other hand, it reduces to one power supply and simplifies the alignment between telescope and retro reflector array. In addition, a single telescope makes LP DOAS multiply dimensions (horizontal and vertical) measurement possible as it can be easily pointed at different retro reflector arrays.

However, this setup still has several disadvantages. Firstly, there is plenty of light throughput loss because of the displacement of the light source by mechanical instability. Secondly, only half of the area of the main mirror is used for either transmitting or receiving light. Thirdly, complex alignment of all optical elements is always a challenge and has to be repeatedly as the high susceptibility of alignment to wind or temperature change and other mechanical disturbances (Merten et al., 2011). The latest modified setup, shown in Figure 2.3(b), uses a single Y-fiber bundle to combine transmitting and receiving fibers in the focal plane of the main mirror, which avoids the described disadvantages of the former coaxial setup. It uses the full main mirror for emitting and receiving light and provides an up to an order of magnitude higher performance in light throughput. Besides, the optical alignment becomes more simple, benefiting from the combined fiber bundle.
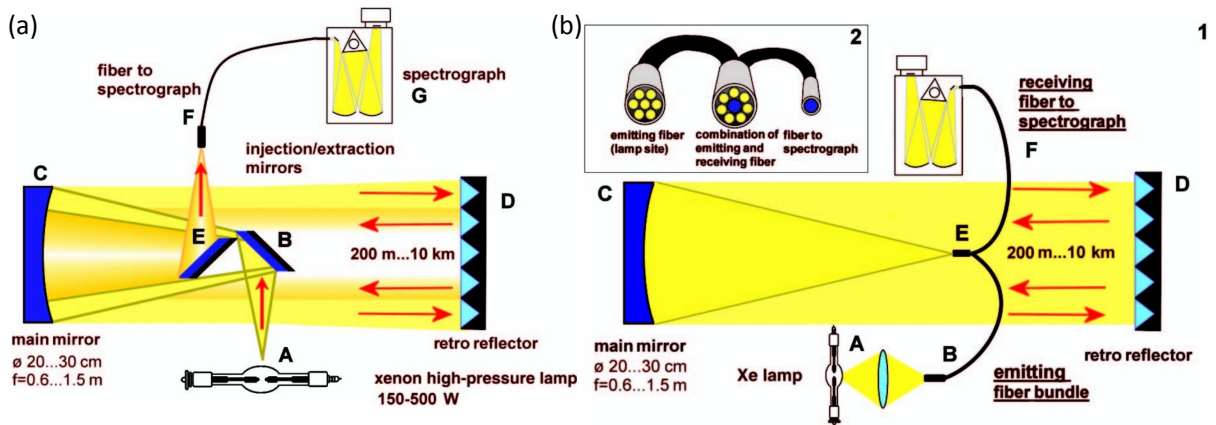
Figure 2.3: Sketch of (a) a coaxial LP DOAS setup introduced by Axelson et al. (1990). (b) a modified coaxial LP DOAS setup introduced by Merten et al. (2011), (1) with emitting and receiving fibers combined into a single bundle. The inset (2) shows the ends (left to right, B, E, F) of the fiber bundle.

In active LP DOAS systems, the telescope has to be precisely pointed at the light source or retro-reflector array. Because the light path will 'bend' due to changing thermal gradients in the atmosphere, this can usually only be accomplished by actively controlling the telescope. Even though, it may still lose the light from the retro-reflector time to time, therefore more frequently optimization of light path is necessary.

The LP DOAS technique has been widely used in different measurement settings, for example, vertical profiling LP DOAS and LP DOAS tomography etc. Vertical profiling LP DOAS extends the LP DOAS technique for trace gases vertical distribution measurements by scanning through several retro reflectors set up at the same location at different heights (Veitel et al., 2002; Stutz et al., 2004). LP DOAS tomography is another type of extending application of DOAS. It uses the measurement of column densities over different optical light paths to reconstruct the trace gases' spatial distribution. The accuracy of the reconstructed trace gases' spatial distribution is depending on the amount of viewing directions. Limited number of retro reflectors also affects the reconstruction resolution of the trace gases distribution. The geometric setting is another tough task and influences the reconstruction quality. Some measurements using LP DOAS tomography have been published and detailed information were provided (Laepple et al., 2004; Hartl et al., 2006; Stutz et al., 2016; Olaguer et al., 2017).

2.2.1.1 Experimental setup in Munich

A sketch of the LP DOAS instrument setup in Munich is shown in Figure 2.4. It has standard components as described above. The system consists of two parts: an indoor module with LED light source, temperature stabilized spectrometer(s) and electronics; an outdoor telescope system for light transmitting and receiving. Several or at least one array of retro reflectors for light reflection are required, consisting of 9×25 mm diameter quartz glass prisms in a sealed housing at the other end of the absorption path. Small single
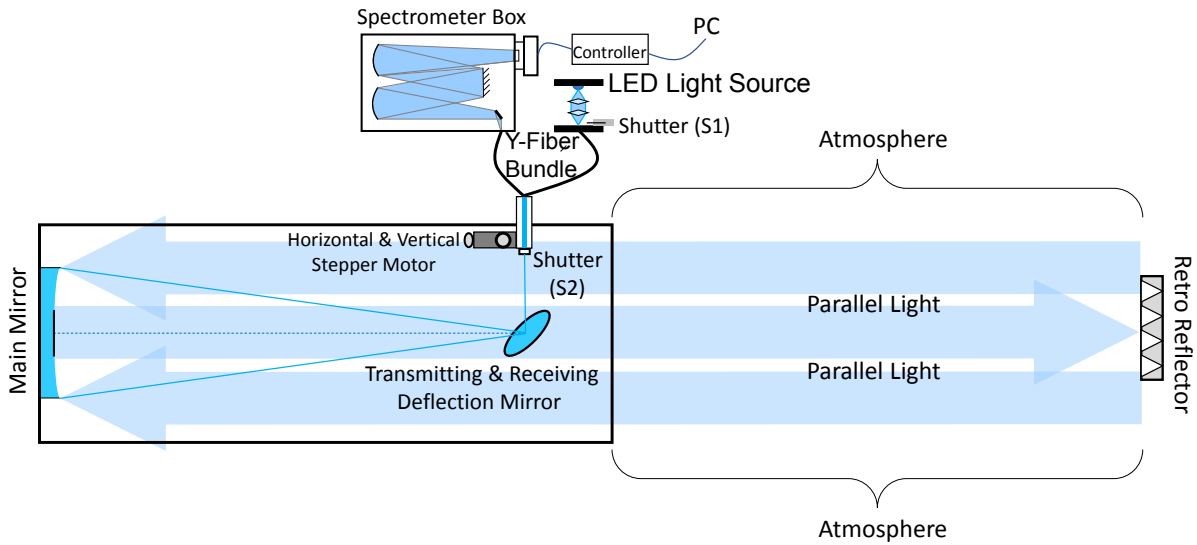
Figure 2.4: Schematic setup of the LP DOAS system on the building of MIM, at LMU using a coaxial arrangement of transmitting and receiving telescope in conjunction with a retro-reflector array built by EnviMeS Inc.

retro reflectors are used to achieve a better homogeneous reflection than large reflectors. The optical fibers (typical 5 m length) are used as a transmitter for the light from the fiber bundle to a parallel light beam pointing to the retro reflector array and the reflected light collected back to the spectrograph. The fibers are connected in a Y-bundle with six sending fibers connecting to the LED light surrounded by one receiving fiber connecting to the spectrometer, with a diameter of 200 μm. The blue LED light source (Cree royal blue, $\sim$450 nm full width half maximum (FWHM)) is integrated in the spectrometer housing. The optics are additionally equipped with a mechanical shutter to block the light in order to record background spectra. The light source is never turned off during a measurement period to avoid any spectral instabilities. A deflection mirror is placed at the focal point of the telescope's main mirror of 20 cm diameter and 80 cm focal length, producing an almost parallel light beam. The combined Y-fiber end is then placed close to the deflection mirror. Another mechanical shutter is placed right in front the end of the fiber to record the lamp spectrum. Two stepper motors allow precise adjustment of the telescope to the retro reflector array. The reflected light is collected by the receiving fiber and redirected to a high grade Avantes spectrometer (Avantes AvaBench-75, 1800 l/mm grating, wavelength range from 305 to 460 nm). The detector is a back-thinned Hamamatsu detector that has 2048 pixel (14 μ) and 895 μ sensor height and has high Ultra-violet (UV) sensitivity with quantum efficiency of $\sim$60 %. In combination with a 200 μm fiber, leading to a spectral resolution of 0.8 nm (FWHM) or better. The telescope has a stainless steel enclosure and is sealed at the front with a quartz glass window which is suitable for UV and visible application. Thus it is weather resistant and can be placed outside.

2.2.1.2 Evaluation procedure

The emission lines of a Mercury lamp and a Xenon glow lamp are used for the spectrograph calibration. The Mercury emission line at 435.84 nm is used to convolve the literature reference spectra to the instrument resolution. The software DOASIS (Kraus, 2005) (doasis.iup.uniheidelberg.de) is used for the LP DOAS measurement and data evaluation. Offset, dark current and background are corrected from all spectra before the DOAS fit. Then, taking the logarithm of the ratio between the measurement spectrum and the corresponding LED reference spectrum. In addition, a high pass filter (a binomial filter of the order of 1000) is applied in order to remove the broadband structures from the spectrum. The residual broadband structures are removed by fitting and subtracting a second order polynomial during the DOAS fit.

One set of shift and squeeze parameters are implemented for all references spectra in order to correct for small uncertainties in the wavelength mapping. The latter of NO_2 (Vandaele et al., 2002), Glyoxal (CHOCHO) (Volkamer et al., 2005), O_4 (Hermans et al., 1999) and H_2O (Rothman et al., 2003) are taken. For the non-linear optimization, DOASIS uses a Levenberg-Marquard fit and b-splines for the interpolation. The same high pass filter that applied for measurement spectra is also applied for the reference spectra. The spectral fit is performed in the wavelengths (from 432.0 nm to 457.6 nm) that includes several strong NO_2 absorption lines. The measured slant columns are converted to mixing ratios in part-per-billion by volume (ppbv) by dividing the slant columns (the product of the total absorption length and the air density). Simultaneous pressure and temperature information are used for the air density calculation.

2.2.2 Cavity Enhanced DOAS (CE DOAS)

Cavity Enhanced DOAS (CE DOAS) technique is an expansion of LP DOAS and a relatively new spectroscopic measurement technique which provides an alternative option for small scale measurements. CE DOAS uses an optical resonator consisting of two highly reflective mirrors to turn a short geometrical light path into a long effective light path, in order to enhance the absorption signal within a limited space. A great advantage of CE DOAS for in-situ measurements is that its setup contains a closed measurement cell isolated from the environment, which allows to sample the air at a well defined location. The light signal is bounced back and forth within this isolated chamber to measure trace gas absorption within a small volume. In addition, it protects the sensitive optical elements from the environment contamination. The principle of the CE DOAS (Platt et al., 2009) is similar to that of the cavity enhanced absorption spectroscopy (CEAS) (Fiedler et al., 2003). The measured absorption spectrum of an incoherent broadband light source (e.g. LED) is used to determine the concentration of trace gases. The combination of the optical cavity enhanced technique with incoherent broadband lights sources allows the application of the DOAS technique for the detection of multiple trace gases by a single instrument.

Sensitive measurements of trace gas and aerosol extinction have already been demonstrated by Langridge et al. (2006); Venables et al. (2006); Washenfelder et al. (2008);

Thalman and Volkamer (2010); Min et al. (2016); Chan et al. (2017). Compared to other in-situ NO_2 monitoring techniques, CE DOAS is insensitive to other reactive nitrogen (NO_y) in the atmosphere, making it a better option for small spatial scale measurements and detection of spatial variation of trace gases. Its high accuracy provides us with improved measurements in comparison to previous measurements with less sensitive sensors. The latter ones do not achieve such a information content due to their large measurement error.

2.2.2.1 Experimental setup in Munich
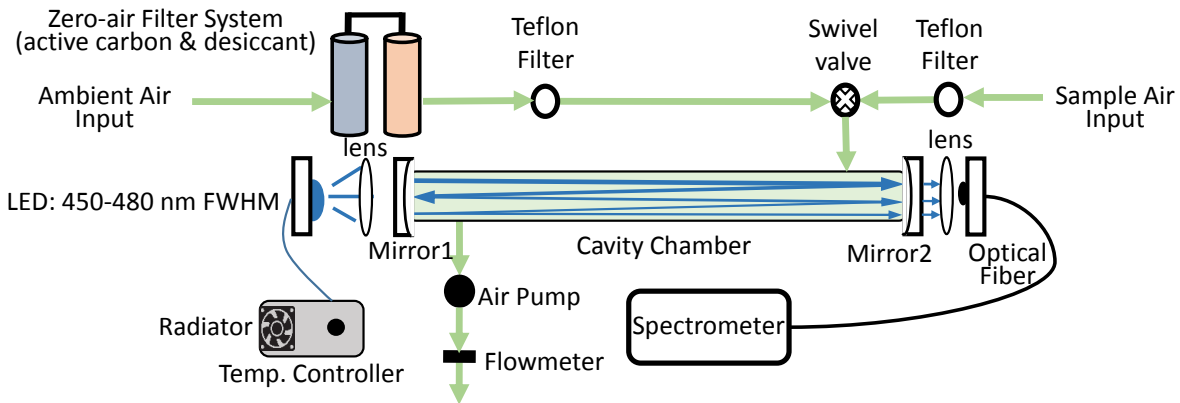
Figure 2.5: Schematic diagram of the experimental setup of the CE DOAS built by EnviMeS Inc.

A sketch of the CE DOAS instrument is shown in Figure 2.5. The CE DOAS consists of a blue LED light source, an optical resonator with two high reflective mirrors, a spectrometer and an air sampling system. Dielectric coated high reflective mirrors (Layertec GmbH, reflectivity $> 99.98\%$ at 440 nm) are placed at both ends of the sampling cell to form an optical resonator. Light from the high power blue LED (CREE XR-E royal blue, 440 nm - 455 nm FWHM) is coupled into the optical resonator by a convex lens with a focal length of 25 mm. Light escaped from the other side of the optical resonator is coupled to an optical fiber with a numerical aperture (NA) of 0.22 by a convex lens with a focal length of 50 mm and an aluminum mirror. The transmitted light is redirected to the spectrometer for spectral analysis through the optical fiber. Spectra are recorded by an Avantes spectrometer (AvaSpec-ULSi2048L-USB2) with a Sony ILX511 Charge Coupled Device (CCD) detector. The spectral range of the spectrometer is adjusted to 395 nm - 492 nm with a spectral resolution of 0.47 nm (FWHM). The sampling cell is made by a Teflon pipe with length of 50 cm and a sampling volume of 286.3 cm^3. The sample flow of the system is achieved by a Direct Current (DC) vacuum pump located at the outlet side of the sampling chamber. A Teflon filter is placed in front of the inlet of the sampling cavity to avoid aerosols entering the sampling cavity and affecting the optical path by scattering and contamination of the high reflective mirrors. The time resolution of the CE DOAS is adjusted to 4 seconds during the mobile measurement. Detailed description of the CE DOAS instrument can be found in Platt et al. (2009); Chan et al. (2017).

The software DOASIS (Kraus, 2005) is used for the CE DOAS spectral evaluation. The CE DOAS spectral fit is performed in the wavelengths from 435.6 nm to 455.1 nm, which includes several strong NO_2 and water vapor absorption bands. Reference absorption cross sections of NO_2 (Vandaele et al., 2002), H_2O (Rothman et al., 2003), Glyoxal (CHOCHO) (Volkamer et al., 2005) and O_4 (Hermans et al., 1999) are included in the DOAS fitting.

2.2.2.2 Data evaluation procedure

The CE DOAS evaluation procedure is similar to the LP DOAS. First, the offset and dark current spectrum is taken by switching off the LED light source. Then, the lamp spectrum I_0 is measured by flushing the cavity chamber with NO_2 free zero air using zero-air filter system. Different from LP DOAS, the length of the effective light path ($L_{eff}(\lambda)$) of CE DOAS needs to be calculated for each measurement. According to equation 2.8, $L_{eff}(\lambda)$ is related to the measured optical density (D) which is a priori unknown. However, the broadband Rayleigh scattering extinction can be calculated with an iterative approach. The light path in the first iteration step is the calibrated light path ($L_0(\lambda)$) assuming no trace gases absorption. The relationship between $L_{eff}(\lambda)$ and $L_0(\lambda)$ is defined in equation 2.9. The first approximate trace gas concentration is retrieved by applying the DOAS fit and is then used for the calculation of the second D as shown in equation 2.10.

$$L_{eff}(\lambda) = L_0(\lambda) \cdot \frac{D(\lambda)}{\exp{(D(\lambda))} - 1} \tag{2.9}$$

$$D_{n+1}(\lambda) = L_{eff}(D_n, \lambda) \cdot \left(\sum \sigma_i(\lambda) \cdot c_i + \varepsilon_R(\lambda) \right) \tag{2.10}$$

Then the resulting fit is used to modify the D for the fit in the next iteration. This iteration process is repeated untill a certain measurement accuracy is achieved or the number of iterations reached the maximum allowed (Frankenberg et al., 2005). The simultaneous pressure and temperature are recorded to calculate the air density and to convert the column density into mixing ratio units.

$$D_x(\lambda) = \frac{I_0(\lambda)}{I_{He}(\lambda)} - 1 = L_0(\lambda) \cdot \epsilon_\Delta(\lambda) \tag{2.11}$$

$$L_0(\lambda, T_0, P_0) = \frac{\frac{I_0(\lambda)}{I_{He}(\lambda)} - 1}{\epsilon_{He}(\lambda, T_{He}, P_{He}) - \epsilon_0 Air(\lambda, T_0, P_0)} \tag{2.12}$$

As we describe above, CE DOAS is realized using two highly reflective mirrors to extend the effective light path up to several kilometers within a short isolated measurement chamber. Only the known path length L_{eff} makes the evaluation of the concentration in the quarz cell possible. So, it is sufficient to know the path length L_0 of a zero air cavity used for trace gas extinction correction. In addition, the effective path length strongly depends on the cleanliness of the mirrors and the alignment of the resonator, the LED and the optical fiber. The path length calibration is the main source of the total measurement error. Therefore the path length has to be calibrated from time to time in case that these parameters change. During the practical calibration for L_0, the light transmitted by a

cavity filled with zero air (I_0) and helium air (I) which has a very week Rayleigh extinction are measured subsequently. Therefore, the tendency of measured intensities of zero air and Helium shows a relatively strong change. In equation 2.11 and 2.12, the extinction $\epsilon_\Delta(\lambda) = \sigma_x(\lambda) \cdot c_x$ only contains contributions from the trace gas absorption, the $\sigma_x(\lambda)$ and c_x are the absorption cross section and the absorber concentration respectively. The extinction coefficient of helium only contains Rayleigh scattering, whereas the extinction coefficient of air contains a contribution from the O_2 dimer O_4 at absorption bands 446 nm and 477 nm. The O_4 absorption coefficient can be known from Hermans et al. (1999). The number densities of helium and air are calculated using the ideal gas law. Afterwards, the L_0 can be derived. More detail about this method have been introduced by Washenfelder et al. (2008).

2.2.3 Multi-AXis DOAS (MAX DOAS)

The molecular absorption in the ultraviolet and visible spectral bands obtains the information of tropospheric aerosols and traces gases. The MAX DOAS is a variant of the passive Zenith Scattered Light DOAS (ZSL DOAS) technique that takes a series of off-axis observations of scattered sun light in several viewing directions and at different elevation angles, in order to gain these information. The growth of the observed trace gas slant column as a function of increasing scanning angles gives information about the vertical distribution of the trace gas. In addition, it is especially sensitive to aerosols and trace gases in the lower troposphere.

The MAX DOAS has a relatively simple setup, requiring only one or two spectrometers (depending on the required wavelength range, could be either visible or UV range, or both) and a unit of spectrometer-telescope assembly to look into different directions. A complete measurement cycle encircling a series of observation directions may take up to several minutes (e.g. Hönninger and Platt (2002)). If the measurements are not taken simultaneously, it could be a problem for the data retrieval process when the radiation transport conditions (e.g. cloud cover, aerosol load, or during sunrise/sunset) of the measurement periods are rapidly changing in the atmosphere. In the recent development of a two-dimensional MAX DOAS, a single spectrometer is equipped with a two-dimensional CCD detector, one for dispersion and the other one simultaneously observes at different elevation angles to capture the spatial resolution. However, this setup also increase the instrumental requirement and the maintenance of moving mechanical parts. Therefore, MAX DOAS can be inconvenient for long-term observations on remote sites. To be noticed, in order to phase out the solar Fraunhofer structure, the different MAX DOAS instruments have to be compared with each other. Still, the simplicity and inexpensiveness of the MAX DOAS setup make it an easy solution for atmospheric measurement. It has been widely used for providing indispensable observations of the vertical distribution of atmospheric aerosols and trace gases in the past decade (Hönninger and Platt, 2002; Bobrowski and Platt, 2007; Wagner et al., 2007, 2010; Lee et al., 2011b,a; Frins et al., 2014; Chan et al., 2015; Gratsea et al., 2016; Jin et al., 2016; Wang et al., 2017).

2.2.3.1 Experimental setup in Munich

The 2-D MAX DOAS instrument is set up on the roof of Meteorological Institute at the Ludwig-Maximilian-University of Munich about 20 m above ground level, located in the center of Munich. Figure 2.6 shows a photo of the actual experimental setup of the MAX DOAS instrument on the institute's roof. It measures scattered sun-light and consists of a scanning telescope with a prism reflector and a quartz-glass tube to protect the rotating prism, a stepping motor controller and a spectrometer covering the visible wavelength from 430 nm to 565 nm and UV wavelength from 295 nm to 450 nm. It is also equipped with a diffuser element in order to allow for direct sun-light measurements and can contain a mercury lamp. A tube filled with humidity absorbing silica gel connects the outside and inside air to compensate for changes in ambient pressure and humidity, in order to protect the highly sensitive spectrometers.

Figure 2.6: Photo of the actual experimental setup of the MAX DOAS on the roof of LMU

Scattered sun-light, collected by the telescope, is redirected by the prism reflector and a quartz fiber to the spectrometer for the spectral analysis. The telescope's field of view of the instrument is less than 0.3° and the elevation angle accuracy is around 0.1°. Two ultra-low stray light 75 mm Avantes spectrometers are equipped with a Sony 2048 L detector used for visible range and a Hamamatsu back-thinned detector optimized for UV range. The spectral resolution is 0.6 nm (FWHM). The telescope scanner unit is sealed and weatherproof. It is heated to avoid ice-cover at low temperatures. During the experiment, the spectrometer box is kept indoor and thermostabilized at 15°C. A sketch of the MAX DOAS instrument setup is shown in Figure 2.7 and the MAX DOAS is controlled by a computer and operated automatically during measurement.

2.2.3.2 Spectral retrieval

The emission lines of a Mercury (Hg) lamp are used for the spectrometer calibration. The literature reference cross sections convolve with the measured Mercury emission line at 435.84 nm to the instrument resolution, then the result is used for the spectral retrieval at different wavelength. After correcting offset and dark current, all measured spectra of the
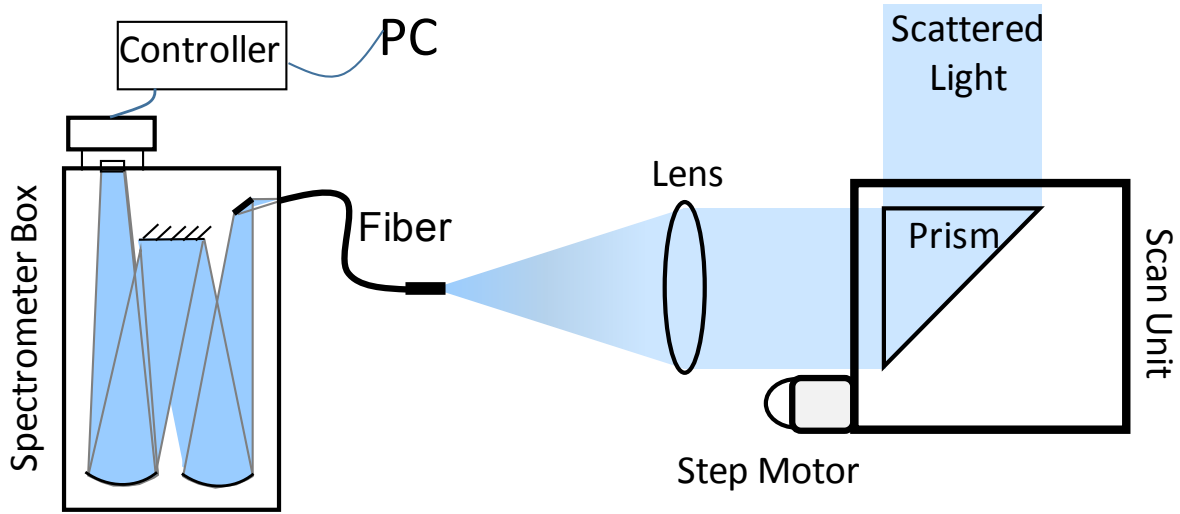
Figure 2.7: Schematic diagram of the experimental setup of the MAX DOAS built by EnviMeS Inc.

scattered sunlight at each elevation angle are divided by the corresponding zenith reference spectrum. By taking the logarithm it can be converted into optical density. Additionally, the Differential Slant Column Densities (DSCDs) of different trace gases, which defined as the difference between the SCD of the measured spectrum and the corresponding zenith reference spectrum, are retrieved by applying the DOAS method to the wavelength range from 425 nm to 490 nm of the spectrum. The broadband spectral structures are removed by including a 5_{th}. order polynomial in the DOAS fit. The absorption cross section of NO_2 (Vandaele et al., 1998), O_4 (Thalman and Volkamer, 2013), O_3 (Serdyuchenko et al., 2014), H_2O (Rothman et al., 2009) as well as the Ring spectrum are considered and fitted to measured optical densities. The software DOASIS (Kraus, 2005) is used for the spectral fitting analysis.

As there is a lack of cloud information in the radiative transfer calculations of the aerosol and trace gas retrievals, horizontally homogeneous layers are assumed. The retrieval might result in uncertainties if the radiation transport conditions are inhomogeneous or varying rapidly in the atmosphere. Therefore, the data are filtered to screen out these conditions before further processing for the aerosols and trace gases retrieval. The vertical profile of the oxygen collision complex O_4 is nearly constant, so the retrieved O_4 DSCDs are assumed to vary smoothly with time when the radiation transport condition is stable. Any lively variation of the O_4 intensities and DSCDs may denote that the radiative transport condition changes suddenly. Therefore, a locally weighted regression smoothing filter with a regression window of 3 h to the O_4 intensities and DSCDs time series at each elevation angle are applied as the filter for the data contaminated by inhomogeneous or rapid changes of radiation transport conditions. Data with fast varying O_4 intensities and DSCDs are filtered out and the data with slowly varying O_4 intensities and DSCDs are used in the aerosols and trace gases retrieval.

2.2.4 Satellite borne DOAS

Over the past two decades, the DOAS community has contributed much to the use of satellite borne DOAS instruments, that use sunlight scattered either by the atmosphere, the ground, or both. Three viewing geometries of these measurements are possible. The most common satellite viewing geometry is the nadir view. In the nadir geometry, the DOAS system looks down from space towards the nadir direction, receiving the sunlight reflected from the earth's surface. The Global Ozone Monitoring Experiment (GOME) (Burrows et al., 1999) was launched in 1995 use this geometry, to provide global concentration fields of trace gases, such as O_3, NO_2 , and HCHO. The ozone monitoring instrument (OMI) on the NASA Earth Observing System (EOS) Aura satellite measuring total column ozone is also a nadir geometry instrument and was launched in 2004 (Levelt et al., 2006b). In addition, some instruments like the SCanning Imaging Absorption spectroMeter for Atmospheric CHartographY (SCIAMACHY) (Bovensmann et al., 1999) determine vertical trace gas profiles with high resolution, employ measurements not only in single geometry, but also in several. They can be used both in nadir and limb geometries. There are several other currently operating DOAS based satellite instruments, in particular the Optical Spectrograph and InfraRed Imager System (OSIRIS) on Odin (Murtagh et al., 2002), the Improved Limb Atmospheric Spectrometer (ILAS) (Sasano et al., 1999).

2.2.4.1 OMI Satellite observations

The Ozone Monitoring Instrument (OMI) is a passive nadir-viewing satellite borne imaging spectrometer (Levelt et al., 2006a) on board the Earth Observing System's (EOS) Aura satellite. The instrument consists of two charge-coupled devices (CCDs) covering a wavelength range from 264 nm to 504 nm. A scan provides measurements at 60 positions across the orbital track covering a swath of approximately 2600 km. The spatial resolution of OMI varies from $\sim$320 km^2 (at nadir) to $\sim$6400 km^2 (at both edges of the swath). The instrument scans along 14.5 sun-synchronous polar orbits per day providing daily global coverage observations of NO_2, BrO, SO_2 and aerosols. It is able to detect cloud radiance fraction, cloud pressure and albedo as well.

In this study, NASA's OMI NO_2 standard product version 3 (SPv3) was used (Krotkov et al., 2017). The SCDs of NO_2 were derived from Earth's reflected spectra in the visible range (402‑465 nm) using an iterative sequential algorithm (Marchenko et al., 2015). Previous studies showed the updated SCDs were systematically lower by 10‑40 % than the previous estimates (Marchenko et al., 2015). The OMI NO_2 SCDs are converted to vertical column densities (VCDs) by using the concept of air mass factor (AMF) (Solomon et al., 1987). The AMFs were calculated based on the NO_2 and temperature profiles derived from the Global Modeling Initiative (GMI) chemistry transport model simulations with a horizontal resolution of 1° (latitude) $\times$ 1.25° (longitude) (Rotman et al., 2001). Separation of stratospheric and tropospheric columns was achieved by the local analysis of the stratospheric field over unpolluted areas (Bucsela et al., 2013).

2.3 Cavity Attenuated Phase shift Spectroscopy (CAPS)

Cavity Attenuated Phase shift Spectroscopy (CAPS) was invented by Herbelin and his colleagues for the characterization of mirror reflectivities (Herbelin et al., 1980) and applied into the detection of atmospheric measurement subsequently. CAPS is a technique closely related to Cavity Ring-Down Laser absorption Spectroscopy (CRDS) which determines the concentration of trace gases concentrations from the decay rate of the light source in the optical resonator (Engeln et al., 1996; Berden et al., 2000; Brown et al., 2002; Ball and Jones, 2003). CRDS is a laser-based system, while CAPS uses an incoherent light source (a blue LED) that is well-matched to the NO_2 absorption band. To be noted, the incoherent light source in CAPS eliminates many of the stability concerns associated with the practical application of laser-based CAPS and CRDS. In addition, it allows a compact, inexpensive sensor setup and provides relatively simple monitor design and no sensitivity loss during the operation.

The CAPS NO_2 system mainly consists of a blue LED, a measurement chamber with two highly reflective mirrors centered at 450 nm, and a vacuum photodiode detector. It determines the NO_2 concentration by directly measuring optical absorption of NO_2 at 450 nm wavelength of the electromagnetic spectrum. In brief, the light appears to be a distorted waveform after passing through two mirrors and the measurement cell, which is characterized by a phase shift that produced by demodulation techniques in comparison to the initial LED light modulation. The size of the phase shift is proportional to the absorbance of the light by the presence. By measuring the amount of the phase shift (θ), the concentration of NO_2 (χ) can be derived from the following formula:

$$\cot \theta = \cot \theta_0 + \frac{c}{2\pi f} \alpha_{NO_2} (T, P)_\chi \tag{2.13}$$

where c is the light speed, f is the modulation frequency of LED, the absorption coefficient of NO_2 (α_{NO_2}) is at the measured sample temperature (T) and pressure (P), and θ_0 is the detected phase angle of the sensor response of NO_2-free air.

The CAPS measures NO_2 with high accuracy (1 ppbv) and frequency (1 second). Theoretically, it requires no calibration except initial calibration using a certain concentration of NO_2 mixed gas. Another advantage of CAPS is that it does not require conversion of neither NO_2 to another species nor the sensitivity to other nitro containing species (such as HNO3, nitrate, PAN, etc.). Therefore, it is different from the standard chemiluminescence-based monitors which have uncertainties from the interferences with other reactive nitrogen species. The detailed principles of the CAPS system have been demonstrated in(Kebabian et al., 2005, 2008).

2.4 Ozone monitor

The Dual Beam Ozone Monitor is used for analyzing on-road O_3 together with CE DOAS in Hong Kong. It is designed to enable accurate measurements of atmospheric O_3 over a wide dynamic range (1 ppbv to 100 parts-per-million (ppmv)) and measures the absorption of ultraviolet light at 254 nm. The sample air is drawn by an air pump into

two separate 15 cm long absorption cells fitted with quartz windows at a flow rate of 1.5 L/min. Ozone is measured based on the attenuation of light emitted by the mercury lamp passing through these two absorption cells. The intensities of light passing through ozone-scrubbed air ($I_0(\lambda)$) and unscrubbed air ($I(\lambda)$) are measured simultaneously. With the known light path and the absorption cross section for ozone (Molina and Molina, 1986), the O_3 concentration can be derived from the Beer–Lambert–Bouguer law (equation 2.2). The pressure and temperature within the absorption cells are measured so that the O_3 concentration can be expressed as a mixing ratio in ppbv.

2.5 GEOS-Chem chemical transport model

The global 3-D GEOS-Chem Chemical Transport Model (CTM) was used in this study to simulate the transportation of major aerosols and trace gases including NO_2 in the atmosphere. This model is driven by assimilated meteorological fields from the Goddard Earth Observing System (GEOS) of the National Aeronautics and Space Administration (NASA) Global Modeling Assimilation Office (GMAO) (Bey et al., 2001). In this study, the GEOS5-FP meteorological data had a horizontal resolution of 2.0°(latitude)×2.5°(longitude), and a vertical resolution of 72 hybrid pressure-sigma levels. The temporal resolution of 1 hour were used to driven the GEOS-Chem CTM version 10-01. In total, there were 92 tracers included in the Universal tropospheric-stratospheric Chemistry eXtension (UCX) simulations (Eastham et al., 2014). Transportation of atmospheric components were calculated every 15 minutes with both 30 min resolution of the emission and the chemistry time step in the model.

3 Long-term observation of temporal patterns of NO$_2$ in Munich

The installation of the Munich DOAS measuring system has been introduced in Section 2.2. In this section, the method used for the calibration of LP DOAS viewing direction is introduced. The calibration is necessary for locating proper sites to install retro reflector arrays before all measurements can be taken. The difference between with and without intrumental background correction which can cause an obvious error is also discussed. In addition, several intercomparisons among intruments were implemented. NO$_2$ levels at different measurement heights and locations are presented. The diurnal patten of NO$_2$ and the city traffic are analyzed. Furthermore, long-term NO$_2$ trends measured by LP DOAS and satellite OMI are compared.

3.1 LP DOAS NO$_2$ measurements

Three LP DOAS instruments are setup on the roof of Meteorological Institute, the LMU of Munich. In this study, several measurement setups were realized Figure 3.1. According to the different length of light paths, different amounts of retro reflector arrays were required. Setup 1 has been operated since December 2015 with a total absorption path of 3828 m across English Garden, the city park of Munich. Three retro reflector arrays were located on the roof-top of Hilton hotel building at ∼48 m height at opposite ends of our institute. Setup 2 has been operated since January 2017 with a total absorption path of 1142 m covered three blocks around the university area to St. Ludwig Munich (Church) and ∼40 m above the ground. Setup 3 had been operated from July 2015 untill April 2017 with a total absorption path of 828 m across two blocks to reach the roof of the building of Technical University Munich (TUM) at ∼28 m height. Setup 4 had been operated from July 2016 untill August 2017 with a total absorption path of 816 m across three blocks to reach the roof of the building of Physics department of LMU at ∼24 m height. The measurement path covers the university campus, public park, residential areas and areas with heavy traffic.

A measurement sequence started with taking the LED reference spectra including dark current, offset, and background spectrum. The LED reference spectra were taken by using a shortcut system consisting of an aluminum diffuser plate that is moved up and down several millimeters in front of the fiber bundle. The measurement of the LED reference spectrum normally took 10 s. Then an atmospheric background spectrum was taken by blocking the LED using a shutter with a fixed integration time of 1 s and 10 scans. Afterward, the atmospheric spectrum with a maximum of 10 scans was taken. Each
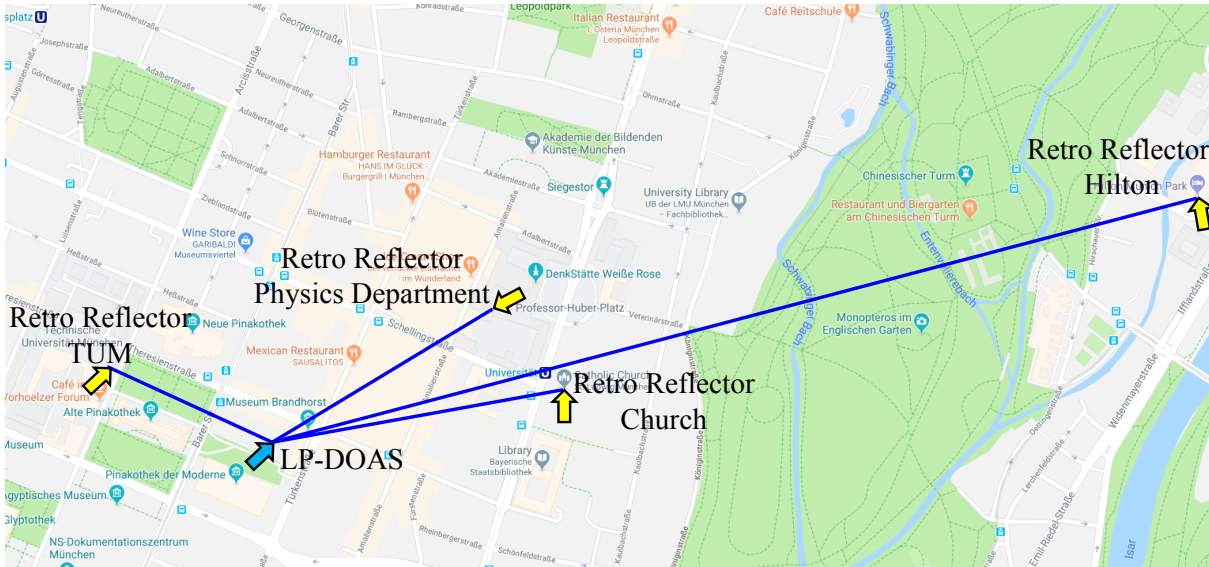
Figure 3.1: Map of Munich city center and 4 optical paths of three LP DOAS instruments.

scan of a spectrum has a peak intensity about $60\% - 80\%$ saturation of the detector and typically requires $60\,\mathrm{ms} - 1000\,\mathrm{ms}$ depending on visibility and instrument setup. The total sampling time (the product of number of scans and exposure time for each scan) was limited to $60\,\mathrm{s}$. A full measurement sequence took between $30\,\mathrm{s}$ and $90\,\mathrm{s}$ depending on visibility conditions.

3.1.1 Compare to opening angle of the telescope

All LP DOAS instruments can measure along multiple light paths within the vertical and horizontal motors movement range. Measurements of several retro reflectors over a large range are possible one after another. In order to achieve this, the certain scanning area for the motor movement range has to be identified first.

The total adjustable range of a stepper motor for both vertical and horizontal axises technically is 4×10^5 motor steps, $+/-\ 15\,\mathrm{mm} = +/-\ 1.07°$. There was a camera on each telescope to record the line-of-sight direction of the fixed telescope. Once the relation between the motor step and the image pixel is known, the scanning area can be calculated. In order to check the accuracy of our motors and identify the scanning area, we set up 2 retro reflect arrays on the roof of the TUM building, 4.5 meters away from each other in horizontal direction. Considerable scans of a larger scan area were then carried out to record the relative difference of the position between the two reflector arrays in motor step counts. A script was used to automatically move both vertical and horizontal motors back to the home position, scanning an area of 3×10^5 vertical and 2×10^5 horizontal motor steps with an accuracy of 2000 motor steps. As a result, it returned the intensity of the tested area (Figure 3.2a). Since the single way from the telescope to these two retro reflector was 414 m, the total scanning angle was around 2.2°. The maximum of the recorded spectrum in the first retro reflector was located at 4.6×10^4 motor steps,
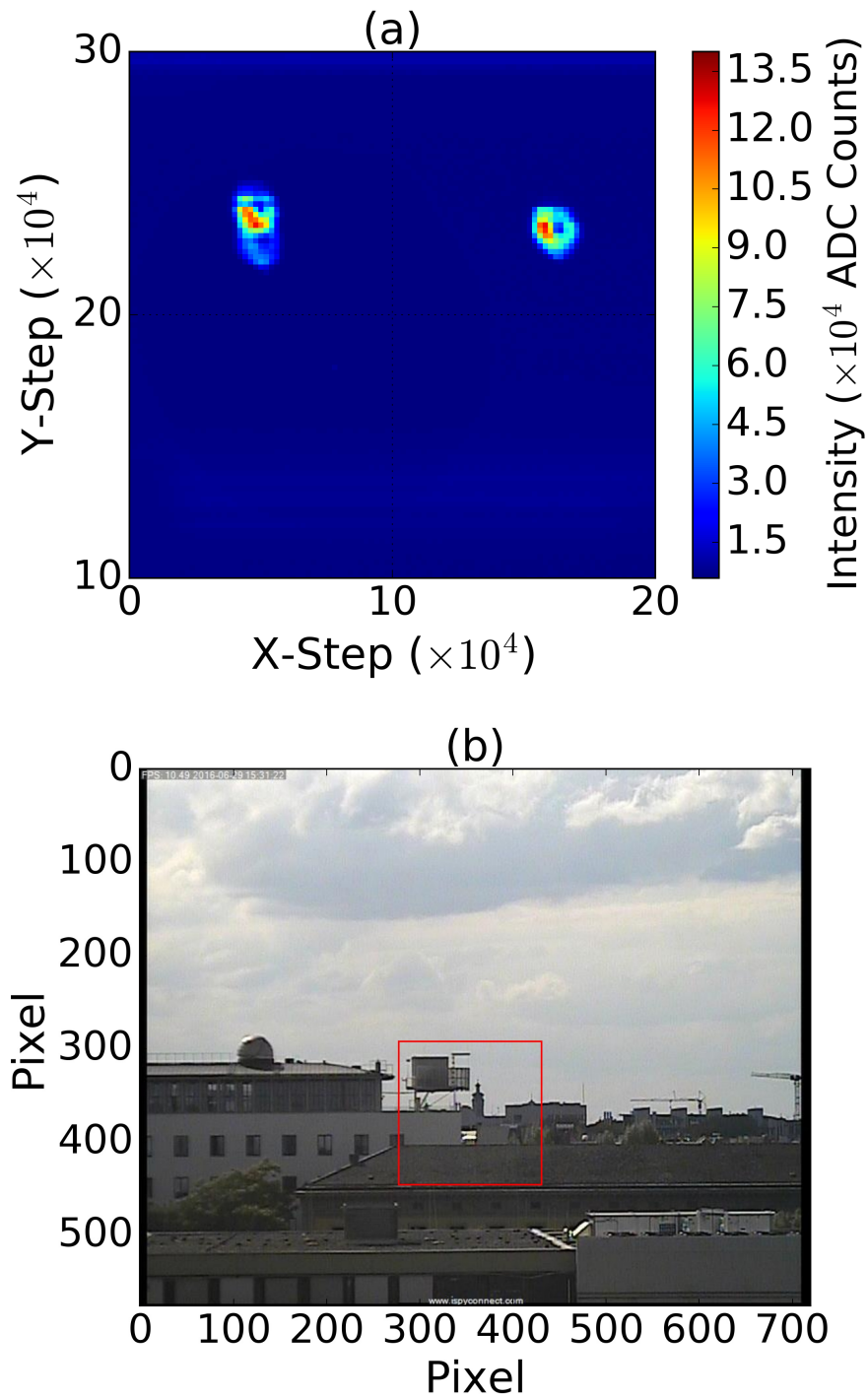
Figure 3.2: (a)The telescope scanning area. (b) A picture taken by the camera on LP DOAS instruments. The red rectangle is the full scanning area

while the maximum of the second retro reflector had a horizontal position of 1.58×10^5 motor steps. As shown in Figure 3.2b (a picture from the telescope), horizontal positions

of these 2 retro reflector arrays were Pixel 280.4 and 323.5, respectively. By caculation, 1 pixel is equal to 2604.7 motor steps. According to this conversion factor and the known position of either retro reflector array, the total scanning area of LP DOAS can be located. We also implemented this method to identify the possible scanning area of the LP DOAS towards the retro reflector array of the Hilton hotel (as shown in Figure 3.3). Accordingly, another retro reflector array was setup on the Church.
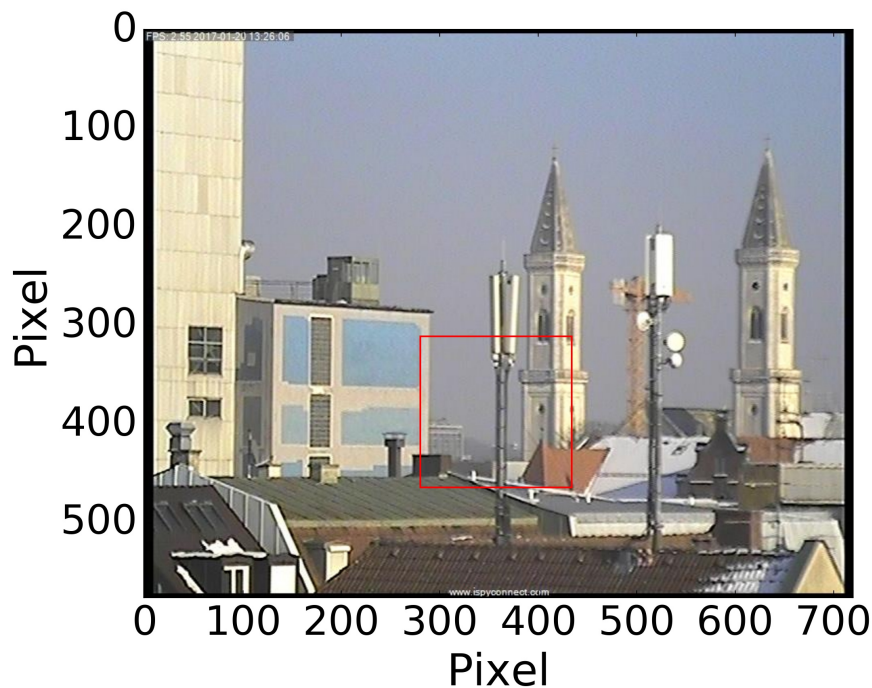
Figure 3.3: A picture taken by the camera on one of our LP DOAS instruments. The red rectangle is the full scanning area

Depending on the location and configuration, a wind shield or hard weather conditions could affect this system, such as the telescope vibration or the reduced lifetime of the motor and gearing. As shown above, since our instruments were set up on the roof and measurement light paths were up to several kilometers (single way to the retro reflector array), strong wind condition cannot be avoid and a tiny movement of the telescope could lead to the lost of reflected light signal. In addition, a so called mirage could lead to a bending of the light path. As a result, relative position of the retro reflector array would be changed along with temperature changes. Since the active DOAS method requires a precise location of the reflector array, we used rectangular spiral searching algorithm around the presumed retro reflector array position to do the optimization of the light beam in case of complete intensity loss. The accuracy of searching steps has to be adjusted according to the length of light path and the size of the retro reflector array. The light path optimization of the LP DOAS towards the retro reflector array of TUM had an accuracy of 2000 motor steps, while that of the LP DOAS towards the retro reflector array of Hilton got an accuracy of 1000 motor steps.

3.1.2 Instrumental background correction

The measurement time for one spectrum is defined by the number of averaged scans and the exposure time for each scan. The signal noise will be added up for every scan and the accuracy will go down when either of those two numbers are chosen too low. Each measured spectrum is composed of several superimposed signals, only the signal from trace gas absorption is what we need to retrieve the concentration of the trace gas that is detected. To achieve this purpose, other signals have to be subtracted from the measured total spectra. In our LP DOAS instruments, the light source was never turned off during measurement period so as to avoid any spectral instabilities. Because of this design, the CCD detector background signal is consist of the electronic offset and dark current spectra when no light enters the spectrometer. There were another two background spectra: the measurement background and the lamp spectrum background which must not be ignored.

As described in Section 2.2.1.1, there were two shutters (S1 and S2 in Figure 2.4) in the whole system, one was equipped with the optics and the other was placed in front of the end of transmitting and receiving fiber. In one complete measurement, four spectra were recorded. The controller first moved in both S1 and S2 to record a lamp spectrum background (I_{scbg}). Afterwards, S1 was moved out while keeping S2 stayed in to take a spectrum of the lamp (I_{sc}). Before taking a real atmosphere measurement, a measurement for background spectrum (I_{mbg}) had to be recorded first by moving S1 in and S2 out simultaneously. At the end, the measurement spectrum(I_m) was taken while the S1 and S2 both were moved out. For testing the proportion of the error coming from this two background spectra, we implemented the test during the night (in case any scattered light would come inside to the telescope) and covered each telescope of LP DOAS instruments with dark material to avoid the city light transmitting into the aerosol. Two tests were deployed: 1) Full range of motor steps were tested in order to detect whether the error changes within different motor positions. 2) A certain motor position with the wavelengths from 432.0 nm to 457.6 nm (corresponding to the channels from 1716 to 1999), which had same wavelength range as the DOAS fit of our measurements, were tested to investigate the dependence of the error on the wavelength. The intensity of all spectra were recorded, each test spectrum was taken averaged 10 scans and each scan took 10 ms.

Figure 3.4 shows the error comparison with and without correcting those two background spectra for full scan area. Since the whole test basically had no trace gas absorption involved and should have not receiving light collected to the fiber. Theoretically, $I_m = 0$. However, in the real measurement test shown in Figure 3.4a, there are up to 4% light ($\frac{I_m}{I_{sc}}$), which means 3-4% light came directly back to the spectrometer without any trace gas absorption but would be added to the receiving signal with trace gas absorption. The retrieved trace gas concentration would be underestimated. Figure 3.4b shows the difference between the corrected measurement spectrum ($I_m - I_{mbg}$) and the corrected lamp spectrum ($I_{sc} - I_{scbg}$). The proportion of the error was no longer strongly pronounced ($< 0.1\%$), which revealed higher accuracy than before by implementing the correction. In addition, both plots (Figure 3.4a and b) indicate the error is constant in the area of main mirror within the different motor position.

In addition, the error that was calculated as the ratio of $\frac{I_m}{I_{sc}}$ shows a strong wavelength
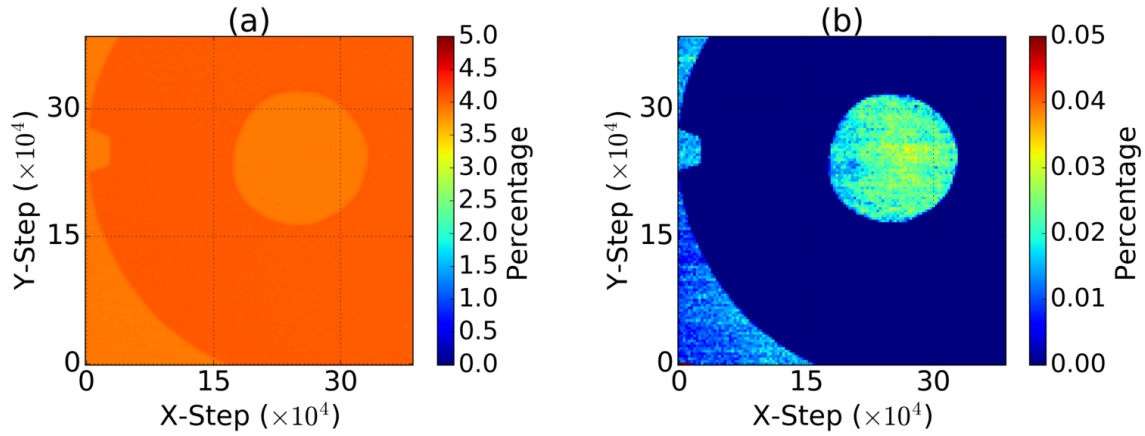
Figure 3.4: Error percentage of full range scanning with an accuracy of 2000 motor steps: (a) the ratio of the measurement spectrum with covered telescope and the lamp spectrum; (b) the ratio after correcting the measurement background and lamp spetrum background.

Figure 3.5: Error percentage of the channel from 1716 to 1999 at a certain motor position: (a) the ratio of the measurement spectrum with covered telescope and the lamp spectrum; (b) the ratio after correcting the measurement background and lamp spectrum background.

dependency (see Figure 3.5a), ranging from 3.5 % to 6 %. This suggests the spectrum we measured was seriously affected by other signals, except for the noise from the detector. With the correction of I_{mbg} and I_{scbg} (Figure 3.5b), the structure of wavelength dependency was disappeared. An error sequence of around 0.2 % was obtained which could be considered as instrument noise.

3.2 NO$_2$ measurement comparisons

Intercomparison and harmonizing instrument is an essential prerequisite for the reliable measurement campaign. Since each instrument error is individual, several intercomparison studies of different instruments for measurement of random NO$_2$ concentrations were carried out. Instruments including three LP DOAS and an CE DOAS have been calibrated independently. The results obtained from these instruments were highly comparable. More results will be introduced afterwards in this section.

3.2.1 Intercomparisons of LP DOAS and CE DOAS

(a)   (b)
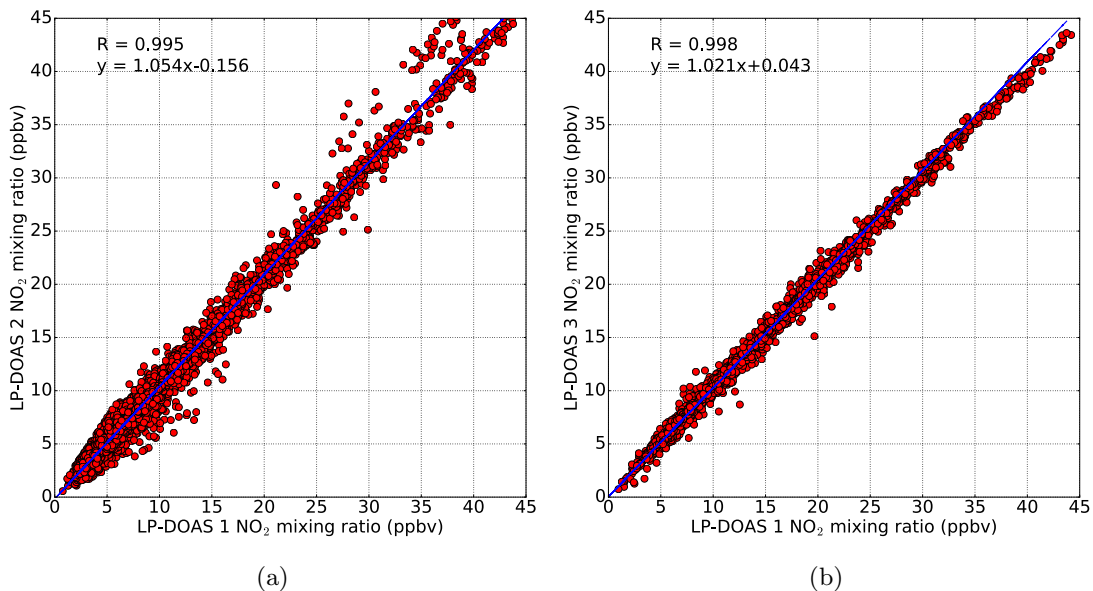
Figure 3.6: Scatter plots and orthogonal linear regression analysis of side by side comparison of three LP DOAS instruments. Data from the whole measurement period were averaged in 5 min bins.

Two intercomparison measurements of three LP DOAS were deployed for 10 days. All three instruments were aimed towards the retro reflector array on the Church. To illustrate this procedure, Figure 3.6 displays and compares the NO$_2$ mixing ratio measurements of the three LP DOAS instruments. Relevant statistical parameters (correlation coefficient, slope and intercept of the orthogonal linear regression fit) are indicated. The uncertainty of each LP measurement is less than 1 ppbv. Good agreements in the three LP DOAS instruments were observed. The scatter plots are compact, the slopes and correlation coefficients are close to unity, and intercepts are close to zero. Correlation between 1_{st} and 2_{nd} LP DOAS was slight higher than that between 1_{st} and 3_{rd} LP DOAS, which might be ascribed to a larger noise of the corresponding instruments. All in all, three LP DOAS showed good sensitivity and stability.
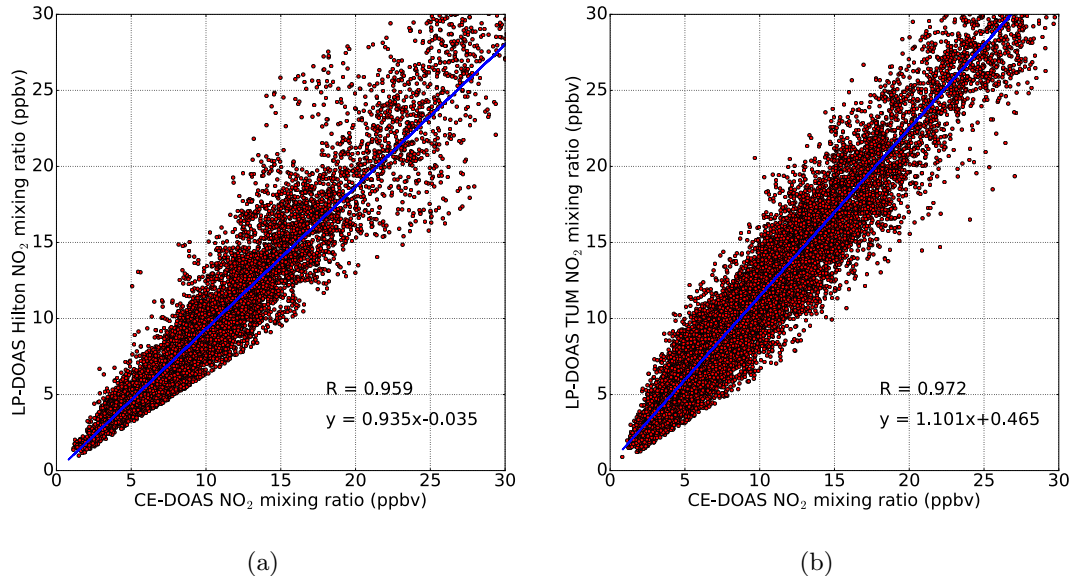
Figure 3.7: Scatter plots and orthogonal linear regression analysis of side by side comparison between CE DOAS and (a) the LP DOAS measuring the area to the Hilton Hotel, (b) the LP DOAS measuring the area to TUM building. The data from the whole measurement period were averaged in 2 min bins.

To proceed further, CE DOAS was placed on the roof for 20 days to compare to LP DOAS instruments towards the retro reflector array of the Hilton Hotel (LP DOAS-Hilton) and TUM building (LP DOAS-TUM), respectively. The CE DOAS performed very frequent measurements with every 30 s, while LP DOAS measured the average NO$_2$ in 1 to 2 min depending on the weather visibility. All data were averaged to 2 min frequency for comparison. The scatter plots displayed in Figure 3.7 illustrate similar high agreement of CE DOAS with two LP DOAS instruments: correlation coefficients were close to unity; slopes deviated by less than 10 % from the CE DOAS measurement; and intercepts were close to zero. Higher value for the slope and larger intercept values and corresponding uncertainties were found for the LP-DOAS-TUM. These differences may related to the difference of measured area. the LP DOAS-TUM measured an area of 2 blocks which were full of busy traffic, whereas the measured area of LP-DOAS-Hilton were over 3 blocks and a large city park (English Garden) which had relative much lower polluted NO$_2$.

In order to have a better insight of NO$_2$ concentration for different areas and their temporal changes, measurements of each instrument were averaged separately into diurnal variation with 2 min resolution shown in Figure 3.8. They all showed significant diurnal variability and similar variation pattern with higher values during the morning, lower values at noon, and slightly increase in the afternoon. All measurements observed elevated NO$_2$ levels during morning (6:00 to 8:00). However, the absolute concentration (ppbv) measured for different directions varied in a large range. The NO$_2$ of LP DOAS-TUM measured up to 15 % higher than the roof-level of CE DOAS and 40 % higher than the
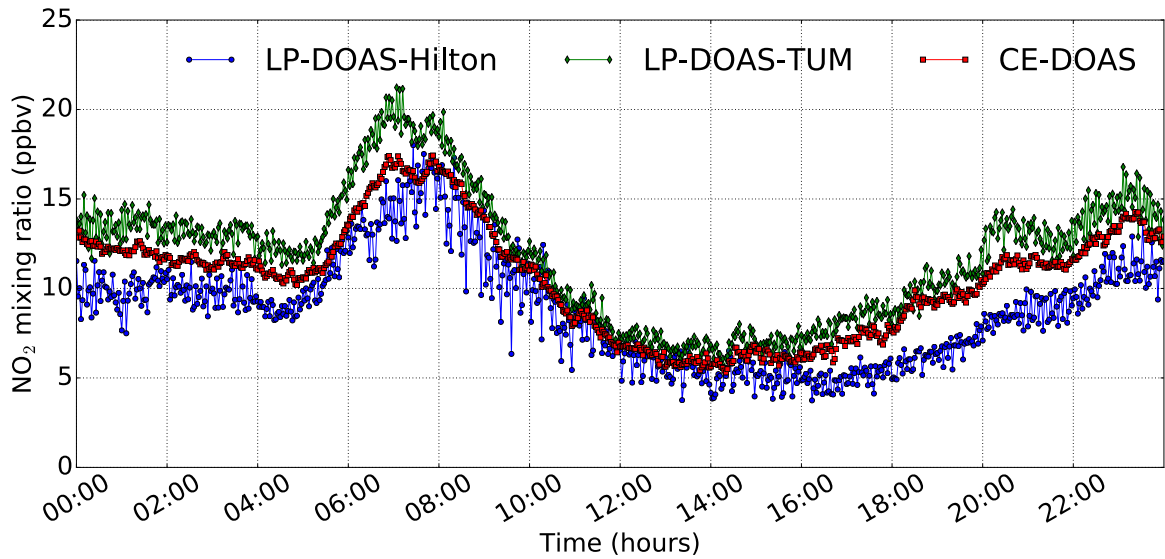
Figure 3.8: Diurnal variation comparison of side by side comparison between CE DOAS and LP DOAS. The data from the whole measurement period were averaged in 2 min bins.

LP DOAS-Hilton. These differences were mainly due to strong spatial variations of NO$_2$.

3.2.2 Comparisons of roof- and ground-level NO$_2$ measurements

In order to examine the difference between ground- and roof-level NO$_2$ concentrations which are closely relevant for most pedestrian, CE DOAS was setup in front of MIM building about 10 m distance next to the main street and at the back yard away from main road for 2 weeks, respectively. The time resolution of both measurements were adjusted to 2 min for comparison. As shown in Figure 3.9(a) and (b), CE DOAS measurement was highly correlated with LP DOAS measurements. In addition, the back yard measurement of CE DOAS was 1 % higher than roof-level measurement, while the measurement more close to the street was 22.7 % higher than the others. This was mainly due to the different measurement locations. NO$_2$ of the near-street location was affected by the traffic emission more significant than the back yard and roof-top. For further investigating the horizontal dilution effect, we moved the CE DOAS to the corner of the street and measured the roadside NO$_2$ for 2 hours in total. All measurements were averaged to 1 min time resolution for comparison (Figure 3.9(c)). The Pearson correlation between roadside measurement and roof-level measurement was much lower. In addition, the measured NO$_2$ of roadside was on average 3.2 times higher than roof-level. This discrepancy for the roadside measurement was generally on account of the sampling location which was the closest to the street and highly influenced by on-road traffic emission.

Based on above results, an extrapolation on the long-term LP DOAS measurements was implemented to get estimated NO$_2$ mixing ratio of near-street and roadside level

(a)

(b)

(c)
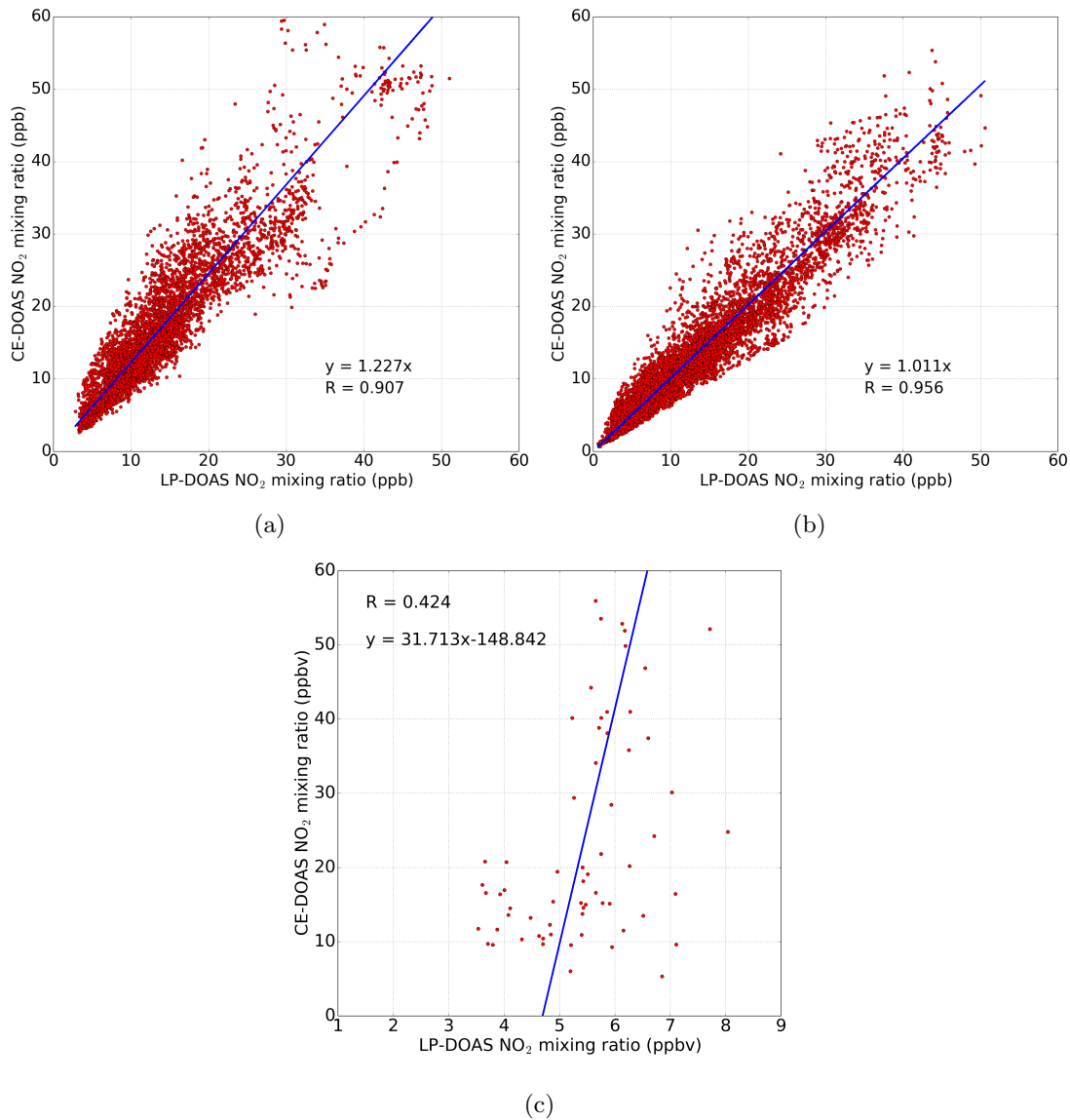
Figure 3.9: Scatter plots and orthogonal linear regression analysis of LP DOAS roof-level measurements with (a) the front yard CE DOAS measurements, (b) the back yard CE DOAS measurements on the ground, and (c) the roadside CE DOAS measurements.

(shown in Figure 3.10a and b, respectively). The near-street level of NO_2 was still below the hourly WHO AQG which suggests no great harm for pedestrian's health. However, 15.7 % in total of the estimated roadside NO_2 level exceeded the hourly guideline.
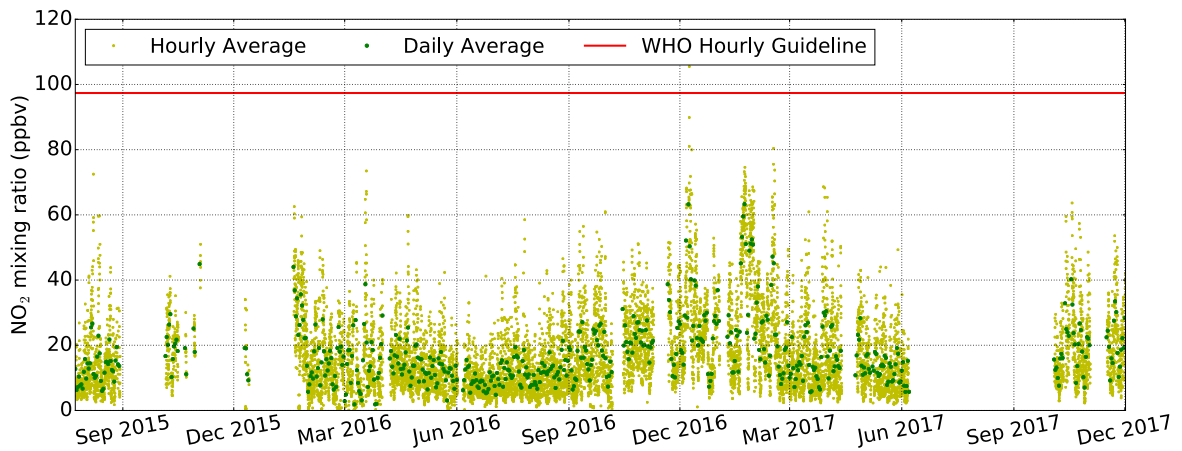
(a)
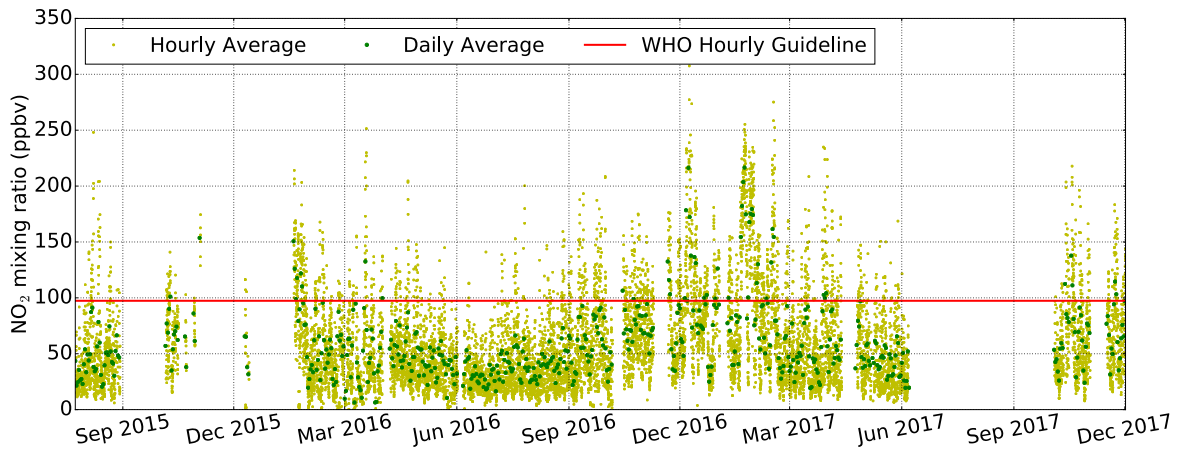
(b)

Figure 3.10: Hour-average and day-average NO$_2$ of near-street ground measurements (a) and roadside measurements (b) by extrapolating the LP DOAS roof-level measurements to the ground-level from 2015 to 2017. The red line is the hourly WHO AQG.

3.3 Diurnal variations of NO$_2$ and city traffic

3.3.1 Local air quality monitoring network and the city traffic information

Ambient NO$_2$ data in Munich were acquired from the air quality monitoring network of Bavaria that is operated by the LfU. The air quality monitoring network comprises 8 am-
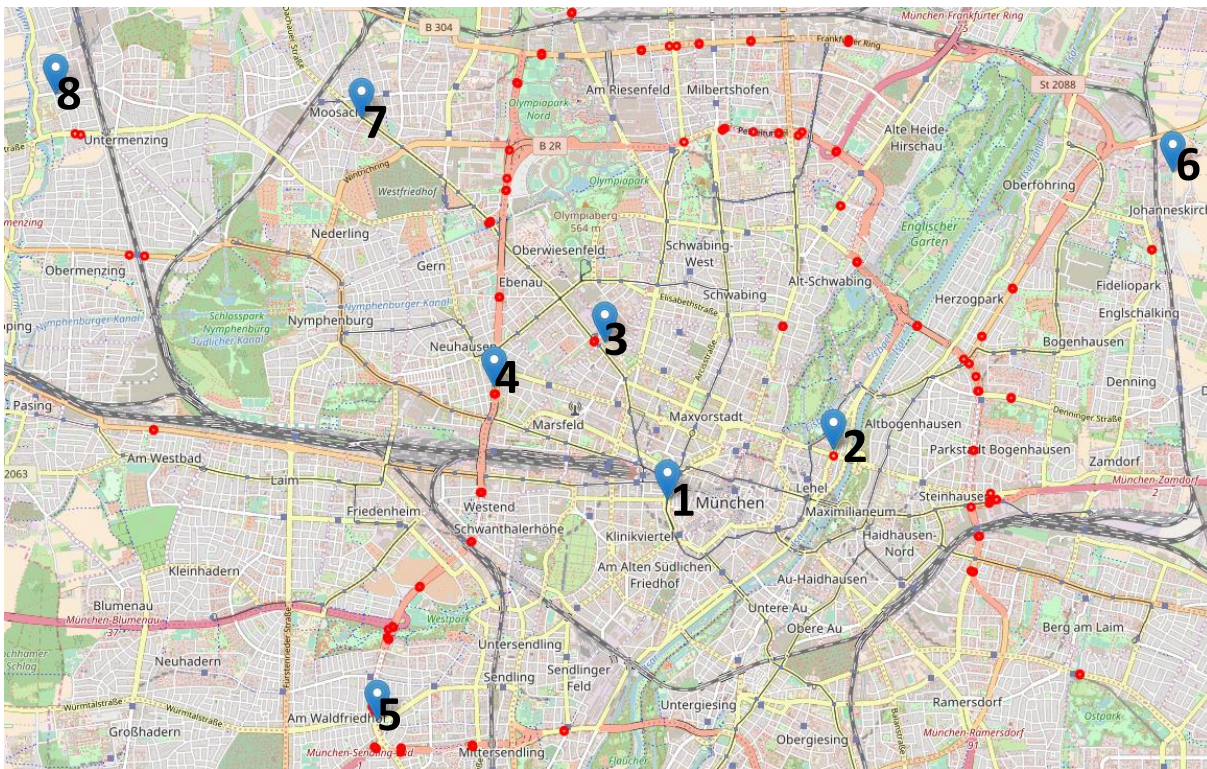
Figure 3.11: The air quality monitoring stations numbered from 1 to 8 are Stachus, Prinzegentenstr, Lothstreet, Landshuter Allee, Luise-KieselbachPlatz, Johanneskirchen, Moosach, Allach, respectively. Red dots are traffic counters that distributed mainly on the busy streets.

bient monitor stations in Munich and they cover both urban and rural areas. Since 2012, only five stations located in Allach, Lothstrasse, Stachus, Landshuter Allee and Johanneskirchen (No.1–5 in Figure 3.11) have been activated for measuring. The NO$_2$ and NO$_x$ concentrations were measured by in-situ NO$_x$ analyzer. In addition, the Munich traffic counting data collecting by the Department of Public Order (Kreisverwaltungsreferat or KVR) of Munich were used as traffic density information to compare with hourly NO$_2$ concentrations of three air quality monitoring stations and long-term LP DOAS NO$_2$ measurements. Location information of the air quality monitoring stations and the traffic detectors in the city centre are shown in Figure 3.11.

3.3.2 Correlations of traffic density with NO$_2$

Traffic count measurements were analyzed together with LP DOAS and LfU monitor stations data to investigate the correlation between the ambient NO$_2$ and the traffic density. Traffic count measurements taken within 2 km radius of the five LfU monitor stations were averaged over 2 years (2016 and 2017) and displayed together with average diurnal variation of NO$_2$ of LfU (Figure 3.12 a, b). Both traffic and NO$_2$ of all stations showed significant diurnal variability with a sharp increase since 4:00 in the morning and
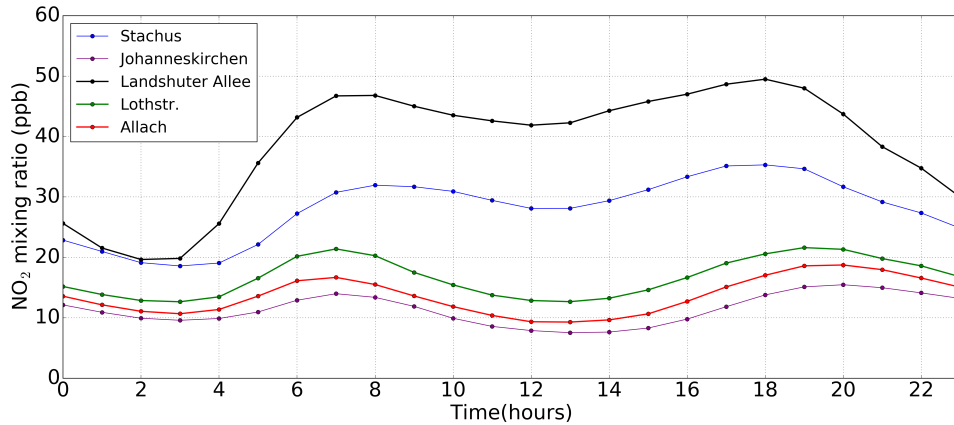
(a)
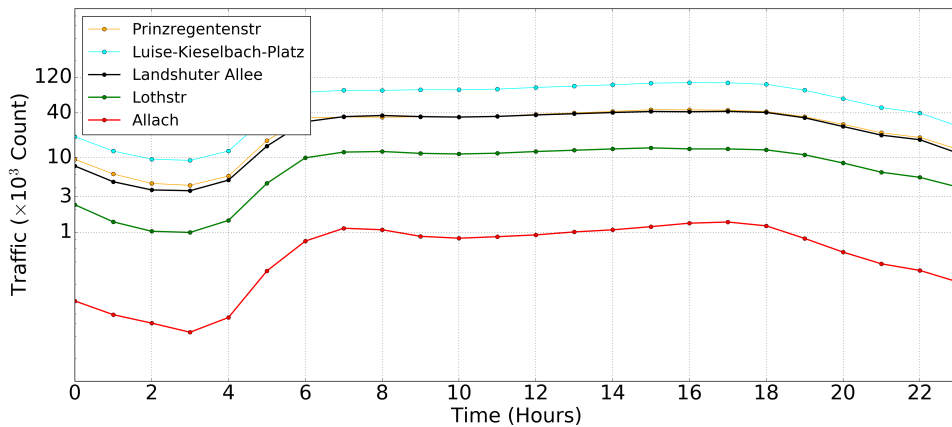
(b)

Figure 3.12: 2-year average diurnal cycle of NO₂ measured by LfU monitoring stations in (a) and traffic count data within 2 km radius of specific stations in (b).

reaching the peak during the morning rush hour from 6:00 to 8:00 and a smooth rising around 18:00. However, the absolute concentration of NO₂ and traffic counts measured by different stations varied in a wide range. Since not every station measured both traffic and NO₂ level information, only Landshuter Allee station, Lothstreet station and Allach station were available to compare. Among these three stations, the traffic density of Allee station was the lowest whereas the Landshuter Allee station was the highest. A same condition was observed in NO₂ levels. In addition, traffic around Landshuter Allee station was on average 68 % more than Lothstreet station and 97 % more than Allach station, while NO₂ of Landshuter Allee station was 57 % higher than Lothstreet station and 65 % higher than Allach station. Due to the different locations, the Allach station

located outside the city center measured the residential area with relative rare traffic, the Landshuter Allee station positioned on the city-ring road captured the high-density traffic emissions, and the Lothstreet station located in the city centre residential area was generally affected by city traffic.
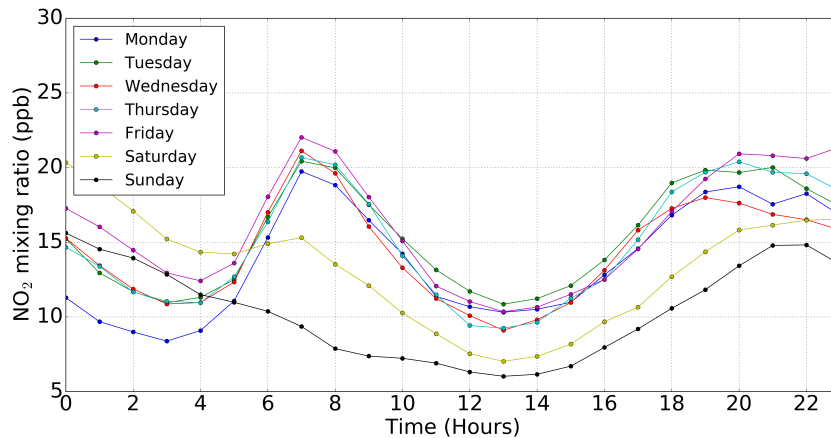
(a)
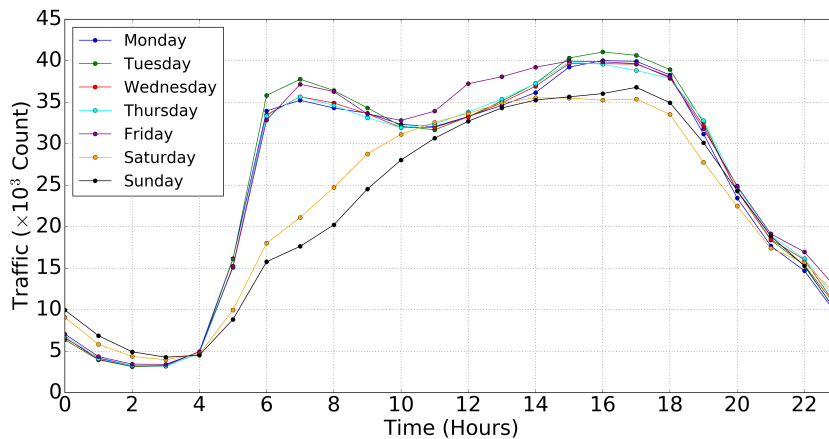
(b)

Figure 3.13: 2-year average diurnal pattern for each day of the week of NO_2 measured by LP DOAS (a) and coinciding traffic counts(b).

Furthermore, the spatial and temporal distribution of NO_2 changed with the day of the week. Traffic load was highly dependent on human activities which typically fall into a 7 days cycle. Therefore, all LP DOAS measurements and traffic counts of all inner-zone sensors in 2016 and 2017 were sorted and averaged into 24 hours in a day for each day of the week (Figure 3.13) so as to investigate weekly pattern of NO_2 and traffic density for capturing the differences between traffic and anthropogenic emissions during
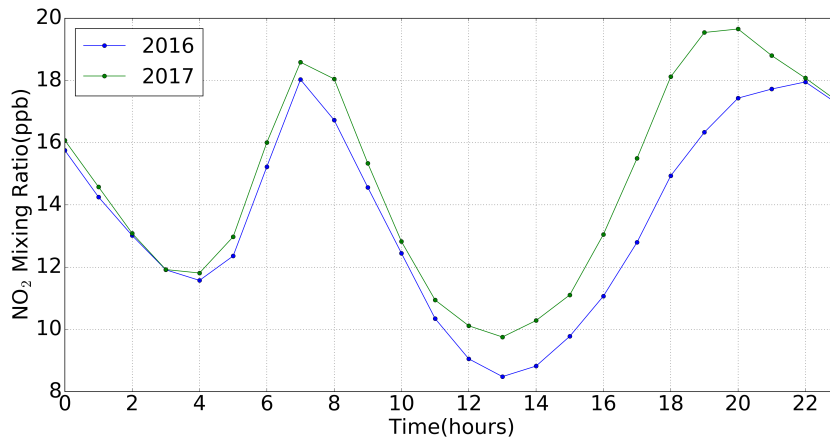
(a)
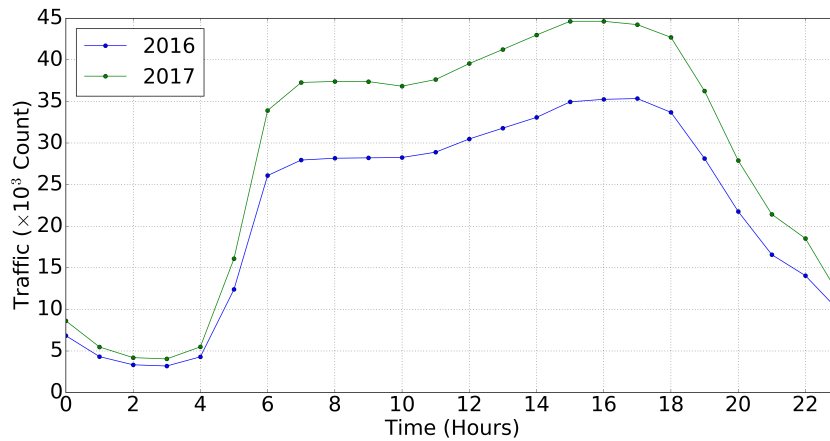
(b)

Figure 3.14: Annual average diurnal variation of the LP DOAS measurement (a) and the traffic count data (b).

weekdays and weekend. The diurnal pattern of traffic and NO_2 both illustrated different characteristics between weekdays and weekend. The LP DOAS measurement indicated the NO_2 concentration was on average 11 % lower on Saturday and 30 % lower on Sunday compared to weekdays. However, the morning rush hour peak of NO_2 was significantly reduced by 24 % on Saturday and 52 % on Sunday, while the evening rush hour (18:00 to 20:00) peak presented a less pronounced reduction of 36 % on Sunday. Traffic counts and the LP DOAS showed similar diurnal variation pattern and weekend reduction, except that the evening rush hour was 2 hours ahead (16:00 to 18:00). As indicated by the traffic count measurement, the traffic was on average 12 % lower on Saturday and 14 % lower on Sunday compared to weekdays. During the morning rush hour (6:00 to 8:00) peak of

traffic substantially decreased 39 % on Saturday and 49 % on Sunday, while the evening rush hour peak showed a smooth declining of 11 % on Saturday and 6 % on Sunday. Besides, NO$_2$ level on Monday was slightly lower than the rest of weekdays, while the traffic counts on Monday had no difference to others. This may be due to the lifetime of NO$_2$, namely much less NO$_2$ emitted on Saturday and Sunday were largely diffused. Therefore, the NO$_2$ measured on Monday was mainly emitted on the same day, while the measured NO$_2$ of midweek were the sum of the emissions of the current day and previous days. For further comparison, the annual average diurnal pattern of traffic counts and NO$_2$ in 2016 and 2017 are shown in Figure 3.14. NO$_2$ increased 8 % on average and traffic increased 29 % from 2016 to 2017.

All relative changes of traffic were highly correlated to the changes of NO$_2$ levels. However, the reduction trend of NO$_2$ during the noon was not the same strongly pronounced in traffic tendency, due to the emissions diffused rapidly during the day by wind. In addition, the sharp decreasing traffic counts during the night was not observed in NO$_2$ diurnal pattern, since the dwell time of the emissions was increased during the night considering much lower wind speed (Brunner et al., 2015; Carapellucci and Giordano, 2013). These relative changes within a week in the diurnal cycle proved that traffic emissions were the main source of NO$_2$ in urban areas in Munich. This effect was strongly dependent on human activities. Traffic is declined during weekend as most of the residents do not work on Sunday, e.g., frequency of buses is reduced during weekend. Saturday has a less pronounced reduction effect comparing to Sunday, as Saturday could still be a travel day for some family in Munich.

3.4 Long-term NO$_2$ trends of ground-based and satellite observation

3.4.1 Converting OMI data to ground mixing ratio using modeled NO$_2$ profiles

The Emission Database for Global Atmospheric Research (EDGAR) version 4.2 (EDGAR4.2, 2011) was used in the simulations as the anthropogenic emissions database, while overridden with some regional inventories were available. The anthropogenic emissions over South East Asia were taken from the Intercontinental Chemical Transport Experiment Phase B (INTEX-B) inventory (Zhang et al., 2009a). The Model of Emissions of Gases and Aerosols from Nature (MEGAN) emission inventory version 2.1 was used to account for biogenic emissions in the simulations (Guenther et al., 2012). The black and organic carbon emissions were taken from the global emissions inventory introduced by Bond et al. (2007) while the biomass burning emissions of carbonaceous aerosols were taken from Global Fire Emissions Database version 3 (GFED3) (Van der Werf et al., 2010). Simulations were carried out from July 2012 to June 2014. Month-average data of the GEOS-Chem simulations were used as the OMI a-priori vertical NO$_2$ profiles in this study for converting the OMI tropospheric NO$_2$ VCDs to the ground level mixing ratios. Monthly vertical NO$_2$ profiles are shown in Figure 3.15.

Figure 3.15: 2-year monthly average NO$_2$ vertical profiles simulate by Geos-Chem Module from July 2012 to June 2014. The corresponding profile for each month is used to convert the NO$_2$ VCDs measured by OMI to ground mixing ratio (ppbv).

3.4.2 Comparison between the ground measurement and converted OMI observation

Satellite measurements are strongly affected by clouds as clouds shield ground level NO$_2$. Hence, for a better comparison with the LP DOAS data, OMI data with cloud fractions larger than 50 % which were significantly influenced by clouds, were filtered out. LP DOAS data from 12:00 - 15:00 UTC time, same as the OMI overpass time for Munich, were used for comparing with the gridded OMI data sets within 10 km and 50 km from the measurement site (Figure 3.16). In order to reduce the influence of clouds and local spatial variations, monthly mean data were used for the comparison. The uncertainty of
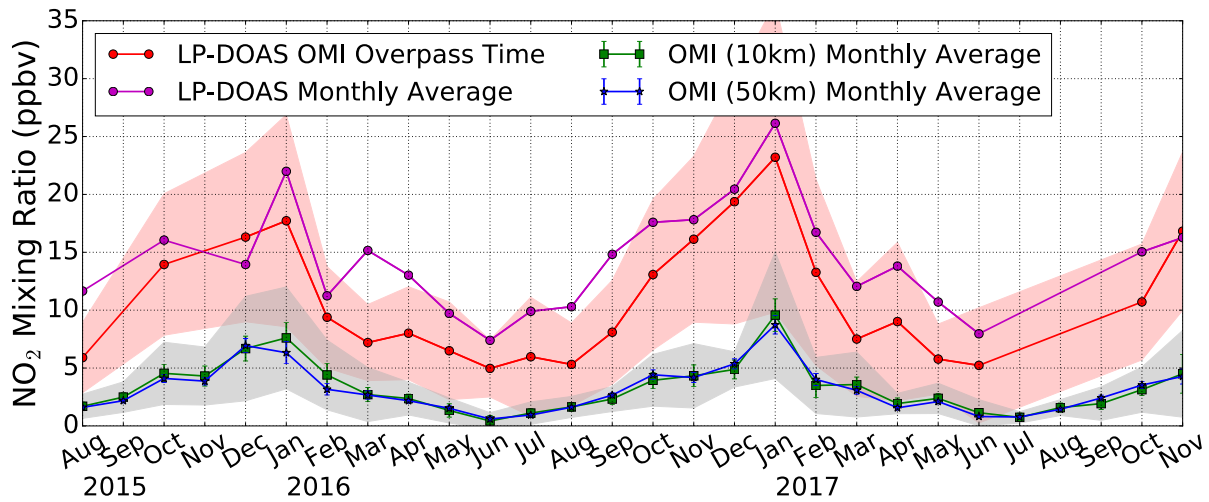
Figure 3.16: Monthly mean ground-level NO₂ mixing ratio. LP DOAS data are temporal averages around OMI overpass time (12:30 – 14:30 UTC). OMI data are spatial averages over pixels within a 10km and 50km radius of our institute. The red shadow indicate the variability of 1 σ (standard deviation) of LP DOAS measurements. The light gray regions indicate 1 σ variability of OMI data within 10 km.
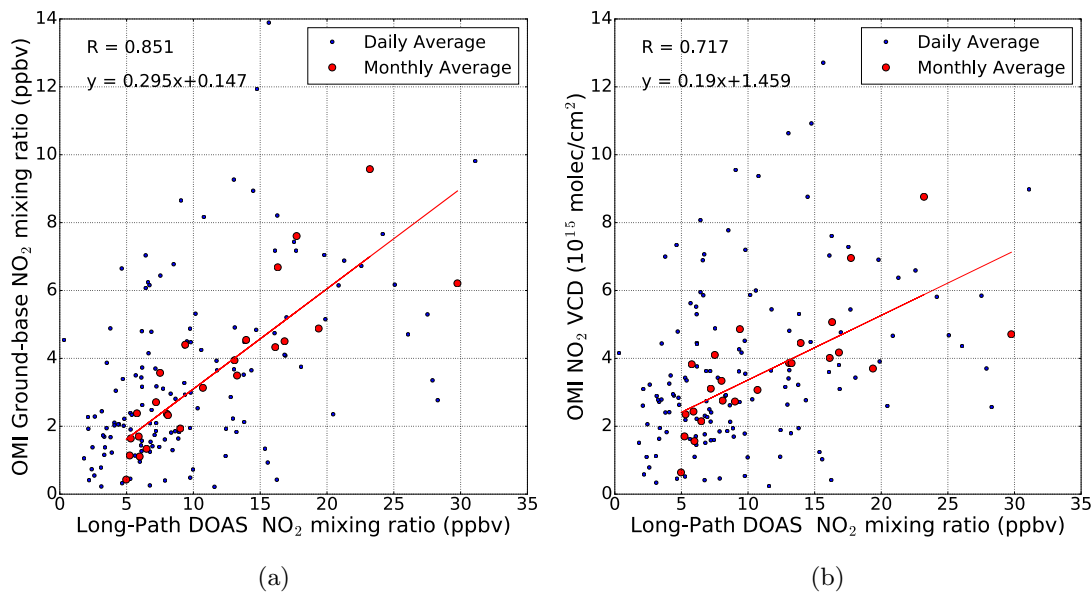
Figure 3.17: Correlation of LP DOAS measurements with retrieved NO₂ mixing ratio (ppbv) in (a) and VCD in (b) of OMI observation.

the LP DOAS measurements which was $< 1\,\mathrm{ppbv}\,/\,$measurement, is too small to be shown after averaging over years. Observation of LP DOAS and OMI both showed similar annual pattern with lower NO₂ values in summer and elevated NO₂ values in winter.

The Pearson correlation between the monthly means of LP DOAS overpass time measurements and OMI retrieved ground mixing ratio of NO$_2$ and VCDs within 15 km were 0.85 and 0.72, respectively (Figure 3.17). OMI and LP DOAS were correlated well, representing OMI measured reliable tendency of ground level NO$_2$. The discrepancy of correlation coefficients were mainly caused by the vertical profile used for the OMI retrieval and the conversion of VCDs to ground level mixing ratios. In order to show the influence of temporal averaging, monthly averages for all LP DOAS data are shown in Figure 3.16 as well.

As NO$_2$ has high temporal variability, increasing the averaging time would include data that OMI is not able to capture. Hence, the measurements of LP DOAS and OMI were less correlated with each other. Additionally, since OMI overpass time was not in between of local rush hours (introduced in 3.3), LP DOAS monthly average of all measurements on average were 50 % higher than NO$_2$ of LP DOAS during OMI overpass time for most of months, except for December, 2015 which had fewer measurements less than 6 days due to the instrument maintenance. OMI data averaged for a 50 km radius illustrated the influence of spatial averaging. By increasing the averaging area to increase spatial coverage would include other sources that were not related to local emissions measured by the LP DOAS. On average the monthly means of the OMI data within 10 km and 50 km were lower than the LP DOAS measurement of same overpass time by 7.4 ppbv and 7.5 ppbv, respectively. Therefore, it could be assumed that Munich and its surrounding area have similar emission sources.

The averaged variability of the NO$_2$ mixing ratios in winter (November to February) and summer (June to August) were 16.5 ppbv and are 5.5 ppbv. In most of the months, the error bars of OMI data, either within 10 km or within 50 km, do not overlap with the LP DOAS data, which indicated that there were some unknown systematic errors either in the OMI retrieval (Wenig et al., 2008) or in the VCDs to ground level mixing ratios conversion, or in both. One possible reason for the lower OMI values over Munich in comparison to the LP DOAS measurements was that the OMI a-priori profile used for converting the tropospheric NO$_2$ VCDs to ground level mixing ratios was averaged over a large area including large fractions of ocean and rural area with lower relative ground level mixing ratio. Underestimation of the relative ground level mixing ratios in the conversion profile led to underestimation of the ground level NO$_2$ and a total underestiation for the ground level NO$_2$ of about 69 %.

4 Analysis of spatial distribution of on-road NO$_2$ in Munich

In most German cities, the frequent exceedance of the WHO AQG for NO$_2$ concentrations has aroused wide concerns in the public. The NO$_2$ concentration can have a very strongly varying spatial distribution in urban areas. Furthermore, the emissions of NO$_x$ from on-road vehicles have a great contribution to the increasing trend of ambient NO$_x$ levels. Hence, capturing the NO$_2$ spatial distribution on the road is very important in order to identify pollution hot spots in the city.

In our study we performed extensive measurements for a period of two weeks in Munich in order to capture the spatial variability of NO$_2$. A combination of different spectroscopic instruments were applied, including mobile CE DOAS and CAPS spectroscopy, two mobile MAX DOAS, three stationary MAX DOAS, and three LP DOAS instruments. In a later phase of this project, this data set will be used for the Airborne Prism EXperiment (APEX) campaign in Munich.

4.1 Methodology

4.1.1 Mobile NO$_2$ Measurements

A CE DOAS, a CAPS and a 1-D MAX DOAS instruments were employed for mobile measurements using a sampling inlet which was positioned on top of the front left window of two vehicles at a height of about 1.5 m above ground. The measurements were performed for a one-week campagin in July 2016 to cover large part of the urban area in Munich. The measurements were performed on varying routes during the daytime to cover non-rush hours, morning and evening rush hours, which aimed to provide a better spatial coverage and to identify pollution hotspots. The scanning geometry of 1-D MAX DOAS measurement was fixed along the driving direction with an elevation angle of 22 °, aiming to avoid the effect of the buildings aside the roads (e.g. blocking the light) and to capture longer absorbing path lengths. A measurement sequence contained 1 measurement of scattered sun-light with elevation angles (α) of 90 ° (zenith) and 9 measurements with elevation angle of 22 °. Each measurement took around 1 min depending on the scattered sunlight intensity. For further supplementary information, one week bike measurements using CE DOAS were conducted in June 2016 to investigate NO$_2$ distribution in a small part of the city park (English Garden).

4.1.2 Stationary MAX DOAS measurement of aerosol and trace gases profile

The MAX DOAS instrument was setup next to LP DOAS system, on the roof of the MIM, at the LMU of Munich. The scanning geometry was set as the viewing azimuth angle (ϕ) of the telescope was adjusted to $0\,°$, $45\,°$, $90\,°$, $135\,°$, $180\,°$, $225\,°$, $270\,°$ and $315\,°$ with the lowest elevation angle of $1\,°$. A measurement sequence consisted of measuring scattered sun-light spectra with elevation angles (α) of $90\,°$ (zenith), $40\,°$, $20\,°$, $10\,°$, $7\,°$, $5\,°$, $3\,°$, $2\,°$ and $1\,°$. Each performed with 100 scans. The exposure time of each measurement was automatically adjusted depending on the intensity of the received scattered sunlight, in order to achieve similar intensities for measurements at all elevations and to further achieve similar intensity levels for all the measurements. A full measurement sequence took about 5 to 15 minutes depending on the scattered sunlight intensity.

As aerosols are typically emitted and formed close to the surface in urban areas, we assumed the a priori aerosol extinction profile followed an exponentially decreasing function with a scale height of 0.5 km. The aerosol optical depth (AOD) of the a priori aerosol profile was set to 0.12 for the retrieval at 477 nm. The uncertainties of the a priori aerosol profile were set to $50\,\%$ and the correlation length of the aerosol inversion was assumed to be 0.5 km. As the MAX DOAS measurements are more sensitive to aerosol and trace gases close to the instrument, we therefore divided the lowest 3.0 km of the troposphere into 15 layers with a thickness of 200 m for each layer. A fixed set of a single scattering albedo of 0.92, the asymmetry parameter of 0.68 and the ground albedo of 0.04 were assumed in the radiative transfer calculations.

The aerosol information obtained from the procedure described above was used for the differential box air mass factor (ΔDAMF) calculation for the trace gas profile inversion. The ΔDAMFs were calculated at a single wavelength for the retrieval of trace gas profile using the radiative transfer model libRadtran with the Monte Carlo simulation module MYSTIC (Emde et al., 2016). The ΔDAMF was assumed to be constant within the DOAS spectral fitting windows. In this study, vertical distribution profiles of NO$_2$ were retrieved at the O$_4$ absorption bands at 477 nm.

The atmosphere layer settings of the trace gas profile retrieval were as same as the one used in the aerosol profile retrieval. As the trace gas profile cannot be fully reconstructed by the small number of measurements, therefore, we used the optimal estimation method (Rodgers, 2000) with a two-step approach to regularize the inversion (Chan et al., 2018). The first step used a fixed and non-committal a priori to retrieve the trace gas distribution. The fixed a priori profile was then scaled to have the vertical column retrieved from the first run. The scaled a priori was used in the second run to retrieve the final result. In this study, the a priori was assumed to follow an exponential decrease function with a scale height of 0.5 km. The uncertainty of the a priori profile was set to $50\,\%$ of the a priori and correlation length was set to $0.5\,\mathrm{km}$ in the trace gas profile inversion. The NO$_2$ vertical column density (VCD) of the a priori was set to 1×10^{16} molec/cm^2.

4.2 Intercomparison of CE DOAS and CAPS

In our first intercomparison measurement, we placed the CE DOAS and the CAPS side by side on the roof of MIM building for 6 days. The measurement frequency for the CE DOAS and the CAPS were both set to every 2 s. One-minute average values of NO_2 were used for comparison. As shown in Figure 4.1, they are highly correlated. The scatter plots are compact, the slopes and correlation coefficients are close to unity, and intercepts are close to zero. These results confirmed the good agreement in the CE DOAS and the CAPS. Hence we were able to place the CE DOAS and the CAPS separately into two vehicles in order to cover an area as large as possible in one week.
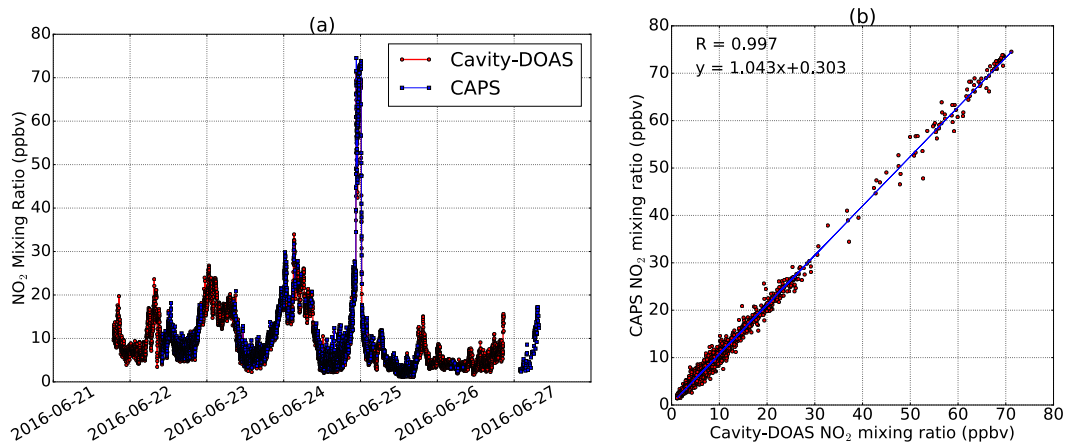
Figure 4.1: (a) The timeseries of the CAPS and the CE DOAS comparison measurements for 6 days. (b) Correlation coefficients of side by side comparison between the CE DOAS and the CAPS.

4.3 Normalization of the diurnal cycle

Since NO_2 concentrations have a very strongly varying spatial distribution in urban areas, capturing the NO_2 spatial distribution on the road could help to identify pollution hot spots in the city. However, measurements were taken at different times of the day, therefore, they were also affected by the diurnal variation. In order to separate the NO_2 spatial and temporal variability and show a representative spatial distribution of NO_2 in each city, an algorithm has been developed to fit long term diurnal cycles to LP DOAS date of the measurement day to normalize the time of the day dependencies. This algorithm was used to create normalized maps for Munich based on measurement campaigns. It is less depending on the outlines caused by the overpass pollution plume and can also interpolate data gaps due to instrumental problems and bad weather.

The algorithm normalizing for diurnal variations used the LP DOAS measurements of

atmospheric NO$_2$ of the same day by dividing through the daily mean NO$_2$ concentration. Then these values were averaged for each day of the week over a period of 2.5 years to obtain a representative diurnal NO$_2$ variation pattern. The normalized and averaged diurnal NO$_2$ variation pattern of the corresponding weekday was scaled and shifted to the normalized LP DOAS measurement for each day during the mobile measurement campaign. The inverse of the 1 standard deviation of the 2.5 years averaged and normalized NO$_2$ level was used as weighting in the linear regression to scale and shift the long term average diurnal pattern. In order to avoid single high value affecting the whole regression, normalized NO$_2$ level exceeded the 2 σ variation of the 2.5-year averaged and normalized NO$_2$ level were not considered in the regression process. Figure 4.2 shows the normalized NO$_2$ level measured by the LP DOAS in 2016. Normalized 2.5-year weekday mean NO$_2$ diurnal pattern, the diurnal pattern of scaled NO$_2$ measurement taken on each day in 2016 are shown as well. All data illustrated similar characteristics with a significant peak in the morning (6:00 to 9:00) rush hours. The corrected long term diurnal pattern was then used to correct for the diurnal effect of the mobile measurement. Mobile measurements were multiplied by the simultaneous NO$_2$ level of the resulting normalized LP DOAS diurnal pattern to obtain a more representative value for the measurement areas.

4.4 Spatial distributions of NO$_2$ in Munich

4.4.1 NO$_2$ mobile measurements by the CE DOAS and the CAPS

In order to have a better overview of major pollution hotspots in Munich, all measurements in 2016 were spatially averaged to a high resolution grid of 20 m × 20 m and were not corrected for the diurnal cycle in the first analysis (Figure 4.3a). These measurements covered mainly the major roads in the city of Munich, including motorway, ring-road, urban, sub-urban and rural area. Elevated NO$_2$ levels were mainly distributed over motorways and busy roads, where there is always a high traffic intensity, e.g. No. 2R ring-road, No.8, No.E54, No.95, No.96, No.99 motorways, Landsbergerstreet near Pasing , Wittelsbacherstreet and Isartalstreet along the Isar river, and Karlsplatz and Marienplatz in the city center. About 5.8 % of the on-road measurements exceeded the WHO one hour guideline value. About 6.6 % of the area in the city center showed NO$_2$ concentrations higher than the guideline. High NO$_2$ values over motorways were mainly due to the emission of heavy duty diesel vehicles, i.e., diesel trucks and buses. Moreover, traffic congestion and street canyon effect (Rakowska et al., 2014) were the major cause of elevated on-road NO$_2$ in the city center.

As described in section 4.3, on-road pollutants are mainly produced by vehicles and the traffic flow patterns have a large impact on pollutant distributions (Westerdahl et al., 2005; Kaur et al., 2007; Huan and Kebin, 2012; Rakowska et al., 2014; Fu et al., 2017). This effect was normalized using the simultaneous LP DOAS measurement. The normalized spatial distribution of on-road NO$_2$ is shown in Figure 4.3(b). The normalized data were now average data representative for the whole day. NO$_2$ levels over 80.1 % regions were significant elevated (>1 ppbv) after applying the normalization, in particularly for the residential area and highways such as Neupelach and Moosach district, while 8.1 %
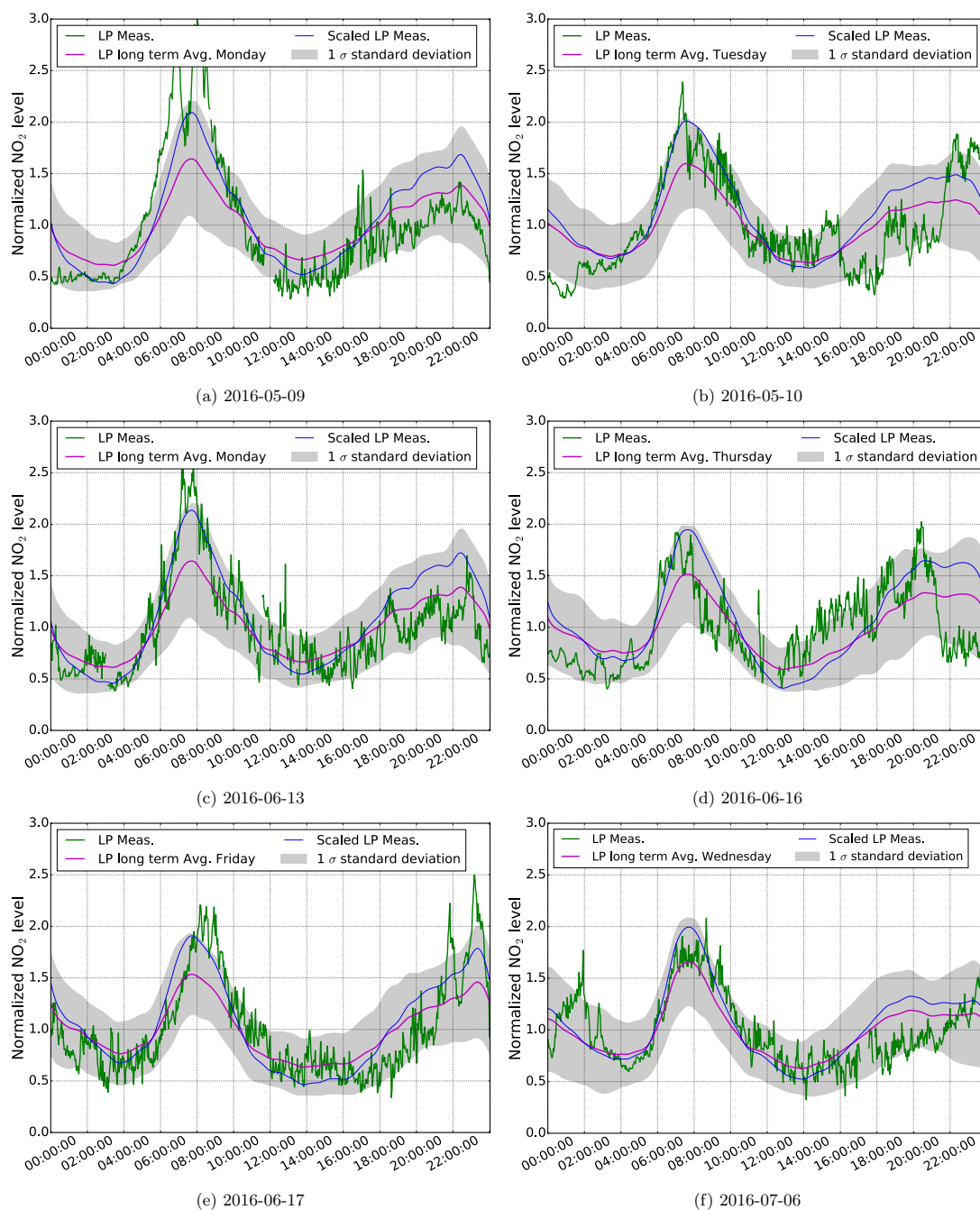
Figure 4.2: Normalized diurnal cycle of NO₂ from Monday to Friday (from (a) to (e)) in Munich in 2016 measured by the LP DOAS. The green curve represents LP DOAS measurement while purple line is the 2.5 years averaged diurnal pattern. The blue line shows the fitted scaled diurnal pattern of ambient NO₂ on each day of the week.

showed significant decrease (>1 ppbv) mainly at the city center. Enhancement of NO₂

concentrations after normalization for certain areas was due to the fact that the mobile measurement took place during non-peak hours during the day, while reduction of NO$_2$ concentrations was due to the measurement vehicle overpassing the regions during rush hours of the day. Compared to the unnormalized data, there were 17.4 % of normalized on-road measurements exceeded the WHO 1-hour guideline and about 14.3 % of the total area in the city center exceeded the guideline. The elevated NO$_2$ level in Munich was presumably due to the fact that the measurement campaigns were conducted during daytime that avoided the rush hours for busy streets in case of traffic jam when the NO$_2$ level was in general lower in comparison to the day-average. In addition, the NO$_2$ in the city park (English Garden) in the city center is about 6 ppbv and therefore much lower than the exterior of the park as plants could reduce the air temperature and provide deposition areas for O$_3$, NO$_x$ and particles (Wesely and Hicks, 2000; Chaparro-Suarez et al., 2011).

4.4.2 Car MAX DOAS Measurements of NO$_2$ and compared with the CE DOAS and CAPS measurements and OMI observation

The car MAX DOAS measurements were deployed in July for one week together with CE DOAS mobile measurements on the city-ring road and motorways. The stationary 2-D MAX DOAS was simultaneously operating on the roof to provide the information of the troposphere NO$_2$ profile, in order to be used for converting mobile NO$_2$ VCDs measurements to the ground level. All measurement days had clear sky with the cloud fraction of less than 50 %. The troposphere NO$_2$ profiles with an azimuth angle of 0° were used as converting factors for each day (shown in Figure 4.4).

The NO$_2$ VCDs of mobile Car MAX DOAS measurements shown in Figure 4.5(a) illustrated similar distributed pattern with peak values on motorways and main busy street in the city center, and relative lower values were observed in residential area. However, the converted ground level NO$_2$ mixing ratio (Figure 4.5(b)) was on average around 3.3 ppbv. 95 % of the car-based MAX DOAS measurements were lower than the CE DOAS and CAPS mobile measurements. This large relative difference was proximately due to the NO$_2$ profiles of the on-road mobile measurements had different shapes from the NO$_2$ profiles of stationary MAX DOAS used to convert the VCDs. Another reason could be the underestimation of the conversion factor measured by the stationary MAX DOAS. The MAX DOAS in general reported lower surface NO$_2$ mixing ratio, which could be ascribed to the difference in the observation height. The lowest layer of the MAX DOAS retrieval extended from 30 m to 230 m above the ground level, while the mobile measurements by CE DOAS and CAPS captured the NO$_2$ emission at 1.5 m. As the major sources of NO$_2$ in Munich are traffic emissions (discussed in section 3.3), which are typically emitted at ground level. Therefore, the concentrations of atmospheric NO$_2$ are expected to be much higher close to the ground. As a consequence, the stationary MAX DOAS in general recorded lower surface NO$_2$ mixing ratios than on-road measurements.

We used the same method with the coinciding LP DOAS measurements corrected for the diurnal effect of the car-based MAX DOAS. The normalized spatial distribution of converted on-road NO$_2$ mixing ratio is shown in Figure 4.6 after applying the normal-

ization. The NO_2 ground levels over 30% of the regions covered with the measurement campaign was significant elevated (>1 ppbv) at the city center and the residential area such as in Moosach , while 51.2% mainly highways showed significant decrease (>1 ppbv). The normalized car-based MAX DOAS measurements indicated the highest polluted area was located in the city center. The NO_2 level on highways was not similarly pronounced, which was different from the normalized NO_2 distribution measured by CE DOAS and CAPS. The different observation heights contributed to the main discrepancy. The car-based MAX DOAS measurements may also be affected by the wind direction since the converted NO_2 mixing ratio measures the average NO_2 up to 200m height, whereas the pollution on highways were mainly from traffic which was close to the ground. To summarize, the Munich city circle is the most polluted area and anthropogenic emission is the domain source of NO_2. A similar distribution can be observed from space by the OMI satellite. Tropospheric NO_2 VCDs averaged for June and July are shown in Figure 4.7. All data were gridded with a $0.02° \times 0.02°$ resolution. It shows a gradually declining from the center towards the Outer Ring of Munich with a total decrease rate of $\sim30\%$.
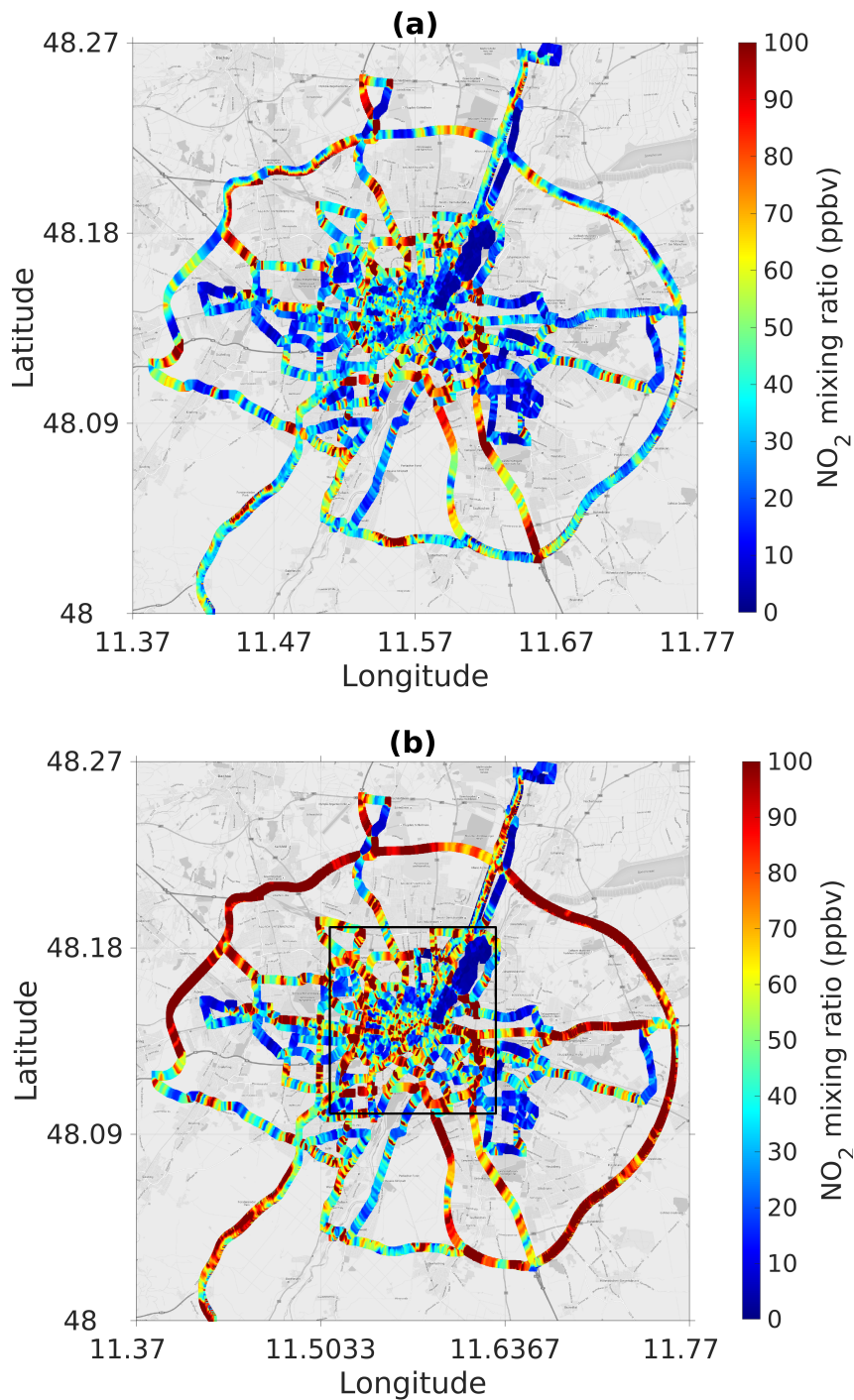
Figure 4.3: (a) CE DOAS and CAPS mobile measurements of NO₂ in 2016. (b) Normalized spatial distribution of NO₂ over city center of Munich measured by the mobile CE DOAS and CAPS in 2016. The CE DOAS and CAPS data is normalized by coinciding normalized LP DOAS data. The black box indicates the area of city center.
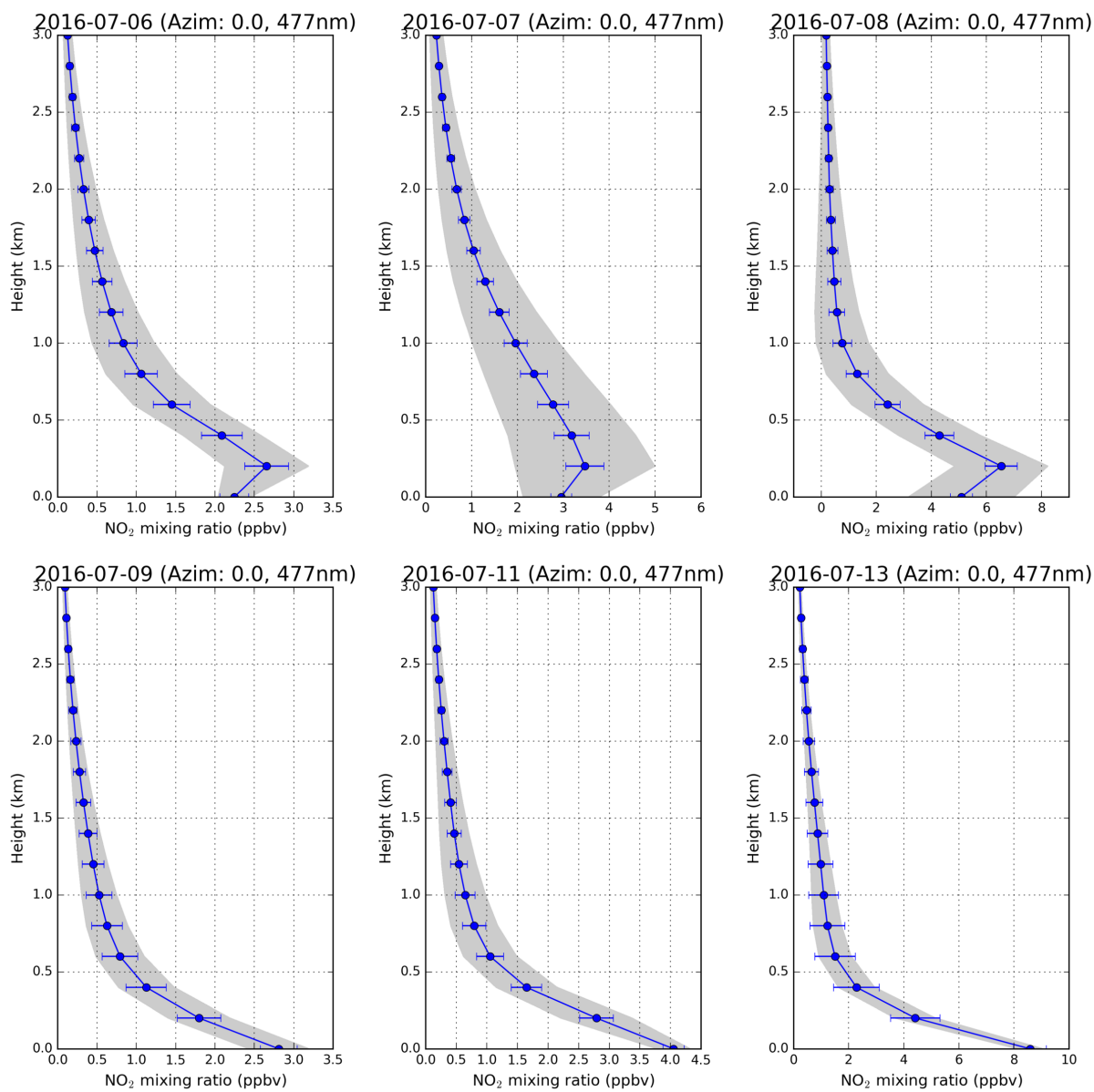
Figure 4.4: NO₂ profile at the azimuth angle of 0° measured by 2-D MAX DOAS on the coincident day of the measurement campaign. The gray regions indicate 1 σ variability of daily data
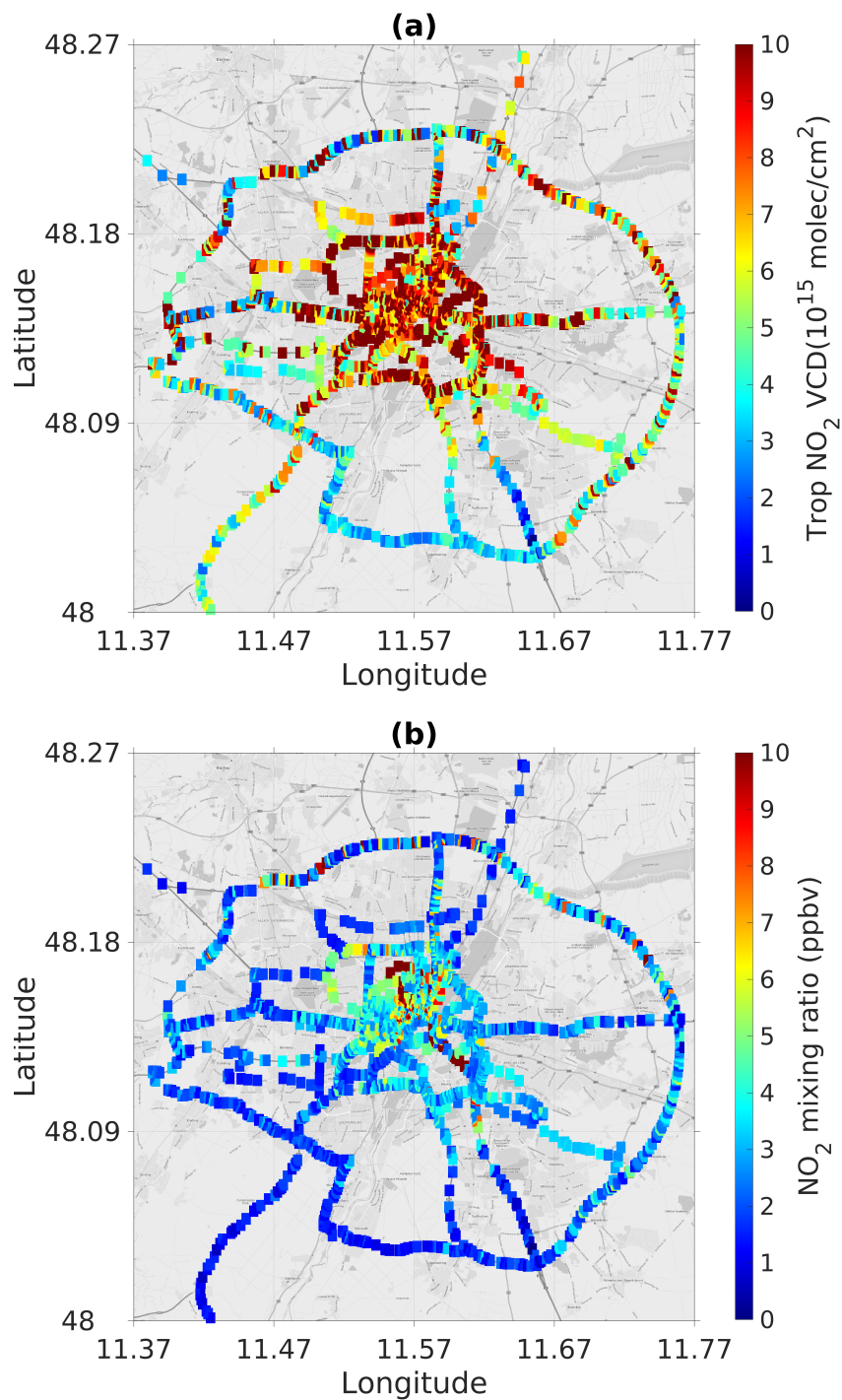
Figure 4.5: (a) Car MAX DOAS measurements of NO₂ VCD. (b) Car MAX DOAS measurements of the NO₂ ground mixing ratio retrieved by coincident NO₂ profile measured by the 2-D MAX DOAS.
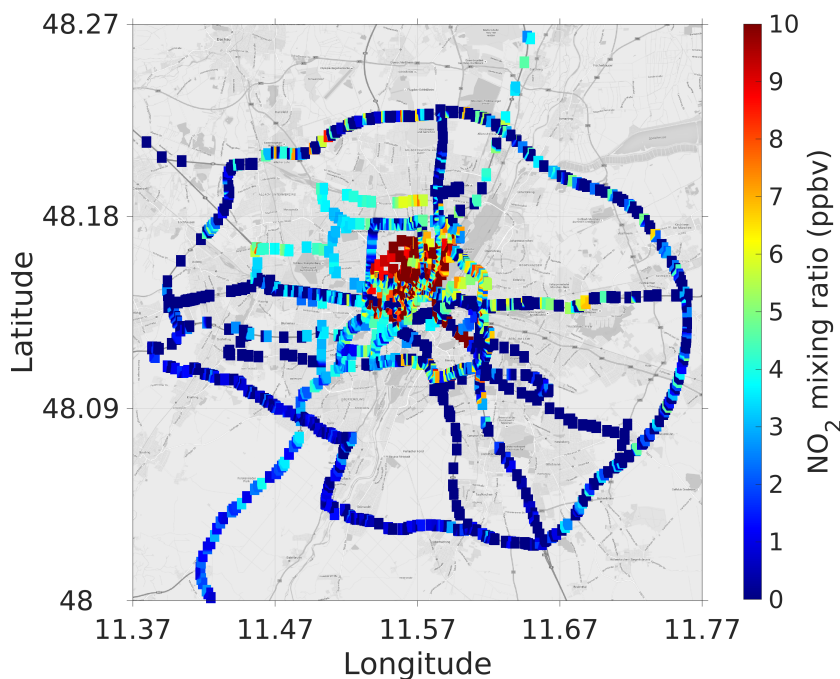
Figure 4.6: Normalized spatial distribution of the NO₂ profile measured by the Car MAX DOAS. The Car MAX DOAS data is normalized by coinciding normalized LP DOAS data.
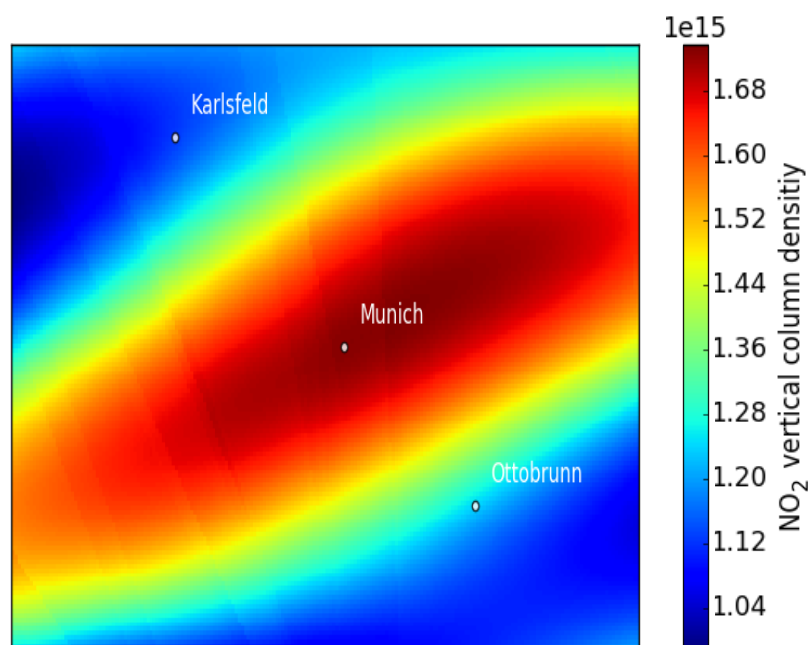
Figure 4.7: OMI observation of the averaged NO₂ VCD of June and July 2016, Munich.

5 Analysis of spatial and temporal patterns of on-road NO$_2$ concentrations in Hong Kong

This chapter will briefly introduce the instrumental setup of LP DOAS and CE DOAS, and mainly talk about the measurement campaign in Hong Kong which has been published on the journal of Atmospheric Measurement Techniques Discussion (AMTD) (Zhu et al., 2018).

5.1 Methodology

5.1.1 LP DOAS NO$_2$ measurement in Hong Kong

A LED based LP DOAS system was installed on the roof-top of the City University of Hong Kong building, providing measurement of near surface NO$_2$. The retro reflectors were placed on a high rise building located at the center of Kowloon, realizing an optical path of 1.9 km (total absorption path of 3.8 km). The spectral range of the spectrometer was adjusted from 400 nm to 462 nm with a spectral resolution of 0.4 nm (FWHM). The average altitude of the LP DOAS light path is ∼50 m above ground level covering a long light path over the urban area of Hong Kong, providing representative measurements of ambient NO$_2$ level. Details of the experimental setup and the data retrieval procedure of the LP DOAS can be found in Chan et al. (2012). When focusing on the spatial variations, we used ambient NO$_2$ values measured by the LP DOAS to normalize for the temporal dependency of the mobile CE DOAS measurements. Since the mobile measurements sample the different parts of the city at different times of the day, the diurnal variability has to be normalized in order to produce a concentration map that represents daily average concentration of NO$_2$. Details of the normalization procedure are presented in section 5.3.

5.1.2 Mobile CE DOAS NO$_2$ measurements in Hong Kong

A CE DOAS instrument was employed for mobile measurements using a sampling inlet positioned on top of the front part of the vehicle at a height of about 1.5 m above ground. The measurements were performed in December 2010 and March 2017 and divided into two parts, (a) measurement along a standard route that covers large part of the urban area in Hong Kong and (b) single measurement in different areas that are not covered by the route. The regular route covers Mong Kok, Central and Causeway Bay which are the busiest areas in Hong Kong (see Figure 5.1). The standard route measurements were

performed 2 to 3 times per day in order to cover non-rush hours, morning and evening rush hours. The varying route measurements were mostly performed during non-rush hours which aims to provide better spatial coverage and to identify pollution hotspots. Measurements performed in 2010 focus more on the on-road NO_2 spatial distribution and the identification of pollution hotspots. Therefore, the 2010 measurements include more non-standard route measurements to have a better spatial coverage. On the other hand, the objectives of the 2017 measurements are refined to investigate the spatio-temporal variations over major pollution hotspots, that are mostly concentrated in the city center. As a result, we focused more on the standard route measurements over the city center in 2017.

(a) (b)
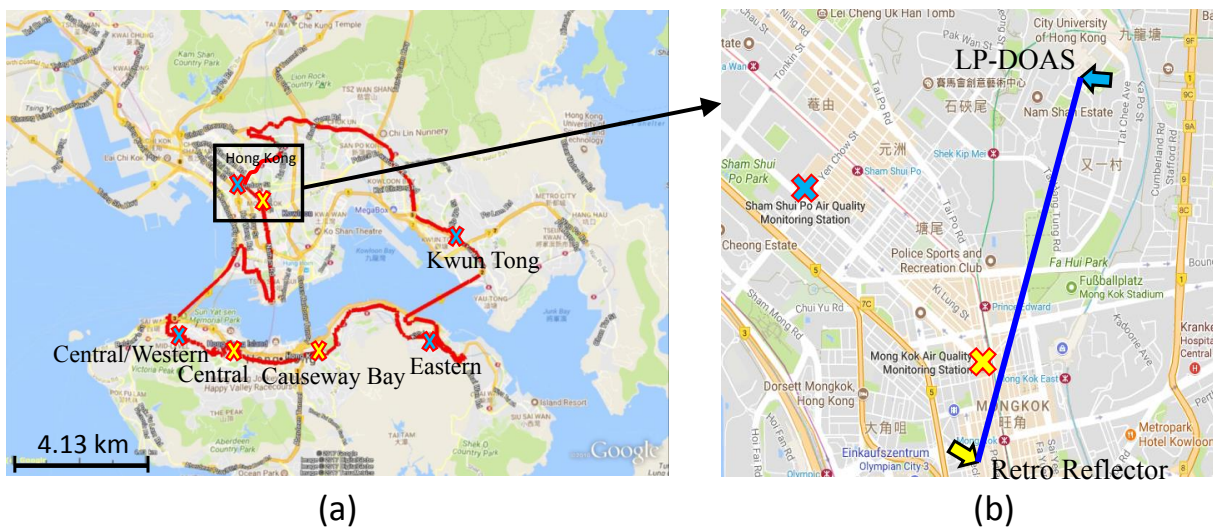
Figure 5.1: Map of Hong Kong city center. (a) The standard measurement route. Yellow crosses indicate 3 roadside EPD monitoring stations while blue crosses represent 4 ambient EPD monitoring stations. The blue line indicated in (b) represents the optical path of the LP DOAS.

A sketch of the CE DOAS instrument in Hong Kong is as same as the instrument in Munich which is shown in Figure 2.5 and described in 2.2.2.1.

5.1.3 Local air quality monitoring network

Ambient NO_2 data in Hong Kong were acquired from the air quality monitoring network of Hong Kong which is operated by the Environmental Protection Department (EPD). The air quality monitoring network comprises 13 ambient and 3 roadside monitor stations (see Figure 5.1 for the locations of some of the stations). They cover both urban and rural areas in Hong Kong. The NO_2 and NO_x concentrations are measured by in-situ chemiluminescence NO_x analyzer. UV absorption O_3 analyzer is used for O_3 monitoring. More details of the air quality monitoring network can be found on http://www.aqhi.gov.hk/en/monitoring-network/air-quality-monitoring-network.html. Hourly

NO$_2$ concentrations from seven of the air quality monitoring stations were used to compare to LP DOAS and CE DOAS NO$_2$ measurements. In addition, NO$_2$, NO$_x$ and O$_3$ data from the monitoring stations are used for long-term trend analysis.

5.1.4 Estimate NO using additional measurements of O$_3$

During the mobile measurements, ozone concentration was recorded by an UV light-based Dual Beam Ozone Monitor (Model 205, 2B Technologies) in 2017 measurement campaign. NO concentration can be derived from measured coinciding NO$_2$ and O$_3$ measurements by using the Leighton ratio equation assuming the NO/NO$_2$/O$_3$ photo-stationary state is steady. This approach has been widely used in the research of NO/NO$_2$/O$_3$ reactions(Stevens, 1987; Atkinson et al., 1997; Düring et al., 2011). Photolysis rates (J) of NO$_2$ under different meteorological conditions (various cloud optical depths (COD) under moderate aerosol pollution) were calculated in the report of VDI-Richtlinie(VDI, 2017a). According to the meteorological condition during our measurement campaign in March 2017, the NO$_2$ photolysis rates we applied are 2.5 (10^{-3}s^{-1}) and 0.5 (10^{-3}s^{-1}) with overcast of COD $= 20$ of Hong Kong calculated by Kim et al. (2014) study and solar zenith angle of 50° and 70° respectively. The averaged NO$_2$/NO$_x$ ratio is about 0.70 $\pm$ 0.22 during the on-road measurements. The reaction time of NO-NO$_2$-O$_3$ chemistry in an inner city street canyon with high traffic density is about 12.6 seconds, that simulated by regional atmospheric chemistry modeling (RACM) (VDI, 2017b). Since emissions accumulate for much longer than that, we can assume equilibrium state with an averaged NO$_2$/NO$_x$ ratio of 0.70 $\pm$ 0.22 for our measurements that calculated by using the Leighton ratio equation referring to the report of VDI-Richtlinie(VDI, 2017a). This value could be confirmed by ratios derived from the EPD monitoring stations where NO measurement were available (see section 5.4).

An electrical chemical sensor package (A-type including NO, NO$_2$, O$_3$) from Alphasense Co. ltd. were also applied in our mobile measurements. It was a prototype of the new generation portable air quality monitor mini station of our future measurements. More calibration process need to be done. The preliminary result of averaged on-road NO$_2$/NO$_x$ ratio were agree with roadside EPD measurements.

5.2 NO$_2$ measurement comparison

Our LP DOAS measurements of atmospheric NO$_2$ in Hong Kong started in December 2010. The data shows significant diurnal, weekly and seasonal variability. The daytime annual average NO$_2$ concentration measured by the LP DOAS from 2011 to 2015 is 47.5 μg/m^3. A decreasing trend can be observed (see Figure 5.5 d), but they all still higher than the WHO annual guideline value or Hong Kong air quality objective annual average value at 40 μg/m^3. Additionally, episodes of high NO$_2$ levels are occasionally recorded.

A time series of NO$_2$ concentrations measured by LP DOAS and EPD monitoring stations are shown in Figure 5.2. On one hand, both LP DOAS and EPD measurements show
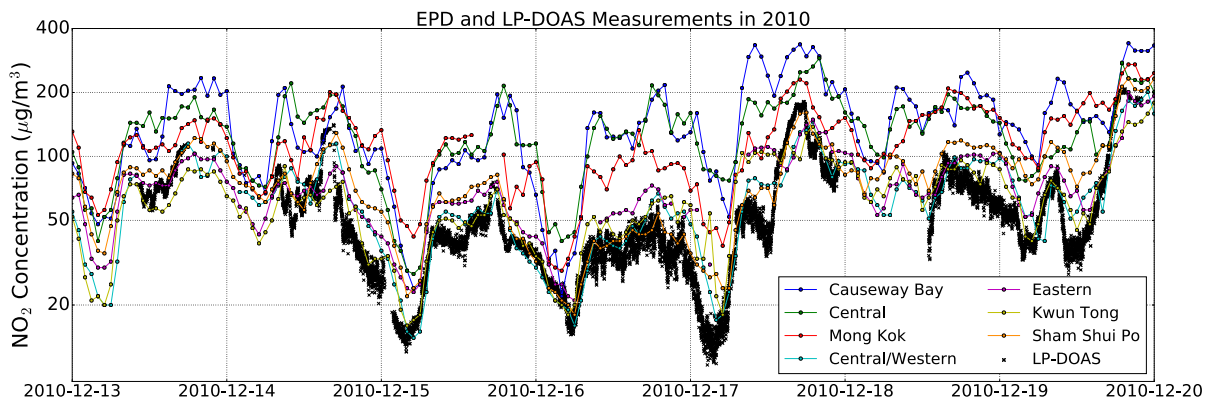
Figure 5.2: Time series of NO$_2$ concentration measured by LP DOAS and EPD Monitoring stations during the measurement campaign in 2010.

similar variation pattern with higher values during daytime and lower values at night. On the other hand, LP DOAS and different EPD stations measurements also demonstrate different characteristics of NO$_2$. The significant spatial dependency of NO$_2$ is also confirmed in long-term changes (see Figure 5.5). All measurements observe elevated NO$_2$ levels during morning (8:00 to 10:00) and afternoon (17:00 to 19:00) rush hours. However, the absolute concentration measured by different stations varies in a wide range. In addition, differences in measurement height also contribute to differences among these measurements. In order to have a better overview of the NO$_2$ spatial distribution, temporal variation and their emission source pattern, we performed mobile measurements of on-road NO$_2$ using a CE DOAS instrument. On road measurement can easily be influenced by the traffic condition, e.g., accumulation of emission during traffic congestion, and the diurnal variation of ambient NO$_2$. In order to correct for these effects in the mobile measurement, we have filtered data which is influenced by traffic condition and normalized the on-road measurement for diurnal variation of NO$_2$.

5.3 Data filtering and normalization

5.3.1 Comparison of concentrations during fluent traffic and traffic congestion

Traffic congestion can result in higher pollution levels due to accumulation of vehicle emissions, cased by less turbulent mixing with cleaner air and longer NO to NO$_2$ reaction time. These high values recorded during low speed driving i.e. in a traffic jam or in front of a traffic light. Figure 5.3 shows the time series of vehicle speed and measured NO$_2$ concentration during a traffic congestion on 2nd Mar 2017. Note that the vehicle speed is calculated from the GPS data with an error about 0.6 m. Converting the error into vehicle speed would be 1.4 km/h. Therefore, the vehicle speed is never zero even if the vehicle stops. In the example shown in Figure 5.3, the vehicle slowed down and stopped for half a minute at a traffic light. The NO$_2$ level goes up from about 100 μg/m^3 to more than

$400\,\mu g/m^3$. The NO_2 level rises about $8\,s$ after the vehicle stopped. When the vehicle started moving again, the measured NO_2 level gradually dropped back to the pre-stop level within $20\,s$.

In order to separate data influenced by accumulation of NO_2 during all traffic congestion with particular idling time, we filtered data from $8\,s$ after the vehicle speed drop below $5\,km/h$ to $20\,s$ after the vehicle speed goes above $5\,km/h$ again. In order to avoid filtering data due to poor GPS signal, this filter only applies when the vehicle speed is below $5\,km/h$ for more than $8\,s$. The average NO_2 concentrations for standing condition are $239\,\mu g/m^3$ which is $14.5\,\%$ higher on average. We filter out traffic light or traffic jam stops only to have a consistent NO_2 spatial distribution under fluent driving condition for the direct comparison of two measurements in different days and years, in order to focus on the concentrations instead of the stopping frequency. This filter criterion remove $37\,\%$ and $30\,\%$ of the total number of measurement data in 2010 and 2017. However, since the filter mainly removes measurements at low speed or standing, only $10\,\%$ and $11\,\%$ of the spatial points were removed for 2010 and 2017, respectively.
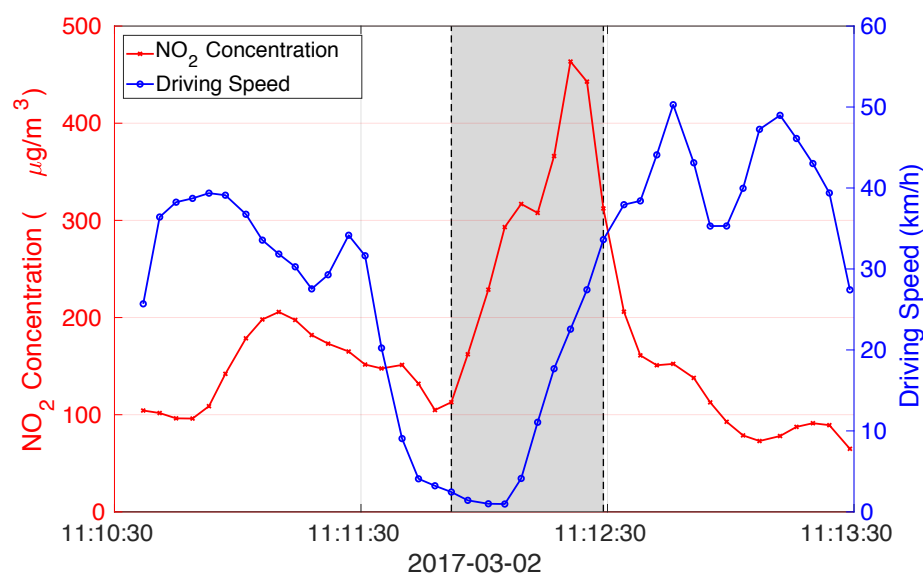
Figure 5.3: Time series of the driving speed and the coinciding NO_2 concentration during stops due to traffic congestion. Data in gray area will be filtered out in later analysis.

5.3.2 Normalization of the diurnal cycle

In order to separate the NO_2 spatial and temporal variability and show a representative spatial distribution of NO_2 in Hong Kong, we developed an algorithm using LP DOAS measurements to normalize for the diurnal variations. Although the LP DOAS measurement covers a long light path over the urban area in Hong Kong, the NO_2 values provided

might still not be representative for all measurement areas due to local influences. Therefore, we use a normalized long term average of diurnal NO_2 cycle for each weekday to correct for the temporal variation effect. It is less depending on outliers caused by the overpass pollution plume and can also interpolate data gaps due to instrumental problems and bad weather.

LP DOAS measurements of atmospheric NO_2 for each day are first normalized by dividing by the daily mean NO_2 concentration. The resulting normalized NO_2 level are then averaged for each day of the week over a period of 2 years to obtain a representative diurnal NO_2 variation pattern. The normalized and averaged diurnal NO_2 variation pattern of the corresponding weekday is scaled and shifted to fit the normalized LP DOAS measurement for each day during the mobile measurement campaign. The inverse of the $1\,\sigma$ (standard deviation) variation of the 2-year averaged and normalized NO_2 level is used as weighting in the least squares regression to scale and shift the long term average diurnal pattern. In order to avoid single high value affecting the whole regression, normalized NO_2 level exceeded the $1\,\sigma$ variation of the 2-year averaged and normalized NO_2 level were not considered in the regression process. Figure 5.4 shows the normalized NO_2 concentration measured by the LP DOAS on 17th Dec 2010. Normalized 2-year Friday mean NO_2 diurnal pattern, the diurnal pattern of scaled NO_2 measurement taken on 17th Dec 2010 and normalized EPD monitoring data are shown as well. All data illustrate similar characteristics with significant peaks in the morning (8:00 to 10:00) and evening (17:00 to 19:00) rush hours. The fitted long term diurnal pattern is then used to correct for the diurnal effect of the mobile measurement. Mobile measurements are multiplied by the simultaneous NO_2 level of the resulting normalized LP DOAS diurnal pattern to obtain a more representative value for the measurement areas.

5.4 Long-term trends of NO_2

On road CE DOAS measurements are analyzed together with LP DOAS and EPD monitors data to investigate the long term trend of on-road and ambient NO_2. The observed trends at the different locations is compared to the changes of the mobile on-road CE DOAS NO_2 measurements in 2010 and 2017 taken within $100\,m$ radius of the 3 EPD roadside stations or along the LP DOAS measurement path within $1\,km$ (Figure 5.5a, b, c, d). The time series represent monthly averaged ambient NO_2 concentrations measured during daytime. OMI satellite observations of monthly average tropospheric NO_2 VCDs over Hong Kong are shown in Figure 5.5e. The data are filtered for cloud fraction larger than $50\,\%$ and the radius of average is $50\,km$. On-road, ambient, and satellite measurements of NO_2 all show a decreasing trend. Ambient NO_2 levels measured by the LP DOAS show a descending trend with a rate of $2.5\,\%$ per year. Stronger decreasing trends of roadside NO_2 are observed by EPD in Mong Kok, Causeway Bay and Central roadside station with annual decreasing rates of $4.4\,\%$, $3.3\,\%$ and $4.8\,\%$, respectively. A similar reduction rate is also observed by on-road CE DOAS measurements. Comparing the CE DOAS measurement taken in 2010 and 2017, on-road NO_2 levels are overall reduced $28\,\%$ for areas along the standard measurement route which would correspond to an annual
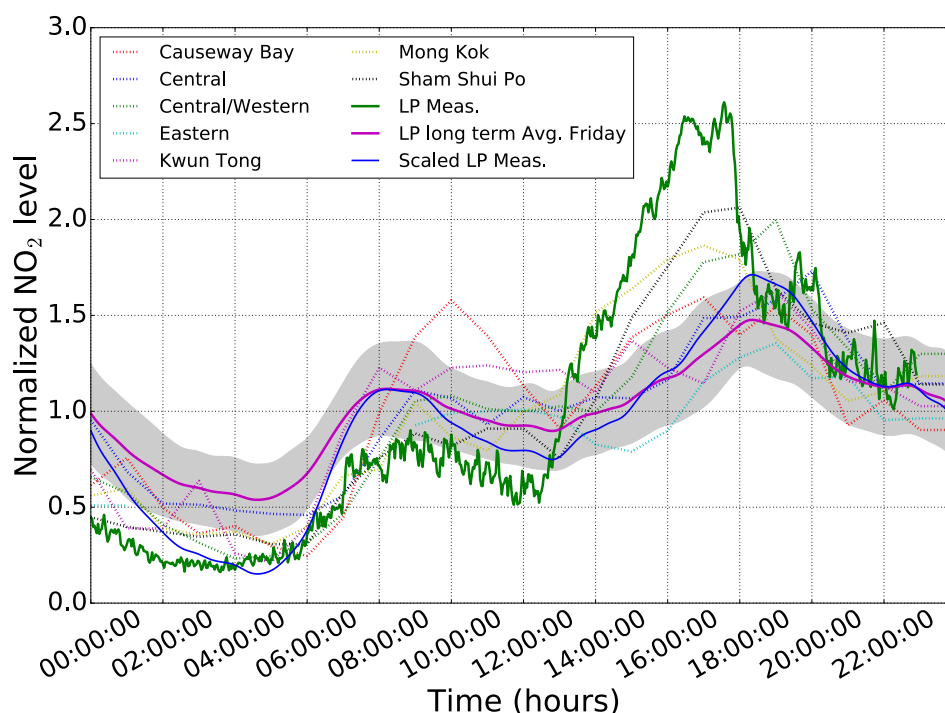
Figure 5.4: Normalized diurnal cycle of NO$_2$ on Friday in Hong Kong in 2010 measured by the LP DOAS and EPD monitoring stations. EPD measurements on 17th Dec 2010 from 7 monitoring stations are indicated as dashed line. The green curve represents LP DOAS measurement while purple line is the 2 years averaged diurnal pattern with shadowed area of the 1 σ standard deviation variation. The blue line shows the scaled and shifted diurnal pattern of ambient NO$_2$ on Friday, 17th Dec 2010.

decreasing rate of 4.0 %. NO$_2$ levels in 85% of the measurement area are significant reduced (>1 ppbv) by 37 % on average, whereas NO$_2$ levels in 14 % of the area are elevated (>1 ppbv) by 22 % on average. The reduction rate for on-road NO$_2$ levels varies from 45 % to 67 %. This reduction change can also be observed from space by satellite OMI. Tropospheric NO$_2$ VCDs show a descending trend with a rate of 3.7 % per year. In addition, Figure 5.6a and b show tropospheric NO$_2$ VCDs over the Pearl River Delta from 1st of Nov 2010 to 31st Jan 2011 and from 1st Feb 2017 to 31st Apr 2017, respectively. The absolute and percentage differences of tropospheric NO$_2$ VCDs between the two periods are shown in Figure 5.6 c and d, respectively. In general, tropospheric NO$_2$ VCDs are reduced by $\sim$50 % (7 % per year) over Hong Kong, while the reduction over Pearl River Delta is ranging from 30 - 60 %.

Averaged on-road NO$_2$ concentrations measured along the standard route during December 2010 and March 2017 are shown in Figure 5.7a and b, the differences in Figure 5.7c. The measurement routes are slightly different due to road constructions and maintenance. In general, a significant reduction (ranging from 20% to 50%, and 4 % / year on average) of on-road NO$_2$ can be observed which is consistent with the LP DOAS and EPD mon-

itor data. The reduction of on-road NO$_2$ level along Nathan Road, the busiest road in Kowloon, is ranging from 50 % to 60 % (around 7 % to 8 % /year). On the other hand, an enhancement of NO$_2$ level can be observed around subway stations, e.g., Hong Kong University station, Kwun Tong station, Diamond Hill station, Ngau Tau Kok station, etc. It probably reflects the fact that there are more bus terminals or bus stops surrounding metro stations in 2017 compared to 2010. Data from the transport department shows that the total number of licensed franchised bus has slightly increased by 3 % from 5729 in 2010 to 5916 in 2016 (http://www.td.gov.hk/en/transport_in_hong_kong/ transport_figures/monthly_traffic_and_transport_digest/index.html). Although the number of franchised bus only has a small contribution to the total number of vehicle in Hong Kong (608 thousands in 2010, 746 thousands in 2016), franchised buses can account for up to 40 % of the traffic at busy traffic corridors (http://www.info.gov. hk/gia/general/201512/31/P201512310204.htm). Average daily public transport usage also increased from 11.6 millions time per day in 2010 to 12.6 millions time per day in 2016. According to the annual reports of Transport International Holdings Limited, the parent company of the Kowloon Motor Bus Company, the largest franchised bus operator in Hong Kong, the total number of buses increases slightly from 3988 in 2010 to 4162 in 2016. However, the number of bus routes reduced from 393 in 2010 to 384 in 2016. These changes are mainly due to the reformation of the operational strategies of the franchised bus operators. Due to the expansion of the metro system in Hong Kong, the role of bus has gradually changed from point to point long distance services to a connector between destination and metro stations. Therefore, enhancement of NO$_2$ levels is observed around metro stations. Franchised bus operators in Hong Kong started to introduce higher emission standard buses (Euro IV and V) since 2009. Buses with model earlier than Euro III which is proven to be more polluted (Dallmann et al., 2011; Mock, 2014; Lau et al., 2015; Pastorello and Melios, 2016). Therefore, the companies started to install retro fit catalytic convertor on earlier model buses and these buses will be replaced completely by buses with higher emission standard by 2021. In addition, the government has set up franchised bus Low Emission Zones (LEZs) in three busiest traffic corridors in Hong Kong on 31st Dec 2015. Buses with emission standard below Euro IV are not allow to operate within these low emission zones. Therefore, both ambient and roadside NO$_2$ levels show a descending trend. In addition, navigation (water transport), road transport and public electricity generation are the largest sources of NO$_x$ according to the 2015 Hong Kong Emission Inventory Report and data from the EPD Hong Kong Air Pollutant Emission Inventory, accounting for 33%, 30% and 25% of total NO$_x$ emissions in 2010 and 37%, 18% and 28% in 2016, respectively. NO$_x$ emissions from navigation and public electricity generation are rather constant, while emissions from road transport show a significant reduction of ∼50 % from 32.1 tonnes in 2010 down to 16.2 tonnes in 2015. This is coherent with the decreasing trend of NO$_2$ from 2010 to 2017.

We have looked into the NO$_2$/NO$_x$ ratio as well as the O$_3$ concentration in order to better understand the impacts of reduction of vehicular emission of NO$_x$. An increasing trend of NO$_2$/NO$_x$ ratio is observed from both roadside and ambient monitoring stations. Figure 5.8 shows the NO$_2$/NO$_x$ ratio for (a) roadside and (b) ambient stations. Ozone concentrations from both (c) roadside and (d) ambient stations are shown for reference.

Decreasing roadside NO_2 level with increasing NO_2/NO_x ratio implies a significant reduction of primary NO emissions. The reduction of primary NO is could be subjected to the upgraded catalytic converter of diesel vehicles (from Euro III or earlier model to Euro IV and V) which reduces the total NO_x emission and increases the NO_2/NO_x ratio (Kašpar et al., 2003). Newer diesel engines in general reduce the total NO_x emission by $\sim$50 % according to the European emission standards for diesel passenger cars (EU emission standards, 2007). The Euro III diesel engines emission limit of NO_x is 0.50 g/km, whereas the Euro IV emissions limit has reduced half to 0.25 g/km. However, this standard might not fully reflect the real driving condition (Franco et al., 2014) and it should be confirmed by more realistic mobile measurements. Furthermore, Tian et al. (2011) observed a rising roadside NO_2/NO_x ratio as well coincided with the introduction of new environmental friendly pre-Euro light and heavy duty vehicles in 2000 and 2003. Ning et al. (2012) also suggested that the proposal of replacing Euro II and III franchised buses to meet Euro IV or even higher emission standards will result in an increase of roadside NO_2/NO_x ratio. In addition, a general rising trend of ambient and roadside ozone is also observed from the EPD monitoring data. Increasing O_3 level also contribute to increasing the atmospheric NO_2/NO_x ratio. The portion of pollutants contributed by road transport emissions (typically with lower NO_2/NO_x ratio) was reduced.

5.5 Weekend effect

Figure 5.9a shows the five years average diurnal cycle of NO_2 of each day of the week measured by LP DOAS, and the seven years average NO_2 diurnal pattern measured by EPD Sham Shui Po, Mong Kok and Causeway Bay station are shown in Figure 5.9b, c and d, respectively. The diurnal pattern of NO_2 illustrates different characteristics between weekdays and weekend. Different measurement locations also show different characteristics of NO_2 during weekend. The LP DOAS measurement indicates the NO_2 concentration is on average 3.3 % lower on Saturday and 8.7 % lower on Sunday compared to weekdays. However, the morning rush hour (8:00 to 10:00) peak of NO_2 is significantly reduced by 23.1 % on Sunday, while the evening rush hour (18:00 to 20:00) peak shows a less pronounced reduction of 9.7 %. NO_2 measurements from the Sham Shui Po ambient station and the LP DOAS show similar diurnal variation pattern and weekend reduction. The weekend reduction is less pronounced for the roadside measurements in Mong Kok, the NO_2 level is on average 3.8 % lower on Sunday compared to weekdays, with reduction during the morning and evening rush hours of 13.1 % and 7.3 %, respectively. Similar weekend reductions are also observed by other EPD roadside stations, i.e., Causeway Bay and Central. These differences in the diurnal cycle are most likely due to different types of land use. Traffic emissions are the main source of NO_2 in urban areas which is strongly dependent on human activities. In residential areas, traffic is reduced during weekend as most of the residents do not work on Sunday, e.g., frequency of buses is reduced during weekend. However, the traffic load is mostly unchanged in commercial areas, since shops are open as well on Sunday.

In order to further investigate the relationship between residents' activities during week-

days and weekend and NO$_2$ emissions, we have looked into the morning standard route measurements on a sequential Sunday and Monday in 2017. Two sequential days are used for comparison so as to avoid influences from different meteorological conditions. NO$_2$ concentration maps measured on Sunday and Monday are shown in Figure 5.10a and b and its difference in c. The NO$_2$ level on Sunday is on average about 45 % lower than that of Monday. The mobile measurements are in general agreement with coinciding EPD data, while discrepancies can be observed for peak values captured by the more frequently measuring CE DOAS. This discrepancy is mainly due to the difference in measurement time. Mobile measurement recorded the instant concentration of on-road NO$_2$ which could easily be influenced by a single incident, especially the on-road NO$_2$ level varies rapidly. On the other hand, EPD monitors provide hourly averaged NO$_2$ concentration which tend to average out those local pollution peaks. Besides, four EPD ambient monitoring stations are located more than 15 m above ground level. Therefore, EPD ambient stations are expected to measure lower NO$_2$ concentrations compared to on-road CE DOAS measurements. In addition, NO$_2$ concentrations of each location show rapid changes which are highly dependent on the traffic flow. However, a consistent elevated NO$_2$ level is observed over the most busy roads, such as Nathan Road in Kowloon, western and eastern Harbor Cross Harbor tunnels. 85 % of the measurements show significant higher (>1 ppbv) NO$_2$ concentrations, whereas 13 % of the measurements show significant lower (>1 ppbv) NO$_2$ concentrations on Monday compared to Sunday. The spatial pattern of elevated NO$_2$ level on Sunday matches with the location of large shopping malls. Similar difference maps between other workdays and Sunday are observed. The number of licensed private car grows by ~30 % from 415 thousands in 2010 to 536 thousands in 2016, while the public transport usage increases by ~9 % from 11.6 millions time per day in 2010 to 12.6 millions time per days in 2016 (http://www.td.gov.hk/en/transport_in_hong_kong/ transport_figures/monthly_traffic_and_transport_digest/index.html). These numbers imply that there is an significant increase of weekend drivers in Hong Kong. People are taking public transport for daily commute, while go out to shopping with their own car in the weekend. As the parking spaces are limited around these shopping areas and results in traffic congestion around these major shopping malls during weekend. As a consequence, an enhancement of NO$_2$ level can be observed over these locations. This is an interesting example of how people's daily life influences the pollution patterns.

5.6 Spatial distribution of NO$_2$ in Hong Kong

In order to have a better overview of major pollution hotspots in Hong Kong, all measurements taken in 2010 were spatially averaged to a high resolution grid of 20 m × 20 m (Figure 5.11 (a)). These measurements covered most of the major roads in Hong Kong, including highway, urban, sub-urban and rural area. As the spatial coverage of measurements taken in 2010 and 2017 is quite different and there is a general decreasing trend of NO$_2$, we only use data measured in 2010 for the spatial distribution analysis to avoid any bias toward lower value over the city center. Elevated NO$_2$ levels are mainly distributed over motorways and busy roads that always with high traffic intensity in the city center,

e.g. No. 8 and No. 9 motorway, Nathan Road in Kowloon, Queen's Road in Central, and Hennessy Road from Admiralty to Causeway Bay. About 29 % of the on-road measurements exceeded the WHO one hour guideline value of 200 μg/m^3, while 27 % of the data measured in the city center exceed the guideline. High NO$_2$ values over motorways are probably due to having more heavy-duty vehicles. On the other hand, traffic congestion and street canyon effects (Rakowska et al., 2014) are the major cause of elevated on-road NO$_2$ in the city center.

As described in section 5.3.2, on-road pollutants mainly produced by vehicles and the traffic flow patterns also have a large impact on pollutant distributions (Westerdahl et al., 2005; Kaur et al., 2007; Huan and Kebin, 2012; Rakowska et al., 2014; Fu et al., 2017). The diurnal dependency of the measurement times is corrected for using the simultaneous normalized LP DOAS measurement. The normalized spatial distribution of on-road NO$_2$ is shown in Figure 5.11(b). This normalized dataset is now representative for the daily average. NO$_2$ levels over some regions are significantly enhanced after applying the normalization, particularly, the residential area in Yuen Long district and Tung Chung district, where the Hong Kong International airport is located. Some other areas (mainly at the city center and highways) obtained lower NO$_2$ values after normalization. Enhancement of NO$_2$ concentrations after normalization for certain areas is due to the fact that the mobile measurement took place during non-peak hours during the day, while reduction of NO$_2$ concentrations is due to the measurement vehicle overpassing the regions during rush hours of the day. Compared to unnormalized data, only 27 % of normalized on-road measurements exceeded the WHO one hour guideline and about 20 % of the area in the city center exceed the guideline. The slightly decreased NO$_2$ level in both all over Hong Kong and city center are presumably due to the fact that the measurement campaigns are conducted during daytime when the NO$_2$ level is in general higher compared to nighttime.
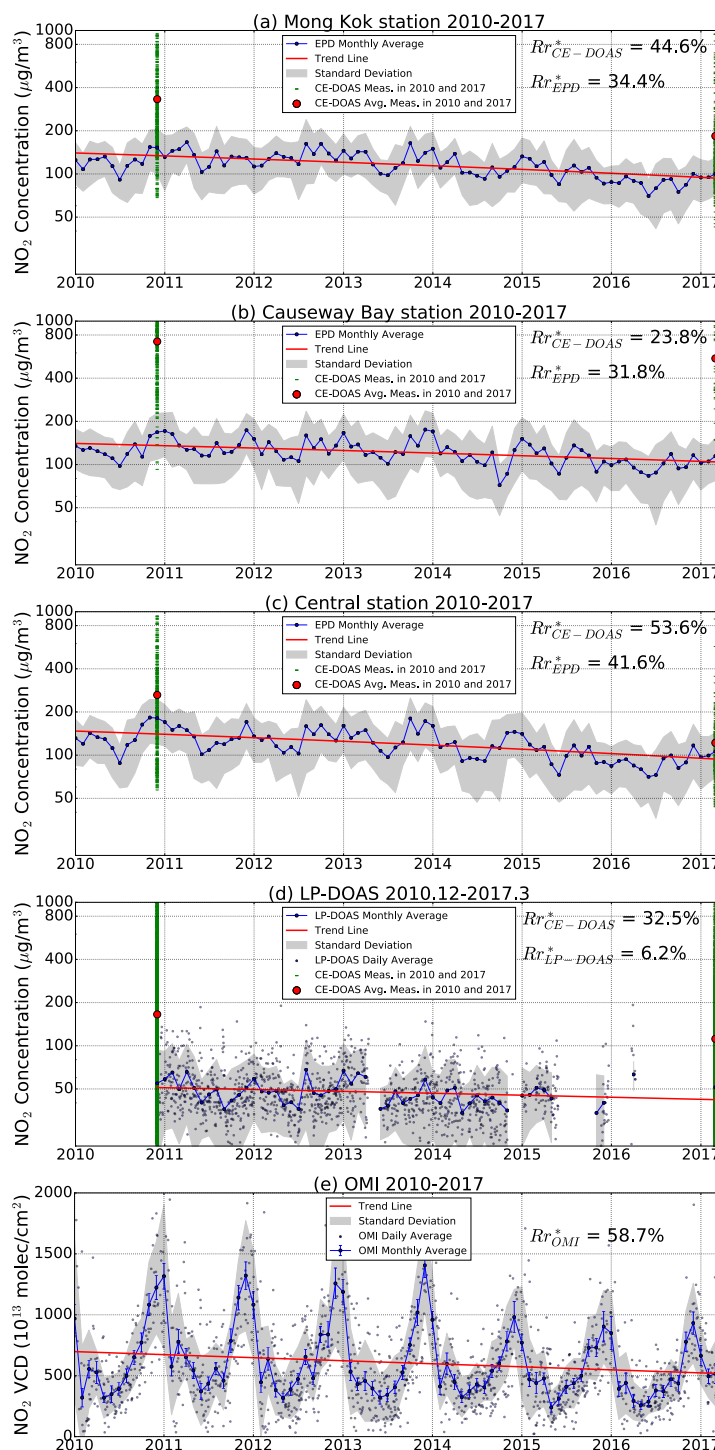
Figure 5.5: Monthly averaged NO₂ concentration during daytime from Jan 2010 to Mar 2017 measured by three EPD stations and LP DOAS. Red dots indicate the NO₂ averaged concentration measured by the CE DOAS within 100 m radius of (a) Mong Kok, (b) Causeway Bay and (c) Central roadside station. (d) shows the CE DOAS measurements within 1 km radius of the center of the LP DOAS measurement path and monthly averaged ambient NO₂ levels during daytime observed by the LP DOAS. (e) shows the Monthly averaged OMI tropospheric NO₂ VCDs over Hong Kong. Reduction rates R_r indicated on the figures are calculated by taking the relative difference between averaged data taken in December 2010 and March 2017.
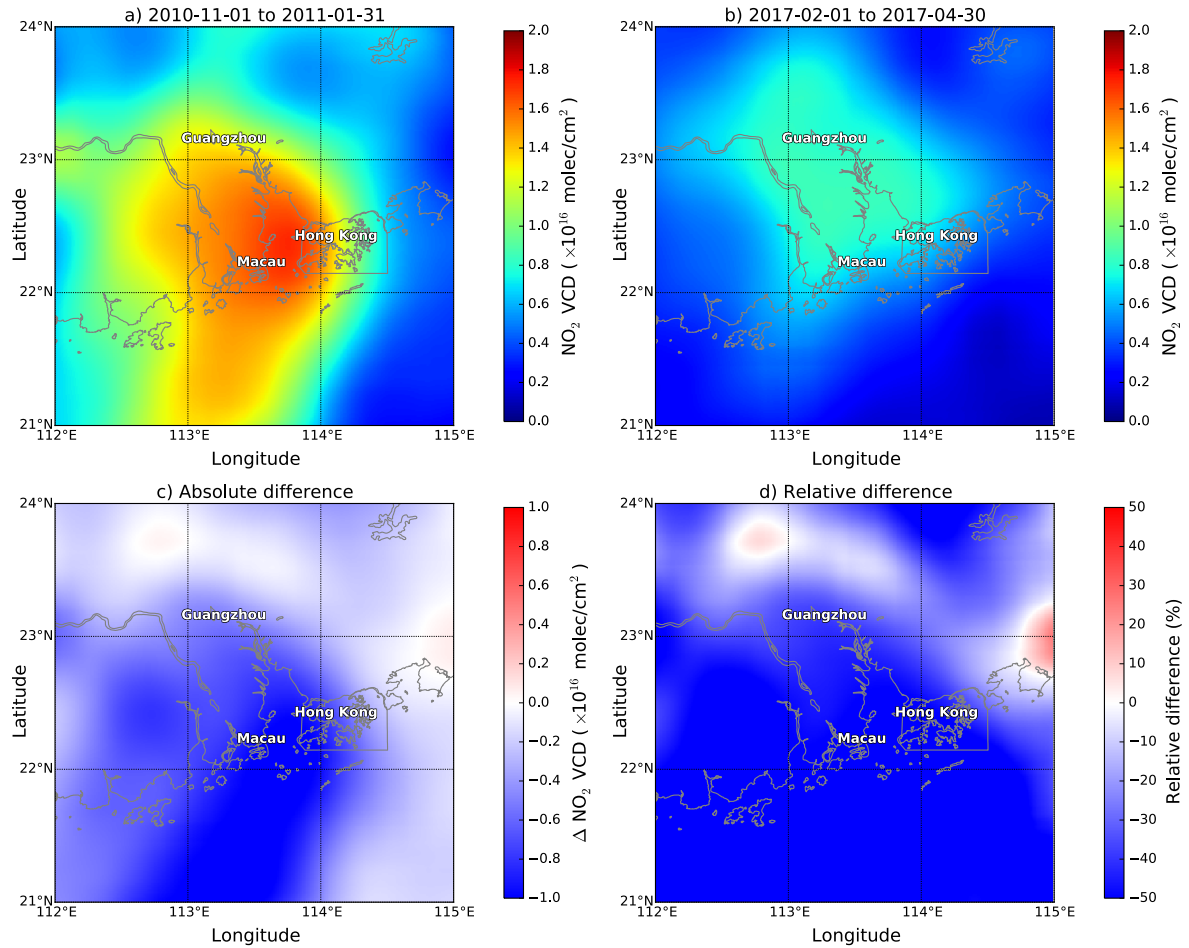
Figure 5.6: Averaged OMI tropospheric NO_2 VCDs over Pearl River Delta a) from 1st of Nov 2010 to 31st Jan 2011 and b) from 1st Feb 2017 to 31st Apr 2017. The absolute and percentage differences of tropospheric NO_2 VCDs between a) and b) is shown in c) and d), respectively. Negative values indicate reduction of NO_2 levels.
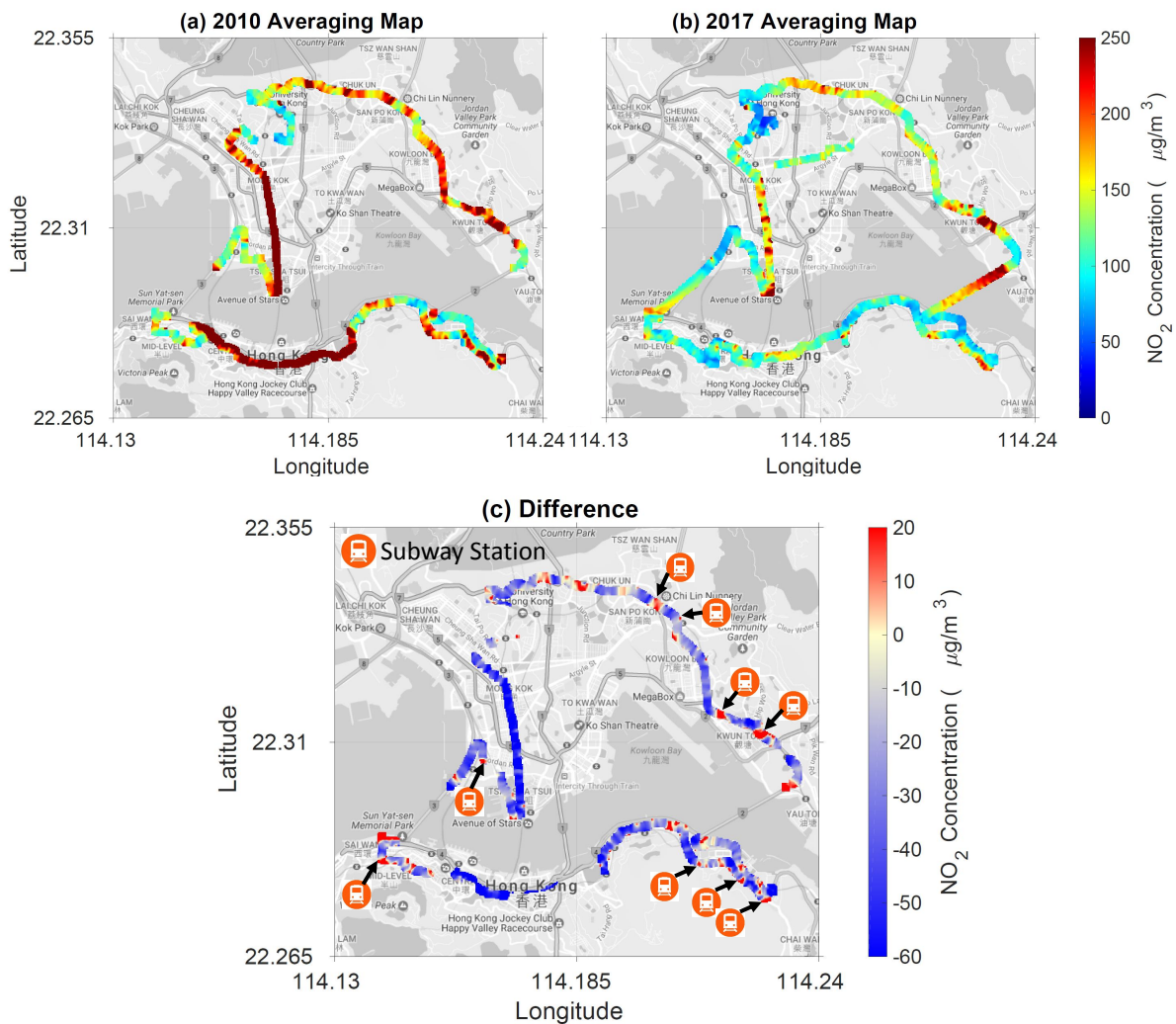
Figure 5.7: Averaged on-road NO_2 concentrations measured along the standard route during (a) December 2010 and (b) March 2017. (c) shows the relative differences between 2010 and 2017. The locations of subway stations are marked.
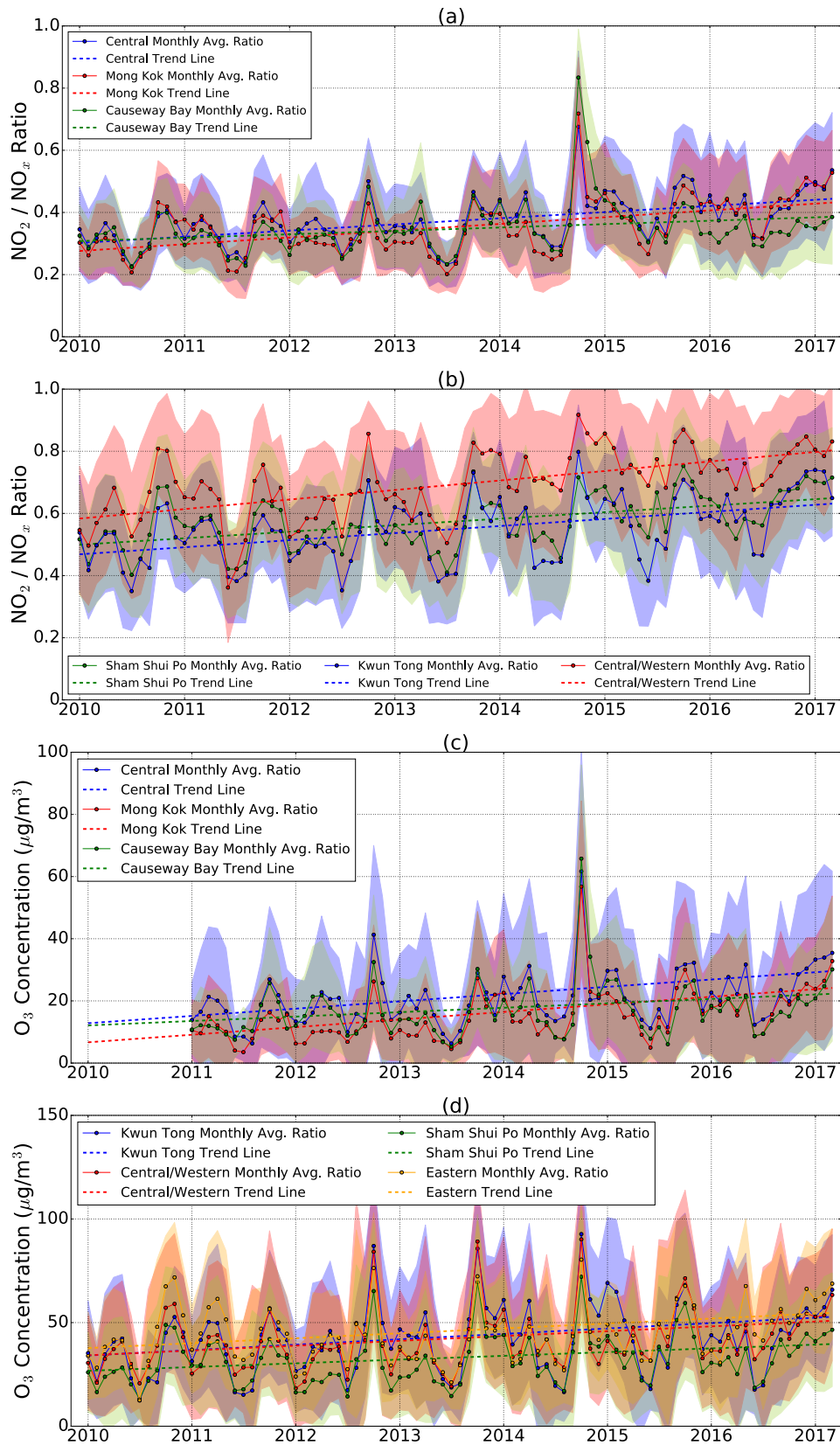
Figure 5.8: Monthly averaged NO$_2$/NO$_x$ ratio from EPD (a) roadside stations (b) ambient stations. O$_3$ concentrations measured by EPD (c) roadside stations (d) ambient stations are shown. Shadowed area indicates the 1 σ standard deviation variation of measurements.
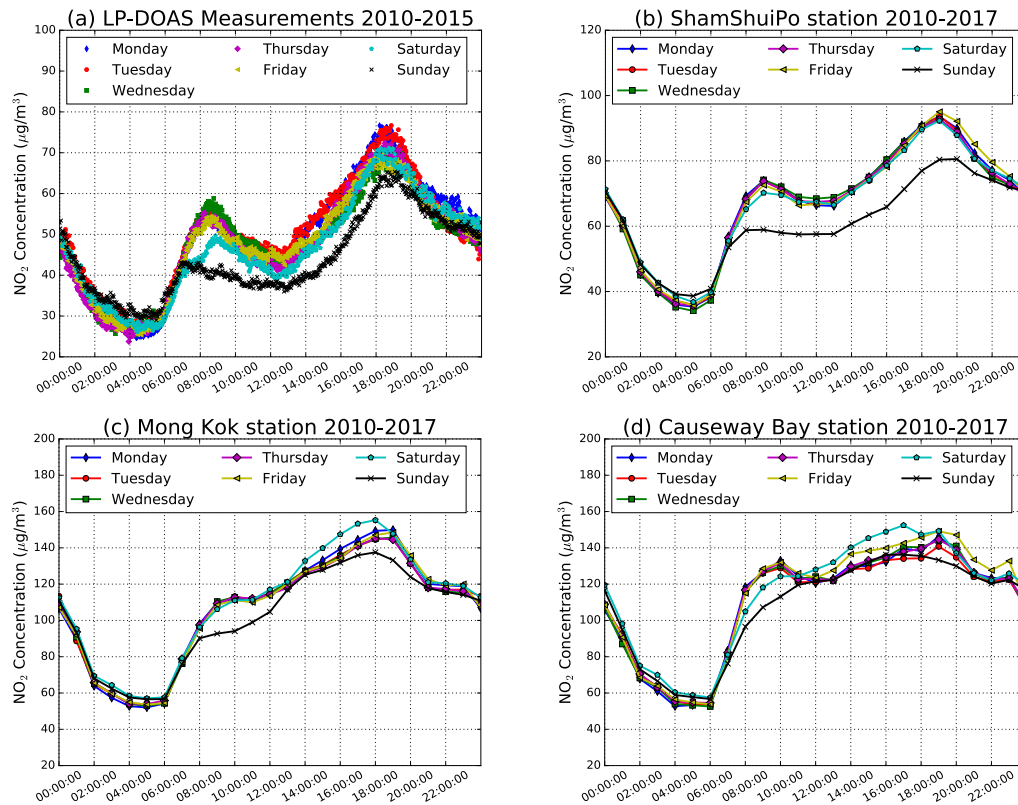
Figure 5.9: (a) shows the five years average diurnal cycle of NO$_2$ of each day of the week measured by LP DOAS.The seven years average diurnal cycle of NO$_2$ of each day of the week measured by EPD (b) Sham Shui Po station, (c) Mong Kok station and (d) Causeway Bay station.
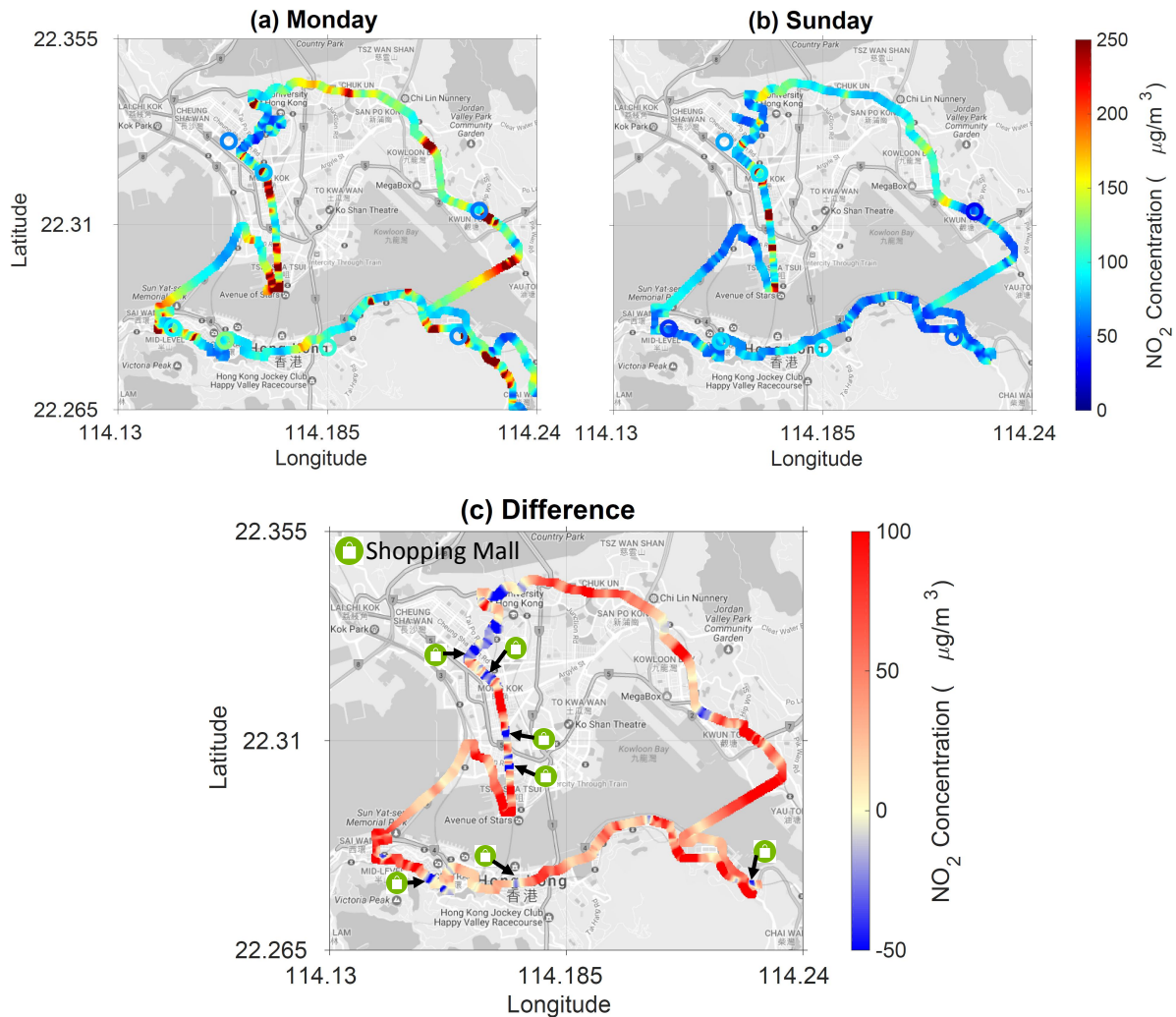
Figure 5.10: Mobile CE DOAS measurement of on-road NO$_2$ on (a) Monday (6th Mar 2017) and (b) Sunday (5th Mar 2017). Coinciding NO$_2$ concentration measured by the 7 EPD stations are shown on the map as circle markers using the same color scale for the concentrations and differences. (c) shows the differences between Monday and Sunday. The locations of shopping malls are marked.
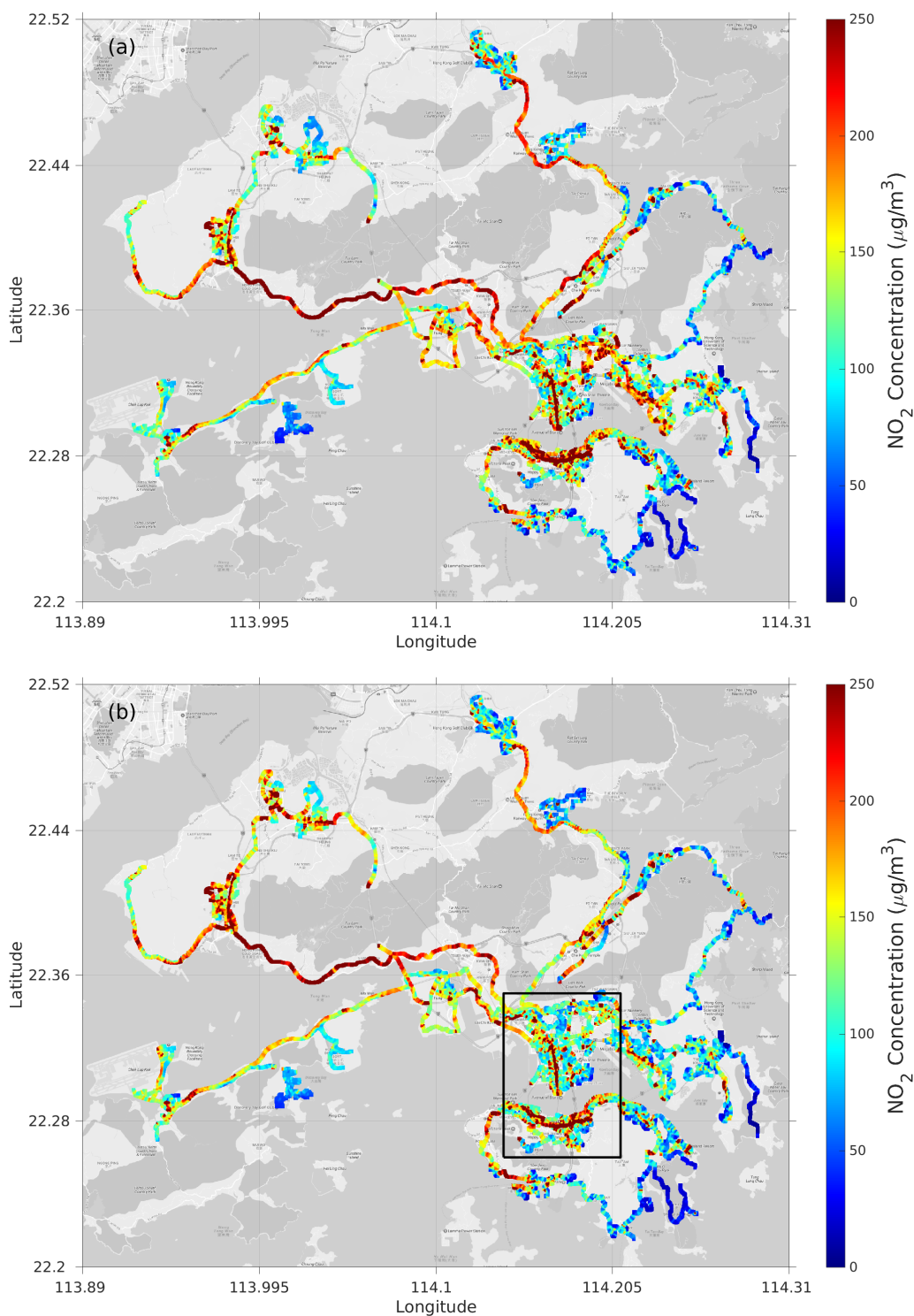
Figure 5.11: (a) Spatial distribution of NO$_2$ in Hong Kong measured by the mobile CE DOAS in 2010. (b) Normalized spatial distribution of NO$_2$ over Hong Kong measured by the mobile CE DOAS in 2010. The CE DOAS data is normalized by coinciding normalized LP DOAS data. The black box indicates the area of city center.

6 Conclusions and outlook

To achieve spatio-temporal NO_2 observation system in Munich, four measurement points were organized for setting up retro reflector arrays of LP DOAS instruments. Each LP DOAS telescope viewing direction was calibrated. Instrumental background was precisely corrected. The intercomparison study of LP DOAS, CE DOAS and CAPS showed that all instruments had good sensitivity and stability, and also confirmed good agreements between the instruments. However, the absolute concentration (ppbv) measured by different LP DOAS for different directions varied in a large range. It confirmed that NO_2 had a strong spatial distribution. Comparing the roof-level NO_2 measured by LP DOAS with CE DOAS ground-level measurements, elevated value with 22.7% higher on average was observed on the ground next to the street with a Pearson correlation of 91%. However, roadside measurements showed much lower correlation with roof measurements. Besides, much higher NO_2 was gained at roadside. Both results illustrated the rapid dilution effect of on-road emission on horizontal and vertical dimension. In addition, 15.7% of the estimated roadside NO_2 level exceeded the hourly WHO AQG, which could do great harm to pedestrian.

For further verification of the main NO_2 emission source in Munich, data in 2016 and 2017 from Lfu local air quality monitoring network and the city traffic information were analyzed. Traffic density of the city center for each day of the week showed similar weekend reduction and diurnal pattern with LP DOAS measurements. NO_2 level and traffic count of different air monitoring stations of the city center were compared. As results, similar diurnal pattern was presented. Lower NO_2 level was obtained at the station that had lower traffic density. Annual average diurnal variation of the traffic count and NO_2 both presented significant increase in 2017 in comparison to 2016.

The LP DOAS measurements during the OMI overpass time (12:30 – 14:30 UTC) were used to validate OMI satellite NO_2 measurements of Munich. Month-average data of the LP DOAS and OMI within 10 km radius of the LP DOAS had a high correlation coefficient of 0.85, showing that OMI measured reliable tendency of ground level NO_2. However, the OMI data were on average 7.4 ppbv lower than the LP DOAS measurements. This underestimation was mainly due to the a-priori NO_2 vertical profile used for the OMI retrieval and the conversion of OMI NO_2 VCDs to ground level mixing ratios.

A high resolution spatial distribution map of street level NO_2 made identifying city pollution hotspots possible. It could also provide valuable information for urban planning and the development of pollution control measures. For obtaining the pollutant information, on-road mobile CE DOAS measurements were successfully deployed in Hong Kong in December 2010 and March 2017, respectively. And the Munich campaign were performed in June and July 2016. The diurnal dependency caused by the different sampling time of mobile measurements was normalized through combining the continuous measurements

of LP DOAS. Furthermore, the algorithm implemented for Hong Kong campagin, which was developed to separate and filter the accumulation of local emissions due to traffic congestion, helped us focusing on the concentrations instead of the stopping frequency while the maps' comparison.

The mobile VCDs of Car MAX DOAS measurements were converted to ground mixing ratios using day-average NO_2 vertical profile measured by stationary 2-D MAX DOAS. Normalized on-road NO_2 distribution map of Car MAX DOAS showed similar observation with satellite OMI, which had high NO_2 in the city center and decrease from the center to the outer ring. However, the Car MAX DOAS data were much lower than the CE DOAS and CAPS measurements. This difference was mainly ascribed to conversion process: the stationary NO_2 vertical profile, which could have different shape with on-road measurements, was used for the conversion of car-based MAX DOAS NO_2 VCDs to ground level mixing ratios. Meanwhile, the lowest layer of the stationary MAX DOAS retrieval was extended from 30 m to 230 m above the ground level, which also led to an underestimation of the NO_2 level near the ground.

In Hong Kong, the long term trend and spatial variations of ambient, roadside and on-road NO_2 levels were investigated by analyzing on-road CE DOAS measurements together with LP DOAS and EPD monitor stations. The long term trend analysis showed that the ambient NO_2 level was descending with a rate of 2.5 % per year, while the roadside NO_2 level showed a strong decreasing trend with annual reduction rate ranging from 3.4 - 4.9 %. This observation matched with the mobile measurement results that on-road NO_2 was in general reduced by 20 - 50 % between 2010 and 2017. The changes of the operational strategies of the major franchised bus company in Hong Kong could be revealed by the enhancements of NO_2 level observed at locations close to metro stations. In addition, a rising trend of NO_2/NO_x ratio was observed in both roadside and ambient monitor data. This was mainly subjected to the reduction of vehicle emissions which typically associated with NO_2/NO_x ratio. Increasing O_3 concentration also contributed to the reduction of NO_2 level in the past few years in Hong Kong.

The temporal emission characteristic of different districts in Hong Kong were investigated using mobile measurements taken on different days of the week. The weekend reduction rate of on-road measurements was much higher than the long term ambient / roadside observation of LP DOAS and EPD monitoring stations. By analyzing the spatial pattern of the weekend reduction effect, it presented that the NO_2 levels of most residential districts were reduced on Sunday while commercial areas showed a rather constant NO_2 level throughout the week.

The mobile CE DOAS measurements presented in this study offered a full-scaled perception for the local emission of on-road NO_2 characteristics in Munich and Hong Kong. Simultaneously, these spatial distribution measurement results are also important for chemical transport model validations and assessment of human health effects.

List of Figures

List of Abbreviations

2-D	Two Dimensional
3-D	Three Dimensional
AOD	Aerosol Optical Depth
AMF	Air Mass Factor
APEX	Airborne Prism EXperiment
AQG	Air Quality Guideline
AQO	Air Quality Objectives
CAPS	Cavity attenuated phase shift spectroscopy
CCD	Charge Coupled Device
CEAS	Cavity Enhanced Absorption Spectroscopy
CE DOAS	Cavity Enhanced Differential Optical Absorption Spectroscopy
CL	ChemiLuminescence
COD	Cloud Optical Depths
CRDS	Cavity Ring-Down Spectroscopy
CTM	Chemical Transport Model
DAMF	Differential box Air Mass Factor
DC	Direct Current
DOAS	Differential Optical Absorption Spectroscopy
DSCD	Differential Slant Column Density
EOS	Earth Observing System
EPD	Environmental Protection Department
FTIR	Fourier Transform Infrared
FWHM	Full width Half Maximum
GMI	Global Modeling Initiative
GFED3	Global Fire Emissions Database version 3
GOME	Global Ozone Monitoring Experiment
ILAS	Improved Limb Atmospheric Spectrometer
LED	Light Emitting Diode
LEZ	Low Emission Zones
LfU	Bavarian Environment Agency
LMU	Ludwig Maximilian University
LP DOAS	Long Path Differential Optical Absorption Spectroscopy
MAX DOAS	Multi-AXis Differential Optical Absorption Spectroscopy
MIM	Meteorological Institute Munich
NA	Numerical Aperture
NASA	National Aeronautics and Space Administration
NDIR	Non-Dispersive InfraRed

List of Abbreviations

NOAA	National Oceanic and Atmospheric Administration
OMI	Ozone Monitoring Instrument
OSIRIS	Optical Spectrograph and InfraRed Imager System
PC	Personal Computer
PM	Particulate Matters
RACM	Regional Atmospheric Chemistry Modeling
SCD	Slant Column Density
SCIAMACHY	SCanning Imaging Absorption spectroMeter for Atmospheric CHartographY
SPv3	Standard Product Version 3
TUM	Technical University Munich
UCX	Universal tropospheric-stratospheric Chemistry eXtension
UV	Ultra-Violet
VCD	Vertical Column Density
WMO	World Meteorological Organization
WHO	World Health Organization
YRD	Yantze River Delta
ZSL DOAS	Zenith Scattered Light Differential Optical Absorption Spectroscopy

Appendix

All relevant python and matlab scripts for analysis are saved in the cluser of MIM Institute at the path of '\project\meteo\ag-wenig\Dragon2\ScriptsYing'. The file named 'LP_readdata.py' is for loading the LP DOAS data. The file named 'Stopeffect_minusmap.m' is for the comparison of two different maps. It also includes the function for filtering out the NO_2 accumulation data measured at traffic lights. The file named 'Normcut-fit_iterate.py' is for diurnal effect normalization which includes several functions, e.g. NaN value filter, error weighted linear regression function, iterate linear fit function.

Bibliography

Atkinson, R., Baulch, D., Cox, R., Hampson Jr, R., Kerr, J., Rossi, M., and Troe, J. (1997). Evaluated kinetic, photochemical and heterogeneous data for atmospheric chemistry: Supplement V. IUPAC subcommittee on gas kinetic data evaluation for atmospheric chemistry. Journal of Physical and Chemical Reference Data, 26(3):521–1011.

Axelson, H., Galle, B., Gustavson, K., Ragnarsson, P., and Rudin, M. (1990). A transmitting/receiving telescope for doas-measurements using retroreflector technique. Optical Remote Sensing of the Atmosphere, 4:641–644.

Axelsson, H., Galle, B., Gustavsson, K., Ragnarsson, P., and Rudi, M. (1990). A transmitting/receiving telescope for DOAS measurements using retro-reflector technique. Dig. Top. Meet. Opt. Remote Sens. Atmos., OSA, 4:641–644.

Baldocchi, D., Falge, E., Gu, L., Olson, R., Hollinger, D., Running, S., Anthoni, P., Bernhofer, C., Davis, K., Evans, R., et al. (2001). Fluxnet: A new tool to study the temporal and spatial variability of ecosystem-scale carbon dioxide, water vapor, and energy flux densities. Bulletin of the American Meteorological Society, 82(11):2415–2434.

Ball, S. M. and Jones, R. L. (2003). Broad-band cavity ring-down spectroscopy. Chemical reviews, 103(12):5239–5262.

Ban-Weiss, G. A., McLaughlin, J. P., Harley, R. A., Lunden, M. M., Kirchstetter, T. W., Kean, A. J., Strawa, A. W., Stevenson, E. D., and Kendall, G. R. (2008). Long-term changes in emissions of nitrogen oxides and particulate matter from on-road gasoline and diesel vehicles. Atmospheric Environment, 42(2):220–232.

Barker, K., Cambi, F., Catcott, E., Chambers, L. A., Halliday, E., Hasegawa, A., Heimann, H., Jammet, H., Katz, M., Leclerc, E., McCabe, L. C., Macfarlane, W. A., Parker, A., Rose, A. H., Stenburg, R. L., Stephan, D. G., Taylor, J. R., Thomas, M. D., Wexler, H., Organization, W. H., et al. (1961). Air pollution/contributors, k. barker...[et al.]. In Air pollution/contributors, K. Barker...[et al.]. Geneva : World Health Organization.

Beer, A. (1852). Bestimmung der absorption des rothen lichts in farbigen flussigkeiten. Ann. Physik, 162:78–88.

Bibliography

Berden, G., Peeters, R., and Meijer, G. (2000). Cavity ring-down spectroscopy: Experimental schemes and applications. International Reviews in Physical Chemistry, 19(4):565–607.

Bey, I., Jacob, D. J., Yantosca, R. M., Logan, J. A., Field, B. D., Fiore, A. M., Li, Q., Liu, H. Y., Mickley, L. J., and Schultz, M. G. (2001). Global modeling of tropospheric chemistry with assimilated meteorology: Model description and evaluation. Journal of Geophysical Research: Atmospheres, 106(D19):23073–23095.

Bobrowski, N. and Platt, U. (2007). So2/bro ratios studied in five volcanic plumes. Journal of Volcanology and Geothermal Research, 166(3-4):147–160.

Bond, D. W., Zhang, R., Tie, X., Brasseur, G., Huffines, G., Orville, R. E., and Boccippio, D. J. (2001). NO_x production by lightning over the continental United States. Journal of Geophysical Research: Atmospheres, 106(D21):27701–27710.

Bond, T. C., Bhardwaj, E., Dong, R., Jogani, R., Jung, S., Roden, C., Streets, D. G., and Trautmann, N. M. (2007). Historical emissions of black and organic carbon aerosol from energy-related combustion, 1850–2000. Global Biogeochemical Cycles, 21(2).

Bouguer, P. (1729). Essai d'optique sur la gradation de la lumière. chez Claude Jombert, ruë S. Jacques, au coin de la ruë des Mathurins, à l'Image Notre-Dame.

Bovensmann, H., Burrows, J., Buchwitz, M., Frerick, J., Noël, S., Rozanov, V., Chance, K., and Goede, A. (1999). Sciamachy: Mission objectives and measurement modes. Journal of the atmospheric sciences, 56(2):127–150.

Brown, S., Stark, H., and Ravishankara, A. (2002). Cavity ring-down spectroscopy for atmospheric trace gas detection: application to the nitrate radical (no 3). Applied Physics B, 75(2-3):173–182.

Brunner, D., Savage, N., Jorba, O., Eder, B., Giordano, L., Badia, A., Balzarini, A., Baro, R., Bianconi, R., Chemel, C., et al. (2015). Comparative analysis of meteorological performance of coupled chemistry-meteorology models in the context of aqmeii phase 2. Atmospheric Environment, 115:470–498.

Bucsela, E. J., Krotkov, N. A., Celarier, E. A., Lamsal, L. N., Swartz, W. H., Bhartia, P. K., Boersma, K. F., Veefkind, J. P., Gleason, J. F., and Pickering, K. E. (2013). A new stratospheric and tropospheric NO_2 retrieval algorithm for nadir-viewing satellite instruments: applications to OMI. Atmospheric Measurement Techniques, 6(10):2607–2626.

Burrows, J. P., Weber, M., Buchwitz, M., Rozanov, V., Ladstätter-Weißenmayer, A., Richter, A., DeBeek, R., Hoogen, R., Bramstedt, K., Eichmann, K.-U., et al. (1999). The global ozone monitoring experiment (gome): Mission concept and first scientific results. Journal of the Atmospheric Sciences, 56(2):151–175.

Carapellucci, R. and Giordano, L. (2013). The effect of diurnal profile and seasonal wind regime on sizing grid-connected and off-grid wind power plants. Applied Energy, 107:364–376.

Carslaw, D. C. (2005). Evidence of an increasing NO_2/NO_x emissions ratio from road traffic emissions. Atmospheric Environment, 39(26):4793–4802.

Chan, K., Hartl, A., Lam, Y., Xie, P., Liu, W., Cheung, H., Lampel, J., Pöhler, D., Li, A., Xu, J., Zhou, H., Ning, Z., and Wenig, M. (2015). Observations of tropospheric NO2 using ground based MAX-DOAS and OMI measurements during the Shanghai World Expo 2010. Atmospheric Environment, 119:45–58.

Chan, K., Wiegner, M., Wenig, M., and Pöhler, D. (2018). Observations of tropospheric aerosols and no2 in hong kong over 5years using ground based max-doas. Science of The Total Environment, 619-620:1545 – 1556.

Chan, K. L., Pöhler, D., Kuhlmann, G., Hartl, A., Platt, U., and Wenig, M. O. (2012). NO_2 measurements in hong kong using LED based long path differential optical absorption spectroscopy. Atmospheric Measurement Techniques, 5(5):901–912.

Chan, K. L., Wang, S., Liu, C., Zhou, B., Wenig, M. O., and Saiz-Lopez, A. (2017). On the summertime air quality and related photochemical processes in the megacity Shanghai, China. Science of The Total Environment, 580:974–983.

Chang, Y., Zou, Z., Deng, C., Huang, K., Collett, J. L., Lin, J., and Zhuang, G. (2016). The importance of vehicle emissions as a source of atmospheric ammonia in the megacity of Shanghai. Atmospheric Chemistry and Physics, 16(5):3577–3594.

Chaparro-Suarez, I., Meixner, F., and Kesselmeier, J. (2011). Nitrogen dioxide (no2) uptake by vegetation controlled by atmospheric concentrations and plant stomatal aperture. Atmospheric Environment, 45(32):5742 – 5750.

Cofala, J., Amann, M., Klimont, Z., Kupiainen, K., and Höglund-Isaksson, L. (2007). Scenarios of global anthropogenic emissions of air pollutants and methane until 2030. Atmospheric Environment, 41(38):8486–8499.

Cofala, J., Bertok, I., Borken-Kleefeld, J., Heyes, C., Klimont, Z., Rafaj, P., Sander, R., Schöpp, W., and Amann, M. (2012). Emissions of air pollutants for the world energy outlook 2012 energy scenarios.

Cox, P. M., Betts, R. A., Jones, C. D., Spall, S. A., and Totterdell, I. J. (2000). Acceleration of global warming due to carbon-cycle feedbacks in a coupled climate model. Nature, 408(6809):184.

Crutzen, P. J. and Arnold, F. (1986). Nitric acid cloud formation in the cold antarctic stratosphere: a major cause for the springtime 'ozone hole'. Nature, 324(6098):651–655.

Bibliography

Dallmann, T. R., Harley, R. A., and Kirchstetter, T. W. (2011). Effects of diesel particle filter retrofits and accelerated fleet turnover on drayage truck emissions at the port of oakland. Environmental science & technology, 45(24):10773–10779.

Duan, L., Yu, Q., Zhang, Q., Wang, Z., Pan, Y., Larssen, T., Tang, J., and Mulder, J. (2016). Acid deposition in Asia: Emissions, deposition, and ecosystem effects. Atmospheric Environment, 146:55–69. Acid Rain and its Environmental Effects: Recent Scientific Advances.

Düring, I., Bächlin, W., Ketzel, M., Baum, A., Friedrich, U., and Wurzler, S. (2011). A new simplified NO/NO_2 conversion model under consideration of direct NO_2-emissions. Meteorologische Zeitschrift, 20(1):67–73.

Eastham, S. D., Weisenstein, D. K., and Barrett, S. R. (2014). Development and evaluation of the unified tropospheric–stratospheric chemistry extension (ucx) for the global chemistry-transport model geos-chem. Atmospheric Environment, 89:52–63.

EDGAR4.2 (2011). Emission database for global atmospheric research (edgar), release version 4.2. Technical report, European Commission, Joint Research Centre (JRC) / Netherlands Environmental Assessment Agency (PBL). Technical Report MSU-CSE-00e2.

EEA (2017). Air quality in europe - 2017 report. Technical report, European Environment Agency. EEA Report No 13/2017.

Emde, C., Buras-Schnell, R., Kylling, A., Mayer, B., Gasteiger, J., Hamann, U., Kylling, J. I., Richter, B., Pause, C., Dowling, T., et al. (2016). The libradtran software package for radiative transfer calculations (version 2.0. 1).

Engeln, R., von Helden, G., Berden, G., and Meijer, G. (1996). Phase shift cavity ring down absorption spectroscopy. Chemical Physics Letters, 262(1):105 – 109.

EU emission standards (2007). European union emission standards for new light duty vehicles (passenger cars and light commercial vehicles). Directive 98/69/EC, DieselNet. Accessed: 2018-02-06.

Fiedler, S. E., Hese, A., and Ruth, A. A. (2003). Incoherent broad-band cavity-enhanced absorption spectroscopy. Chemical Physics Letters, 371(3-4):284–294.

Finlayson-Pitts, B. J. and Pitts Jr, J. N. (1999a). Chemistry of the upper and lower atmosphere: theory, experiments, and applications. Academic press.

Finlayson-Pitts, B. J. and Pitts Jr, J. N. (1999b). Chemistry of the upper and lower atmosphere: theory, experiments, and applications. Elsevier.

Franco, V., Sánchez, F. P., German, J., and Mock, P. (2014). Real-world exhaust emissions from modern diesel cars. communications, 49(30):847129–102.

Frankenberg, C., Platt, U., and Wagner, T. (2005). Iterative maximum a posteriori (imap)-doas for retrieval of strongly absorbing trace gases: Model studies for ch 4 and co 2 retrieval from near infrared spectra of sciamachy onboard envisat. Atmospheric Chemistry and Physics, 5(1):9–22.

Frins, E., Bobrowski, N., Osorio, M., Casaballe, N., Belsterli, G., Wagner, T., and Platt, U. (2014). Scanning and mobile multi-axis DOAS measurements of SO_2 and NO_2 emissions from an electric power plant in Montevideo, Uruguay. Atmospheric Environment, 98:347–356.

Fu, X., Liu, J., Ban-Weiss, G. A., Zhang, J., Huang, X., Ouyang, B., Popoola, O., and Tao, S. (2017). Effects of canyon geometry on the distribution of traffic-related air pollution in a large urban area: Implications of a multi-canyon air pollution dispersion model. Atmospheric Environment, 165:111–121.

Gratsea, M., Vrekoussis, M., Richter, A., Wittrock, F., Schönhardt, A., Burrows, J., Kazadzis, S., Mihalopoulos, N., and Gerasopoulos, E. (2016). Slant column MAX-DOAS measurements of nitrogen dioxide, formaldehyde, glyoxal and oxygen dimer in the urban environment of Athens. Atmospheric Environment, 135:118–131.

Guenther, A., Jiang, X., Heald, C., Sakulyanontvittaya, T., Duhl, T., Emmons, L., and Wang, X. (2012). The model of emissions of gases and aerosols from nature version 2.1 (megan2. 1): an extended and updated framework for modeling biogenic emissions.

Guo, S., Hu, M., Guo, Q., Zhang, X., Schauer, J., and Zhang, R. (2013). Quantitative evaluation of emission controls on primary and secondary organic aerosol sources during beijing 2008 olympics. Atmospheric Chemistry and Physics, 13(16):8303–8314.

Haagen-Smit, A. J. (1952). Chemistry and physiology of los angeles smog. Industrial & Engineering Chemistry, 44(6):1342–1346.

Harris, G. W., Carter, W. P., Winer, A. M., Pitts, J. N., Platt, U., and Perner, D. (1982). Observations of nitrous acid in the los angeles atmosphere and implications for predictions of ozone-precursor relationships. Environmental science & technology, 16(7):414–419.

Hartl, A., Song, B., and Pundt, I. (2006). 2-d reconstruction of atmospheric concentration peaks from horizontal long path doas tomographic measurements: parametrisation and geometry within a discrete approach. Atmospheric Chemistry and Physics, 6(3):847–861.

Henderson, S. B., Beckerman, B., Jerrett, M., and Brauer, M. (2007). Application of land use regression to estimate long-term concentrations of traffic-related nitrogen oxides and fine particulate matter. Environmental science & technology, 41(7):2422–2428.

Herbelin, J. M., McKay, J. A., Kwok, M. A., Ueunten, R. H., Urevig, D. S., Spencer, D. J., and Benard, D. J. (1980). Sensitive measurement of photon lifetime and true reflectances in an optical cavity by a phase-shift method. Appl. Opt., 19(1):144–147.

Bibliography

Hermans, C., Vandaele, A. C., Carleer, M., Fally, S., Colin, R., Jenouvrier, A., Coquart, B., and Mérienne, M.-F. (1999). Absorption cross-sections of atmospheric constituents: NO2, O2, and H2O. Environmental Science and Pollution Research, 6(3):151–158.

Hönninger, G., Leser, H., Sebastian, O., and Platt, U. (2004). Ground-based measurements of halogen oxides at the hudson bay by active longpath doas and passive max-doas. Geophysical research letters, 31(4).

Hönninger, G. and Platt, U. (2002). Observations of bro and its vertical distribution during surface ozone depletion at alert. Atmospheric Environment, 36(15-16):2481–2489.

Huan, L. and Kebin, H. (2012). Traffic optimization: A new way for air pollution control in china's urban areas. Environmental Science & Technology, 46(11):5660–5661. PMID: 22612715.

Huang, R.-J., Seitz, K., Buxmann, J., Pöhler, D., Hornsby, K., Carpenter, L., Platt, U., and Hoffmann, T. (2010a). In situ measurements of molecular iodine in the marine boundary layer: the link to macroalgae and the implications for o 3, io, oio and no x. Atmospheric Chemistry and Physics, 10(10):4823–4833.

Huang, R.-J., Zhang, Y., Bozzetti, C., Ho, K.-F., Cao, J.-J., Han, Y., Daellenbach, K. R., Slowik, J. G., Platt, S. M., Canonaco, F., et al. (2014). High secondary aerosol contribution to particulate pollution during haze events in China. Nature, 514(7521):218–222.

Huang, X.-F., He, L.-Y., Hu, M., Canagaratna, M., Sun, Y., Zhang, Q., Zhu, T., Xue, L., Zeng, L.-W., Liu, X.-G., et al. (2010b). Highly time-resolved chemical characterization of atmospheric submicron particles during 2008 beijing olympic games using an aerodyne high-resolution aerosol mass spectrometer. Atmospheric Chemistry and Physics, 10(18):8933–8945.

Irie, H., Takashima, H., Kanaya, Y., Boersma, K., Gast, L., Wittrock, F., Brunner, D., Zhou, Y., and Roozendael, M. V. (2011). Eight-component retrievals from ground-based max-doas observations. Atmospheric Measurement Techniques, 4(6):1027–1044.

Jacob, D. J., Crawford, J. H., Kleb, M. M., Connors, V. S., Bendura, R. J., Raper, J. L., Sachse, G. W., Gille, J. C., Emmons, L., and Heald, C. L. (2003). Transport and chemical evolution over the pacific (trace-p) aircraft mission: Design, execution, and first results. Journal of Geophysical Research: Atmospheres, 108(D20).

Jang, M. and Kamens, R. M. (2001). Characterization of secondary aerosol from the photooxidation of toluene in the presence of NO_x and 1-propene. Environmental Science & Technology, 35(18):3626–3639.

Jin, J., Ma, J., Lin, W., Zhao, H., Shaiganfar, R., Beirle, S., and Wagner, T. (2016). MAX-DOAS measurements and satellite validation of tropospheric NO2 and SO2 vertical column densities at a rural site of North China. Atmospheric Environment, 133:12–25.

Kang, J., Cho, B. C., and Lee, C.-B. (2010). Atmospheric transport of water-soluble ions (NO_3^-, NH_4^+ and nss-SO_4^{2-}) to the southern east sea (sea of japan). Science of The Total Environment, 408(11):2369 – 2377.

Katz, M., Organization, W. H., et al. (1969). Measurement of air pollutants: guide to the selection of methods.

Kaur, S., Nieuwenhuijsen, M., and Colvile, R. (2007). Fine particulate matter and carbon monoxide exposure concentrations in urban street transport microenvironments. Atmospheric Environment, 41(23):4781–4810.

Kašpar, J., Fornasiero, P., and Hickey, N. (2003). Automotive catalytic converters: current status and some perspectives. Catalysis Today, 77(4):419–449. Fundamentals of Catalysis and Applications to Environmental Problems.

Kebabian, P. L., Herndon, S. C., and Freedman, A. (2005). Detection of nitrogen dioxide by cavity attenuated phase shift spectroscopy. Analytical chemistry, 77(2):724–728.

Kebabian, P. L., Wood, E. C., Herndon, S. C., and Freedman, A. (2008). A practical alternative to chemiluminescence-based detection of nitrogen dioxide: Cavity attenuated phase shift spectroscopy. Environmental science & technology, 42(16):6040–6045.

Keeling, C. D., Bacastow, R. B., Bainbridge, A. E., Ekdahl Jr, C. A., Guenther, P. R., Waterman, L. S., and Chin, J. F. (1976). Atmospheric carbon dioxide variations at mauna loa observatory, hawaii. Tellus, 28(6):538–551.

Keuken, M., Roemer, M., and van den Elshout, S. (2009). Trend analysis of urban NO_2 concentrations and the importance of direct NO_2 emissions versus ozone/NOx equilibrium. Atmospheric Environment, 43(31):4780–4783. Urban Air Quality.

Kim, M., Kim, J., Wong, M. S., Yoon, J., Lee, J., Wu, D., Chan, P., Nichol, J. E., Chung, C.-Y., and Ou, M.-L. (2014). Improvement of aerosol optical depth retrieval over Hong Kong from a geostationary meteorological satellite using critical reflectance with background optical depth correction. Remote Sensing of Environment, 142:176–187.

Kirchstetter, T. W., Harley, R. A., Kreisberg, N. M., Stolzenburg, M. R., and Hering, S. V. (1999). On-road measurement of fine particle and nitrogen oxide emissions from light-and heavy-duty motor vehicles. Atmospheric Environment, 33(18):2955–2968.

Knight, A. W. and Greenway, G. M. (1994). Occurrence, mechanisms and analytical applications of electrogenerated chemiluminescence. a review. Analyst, 119(5):879–890.

Kraus, S. (2005). DOASIS A Framework Design for DOAS. PhD thesis, Combined Faculties for Mathematics and for Computer Science, University of Mannheim.

Krotkov, N. A., Lamsal, L. N., Celarier, E. A., Swartz, W. H., Marchenko, S. V., Bucsela, E. J., Chan, K. L., Wenig, M., and Zara, M. (2017). The version 3 OMI NO_2 standard product. Atmospheric Measurement Techniques, 10(9):3133–3149.

Bibliography

Krzyzanowski, M. and Cohen, A. (2008). Update of WHO air quality guidelines. Air Quality, Atmosphere & Health, 1(1):7–13.

Laepple, T., Knab, V., Mettendorf, K.-U., and Pundt, I. (2004). Longpath doas tomography on a motorway exhaust gas plume: numerical studies and application to data from the bab ii campaign. Atmospheric Chemistry and Physics, 4(5):1323–1342.

Lambert, J. H. (1760). Photometria sive de mensura et gradibus luminis, colorum et umbrae. Klett.

Langridge, J. M., Ball, S. M., and Jones, R. L. (2006). A compact broadband cavity enhanced absorption spectrometer for detection of atmospheric NO_2 using light emitting diodes. Analyst, 131(8):916–922.

Lau, C. F., Rakowska, A., Townsend, T., Brimblecombe, P., Chan, T. L., Yam, Y. S., Močnik, G., and Ning, Z. (2015). Evaluation of diesel fleet emissions and control policies from plume chasing measurements of on-road vehicles. Atmospheric Environment, 122:171–182.

Lawther, P. J., Martin, A. E., Wilkins, E. T., Organization, W. H., et al. (1962). Epidemiology of air pollution: report on a symposium.

Lee, C., Kim, Y. J., Tanimoto, H., Bobrowski, N., Platt, U., Mori, T., Yamamoto, K., and Hong, C. S. (2005). High clo and ozone depletion observed in the plume of sakurajima volcano, japan. Geophysical Research Letters, 32(21).

Lee, H., Irie, H., Gu, M., Kim, J., and Hwang, J. (2011a). Remote sensing of tropospheric aerosol using UV MAX-DOAS during hazy conditions in winter: Utilization of O4 Absorption bands at wavelength intervals of 338–368 and 367–393 nm. Atmospheric Environment, 45(32):5760–5769.

Lee, H., Ryu, J., Kim, J., Noh, Y., and Yoon, Y. (2011b). Combined measurements of a UV mini MAX-DOAS system and a TX for retrieval of ambient trace gas mixing ratio: Comparisons with combined RTM and MAX-DOAS methods. Atmospheric Environment, 45(39):7218–7226.

Levelt, P., Van den Oord, G. H. J., Dobber, M., Malkki, A., Visser, H., de Vries, J., Stammes, P., Lundell, J., and Saari, H. (2006a). The ozone monitoring instrument. Geoscience and Remote Sensing, IEEE Transactions on, 44(5):1093–1101.

Levelt, P. F., van den Oord, G. H., Dobber, M. R., Malkki, A., Visser, H., de Vries, J., Stammes, P., Lundell, J. O., and Saari, H. (2006b). The ozone monitoring instrument. IEEE Transactions on geoscience and remote sensing, 44(5):1093–1101.

LfU (2015). Untersuchung der räumlichen verteilung der nox-belastung im umfeld von vorhandenen, hochbelasteten luftmessstationen, abschlussbericht. Technical report, Bayerisches Landesamt für Umwelt.

Li, X., Brauers, T., Hofzumahaus, A., Lu, K., Li, Y., Shao, M., Wagner, T., and Wahner, A. (2013). Max-doas measurements of no 2, hcho and chocho at a rural site in southern china. Atmospheric Chemistry and Physics, 13(4):2133–2151.

Likens, G. E., Driscoll, C. T., and Buso, D. C. (1996). Long-term effects of acid rain: response and recovery of a forest ecosystem. Science, 272(5259):244–246.

Lodge, J. P., Evelyn, J., and Barr, R. (1969). The Smoke of London; Two Prophecies: Fumifugium; or, The Inconvenience of the Air and Smoke of London Dissipated. Maxwell Reprint Co, Elmsford, New York.

Logan, J. A. (1983). Nitrogen oxides in the troposphere: Global and regional budgets. Journal of Geophysical Research: Oceans, 88(C15):10785–10807.

Longley, I., Somervell, E., and Gray, S. (2015). Roadside increments in PM_{10}, nox and no_2 concentrations observed over 2 months at a major highway in New Zealand. Air Quality, Atmosphere & Health, 8(6):591–602.

Malhi, Y. and Grace, J. (2000). Tropical forests and atmospheric carbon dioxide. Trends in Ecology & Evolution, 15(8):332–337.

Marchenko, S., Krotkov, N. A., Lamsal, L. N., Celarier, E. A., Swartz, W. H., and Bucsela, E. J. (2015). Revising the slant column density retrieval of nitrogen dioxide observed by the ozone monitoring instrument. Journal of Geophysical Research: Atmospheres, 120(11):5670–5692. 2014JD022913.

Merten, A., Tschritter, J., and Platt, U. (2011). Design of differential optical absorption spectroscopy long-path telescopes based on fiber optics. Applied optics, 50(5):738–754.

Min, K.-E., Washenfelder, R. A., Dubé, W. P., Langford, A. O., Edwards, P. M., Zarzana, K. J., Stutz, J., Lu, K., Rohrer, F., Zhang, Y., and Brown, S. S. (2016). A broadband cavity enhanced absorption spectrometer for aircraft measurements of glyoxal, methylglyoxal, nitrous acid, nitrogen dioxide, and water vapor. Atmospheric Measurement Techniques, 9(2):423–440.

Mock, P. (2014). European vehicle market statistics. Pocketbook: Lugano, Switzerland.

Molina, L. and Molina, M. (1986). Absolute absorption cross sections of ozone in the 185-to 350-nm wavelength range. Journal of Geophysical Research: Atmospheres, 91(D13):14501–14508.

Muilwijk, C., Schrijvers, P., Wuerz, S., and Kenjereš, S. (2016). Simulations of photochemical smog formation in complex urban areas. Atmospheric Environment, 147:470–484.

Murtagh, D., Frisk, U., Merino, F., Ridal, M., Jonsson, A., Stegman, J., Witt, G., Eriksson, P., Jiménez, C., Megie, G., et al. (2002). An overview of the odin atmospheric mission. Canadian Journal of Physics, 80(4):309–319.

Bibliography

Ning, Z., Wubulihairen, M., and Yang, F. (2012). PM, NO$_x$ and butane emissions from on-road vehicle fleets in Hong Kong and their implications on emission control policy. Atmospheric Environment, 61:265–274.

NOAA (2018). Earth system research laboratory. `ftp://ftp.cmdl.noaa.gov/ccg/co2/trends/co2_annmean_mlo.txt`.

Olaguer, E. P., Stutz, J., Erickson, M. H., Hurlock, S. C., Cheung, R., Tsai, C., Colosimo, S. F., Festa, J., Wijesinghe, A., and Neish, B. S. (2017). Real time measurement of transient event emissions of air toxics by tomographic remote sensing in tandem with mobile monitoring. Atmospheric Environment, 150:220–228.

Pastorello, C. and Melios, G. (2016). Explaining road transport emissions: a non-technical guide. Technical report, European Environment Agency.

Perner, D. and Platt, U. (1980). Absorption of light in the atmosphere by collision pairs of oxygen (o2) 2. Geophysical Research Letters, 7(12):1053–1056.

Pfeilsticker, K. and Platt, U. (1994). Airborne measurements during the arctic stratospheric experiment: observation of o3 and no2. Geophysical research letters, 21(13):1375–1378.

Platt, U., Meinen, J., Pöhler, D., and Leisner, T. (2009). Broadband cavity enhanced differential optical absorption spectroscopy (CE-DOAS) – applicability and corrections. Atmospheric Measurement Techniques, 2(2):713–723.

Platt, U., Perner, D., Schröder, J., Kessler, C., and Toennissen, A. (1981). The diurnal variation of no3. Journal of Geophysical Research: Oceans, 86(C12):11965–11970.

Rakowska, A., Wong, K. C., Townsend, T., Chan, K. L., Westerdahl, D., Ng, S., Močnik, G., Drinovec, L., and Ning, Z. (2014). Impact of traffic volume and composition on the air quality and pedestrian exposure in urban street canyon. Atmospheric Environment, 98(Supplement C):260–270.

Rodgers, C. D. (2000). Inverse methods for atmospheric sounding: theory and practice, volume 2. World scientific.

Rothman, L., Barbe, A., Benner, D. C., Brown, L., Camy-Peyret, C., Carleer, M., Chance, K., Clerbaux, C., Dana, V., Devi, V., Fayt, A., Flaud, J.-M., Gamache, R., Goldman, A., Jacquemart, D., Jucks, K., Lafferty, W., Mandin, J.-Y., Massie, S., Nemtchinov, V., Newnham, D., Perrin, A., Rinsland, C., Schroeder, J., Smith, K., Smith, M., Tang, K., Toth, R., Auwera, J. V., Varanasi, P., and Yoshino, K. (2003). The HITRAN molecular spectroscopic database: edition of 2000 including updates through 2001. Journal of Quantitative Spectroscopy and Radiative Transfer, 82(1):5–44. The HITRAN Molecular Spectroscopic Database: Edition of 2000 Including Updates of 2001.

Rothman, L. S., Gordon, I. E., Barbe, A., Benner, D. C., Bernath, P. F., Birk, M., Boudon, V., Brown, L. R., Campargue, A., Champion, J.-P., et al. (2009). The hitran 2008 molecular spectroscopic database. Journal of Quantitative Spectroscopy and Radiative Transfer, 110(9-10):533–572.

Rotman, D. A., Tannahill, J. R., Kinnison, D. E., Connell, P. S., Bergmann, D., Proctor, D., Rodriguez, J. M., Lin, S. J., Rood, R. B., Prather, M. J., Rasch, P. J., Considine, D. B., Ramaroson, R., and Kawa, S. R. (2001). Global modeling initiative assessment model: Model description, integration, and testing of the transport shell. Journal of Geophysical Research: Atmospheres, 106(D2):1669–1691.

Russo, R. S., Talbot, R. W., Dibb, J. E., Scheuer, E., Seid, G., Jordan, C. E., Fuelberg, H. E., Sachse, G. W., Avery, M. A., Vay, S. A., Blake, D. R., Blake, N. J., Atlas, E., Fried, A., Sandholm, S. T., Tan, D., Singh, H. B., Snow, J., and Heikes, B. G. (2003). Chemical composition of asian continental outflow over the western pacific: Results from transport and chemical evolution over the pacific (trace-p). Journal of Geophysical Research: Atmospheres, 108(D20):n/a–n/a. 8804.

Sasano, Y., Suzuki, M., Yokota, T., and Kanzawa, H. (1999). Improved limb atmospheric spectrometer (ilas) for stratospheric ozone layer measurements by solar occultation technique. Geophysical research letters, 26(2):197–200.

Seinfeld, J. H. and Pandis, S. N. (2012). Atmospheric chemistry and physics: from air pollution to climate change. John Wiley & Sons.

Serdyuchenko, A., Gorshelev, V., Weber, M., Chehade, W., and Burrows, J. (2014). High spectral resolution ozone absorption cross-sections–part 2: Temperature dependence. Atmospheric Measurement Techniques, 7(2):625–636.

Sinreich, R., Volkamer, R., Filsinger, F., Frieß, U., Kern, C., Platt, U., Sebastián, O., and Wagner, T. (2007). Max-doas detection of glyoxal during icartt 2004. Atmospheric Chemistry and Physics, 7(5):1293–1303.

Solomon, S., Schmeltekopf, A. L., and Sanders, R. W. (1987). On the interpretation of zenith sky absorption measurements. Journal of Geophysical Research: Atmospheres, 92(D7):8311–8319.

Stevens, C. (1987). The $NO/NO_2/O_3$ photostationary state and rate of photolysis of NO_2 in central Johannesburg. Atmospheric Environment (1967), 21(4):799–805.

Stutz, J., Alicke, B., Ackermann, R., Geyer, A., White, A., and Williams, E. (2004). Vertical profiles of no3, n2o5, o3, and nox in the nocturnal boundary layer: 1. observations during the texas air quality study 2000. Journal of Geophysical Research: Atmospheres, 109(D12).

Bibliography

Stutz, J., Hurlock, S. C., Colosimo, S. F., Tsai, C., Cheung, R., Festa, J., Pikelnaya, O., Alvarez, S., Flynn, J. H., Erickson, M. H., and Olaguer, E. P. (2016). A novel dual-LED based long-path DOAS instrument for the measurement of aromatic hydrocarbons. Atmospheric Environment, 147:121–132.

Stutz, J. and Platt, U. (1996). Numerical analysis and estimation of the statistical error of differential optical absorption spectroscopy measurements with least-squares methods. Applied Optics, 35(30):6041–6053.

Thalman, R. and Volkamer, R. (2010). Inherent calibration of a blue LED-CE-DOAS instrument to measure iodine oxide, glyoxal, methyl glyoxal, nitrogen dioxide, water vapour and aerosol extinction in open cavity mode. Atmospheric Measurement Techniques, 3(6):1797–1814.

Thalman, R. and Volkamer, R. (2013). Temperature dependent absorption cross-sections of o 2–o 2 collision pairs between 340 and 630 nm and at atmospherically relevant pressure. Physical chemistry chemical physics, 15(37):15371–15381.

Tian, L., Hossain, S. R., Lin, H., Ho, K. F., Lee, S. C., and Yu, I. T. S. (2011). Increasing trend of primary NO_2 exhaust emission fraction in Hong Kong. Environmental Geochemistry and Health, 33(6):623–630.

UBA (2017). Air quality 2016 (preliminary evaluation). Technical report, Umweltbundesamt (German Environment Agency). Jan.2017.

Van der Werf, G. R., Randerson, J. T., Giglio, L., Collatz, G., Mu, M., Kasibhatla, P. S., Morton, D. C., DeFries, R., Jin, Y. v., and van Leeuwen, T. T. (2010). Global fire emissions and the contribution of deforestation, savanna, forest, agricultural, and peat fires (1997–2009). Atmospheric Chemistry and Physics, 10(23):11707–11735.

Vandaele, A. C., Hermans, C., Fally, S., Carleer, M., Colin, R., Mérienne, M.-F., Jenouvrier, A., and Coquart, B. (2002). High-resolution fourier transform measurement of the NO_2 visible and near-infrared absorption cross sections: Temperature and pressure effects. Journal of Geophysical Research: Atmospheres, 107(D18):ACH 3–1–ACH 3–12. 4348.

Vandaele, A. C., Hermans, C., Simon, P. C., Carleer, M., Colin, R., Fally, S., Merienne, M.-F., Jenouvrier, A., and Coquart, B. (1998). Measurements of the no2 absorption cross-section from 42 000 cm- 1 to 10 000 cm- 1 (238–1000 nm) at 220 k and 294 k. Journal of Quantitative Spectroscopy and Radiative Transfer, 59(3-5):171–184.

VDI (2017a). Environmental meteorology, photolysis frequencies for calculating pollutant concentrations in the troposphere, Bd. 3783 part 18. VDI-Richtlinie.

VDI (2017b). Environmental meteorology, reaction mechanism for the determination of the nitrogen dioxide concentration, Bd. 3783 part 19. VDI-Richtlinie.

Veitel, H., Kromer, B., Mossner, M., and Platt, U. (2002). New techniques for measurements of atmospheric vertical trace gas profiles using doas. Environmental Science and Pollution Research, pages 17–26.

Venables, D. S., Gherman, T., Orphal, J., Wenger, J. C., and Ruth, A. A. (2006). High sensitivity in situ monitoring of NO_3 in an atmospheric simulation chamber using incoherent broadband cavity-enhanced absorption spectroscopy. Environmental science & technology, 40(21):6758–6763.

Volkamer, R., Spietz, P., Burrows, J., and Platt, U. (2005). High-resolution absorption cross-section of glyoxal in the UV–vis and IR spectral ranges. Journal of Photochemistry and Photobiology A: Chemistry, 172(1):35–46.

Wagner, T., Burrows, J., Deutschmann, T., Dix, B., Friedeburg, C. v., Frieß, U., Hendrick, F., Heue, K.-P., Irie, H., Iwabuchi, H., et al. (2007). Comparison of box-air-mass-factors and radiances for multiple-axis differential optical absorption spectroscopy (max-doas) geometries calculated from different uv/visible radiative transfer models. Atmospheric Chemistry and Physics, 7(7):1809–1833.

Wagner, T., Ibrahim, O., Shaiganfar, R., and Platt, U. (2010). Mobile max-doas observations of tropospheric trace gases. Atmospheric Measurement Techniques, 3(1):129–140.

Wang, M., Zhu, T., Zheng, J., Zhang, R., Zhang, S., Xie, X., Han, Y., and Li, Y. (2009a). Use of a mobile laboratory to evaluate changes in on-road air pollutants during the beijing 2008 summer olympics. Atmospheric Chemistry and Physics, 9(21):8247–8263.

Wang, S. X., Zhao, B., Cai, S. Y., Klimont, Z., Nielsen, C. P., Morikawa, T., Woo, J. H., Kim, Y., Fu, X., Xu, J. Y., Hao, J. M., and He, K. B. (2014). Emission trends and mitigation options for air pollutants in East Asia. Atmospheric Chemistry and Physics, 14(13):6571–6603.

Wang, T., Nie, W., Gao, J., Xue, L. K., Gao, X. M., Wang, X. F., Qiu, J., Poon, C. N., Meinardi, S., Blake, D., Wang, S. L., Ding, A. J., Chai, F. H., Zhang, Q. Z., and Wang, W. X. (2010). Air quality during the 2008 Beijing Olympics: secondary pollutants and regional impact. Atmospheric Chemistry and Physics, 10(16):7603–7615.

Wang, T. and Xie, S. (2009). Assessment of traffic-related air pollution in the urban streets before and during the 2008 beijing olympic games traffic control period. Atmospheric Environment, 43(35):5682–5690.

Wang, Y., Hao, J., McElroy, M. B., Munger, J. W., Ma, H., Chen, D., and Nielsen, C. P. (2009b). Ozone air quality during the 2008 Beijing Olympics: effectiveness of emission restrictions. Atmospheric Chemistry and Physics, 9(14):5237–5251.

Wang, Y., Lampel, J., Xie, P., Beirle, S., Li, A., Wu, D., and Wagner, T. (2017). Ground-based max-doas observations of tropospheric aerosols, no_2, so_2 and hcho in wuxi, china, from 2011 to 2014. Atmospheric Chemistry and Physics, 17(3):2189–2215.

Bibliography

Warneke, C., De Gouw, J. A., Holloway, J. S., Peischl, J., Ryerson, T. B., Atlas, E., Blake, D., Trainer, M., and Parrish, D. D. (2012). Multiyear trends in volatile organic compounds in los angeles, california: Five decades of decreasing emissions. Journal of Geophysical Research: Atmospheres, 117(D21).

Washenfelder, R. A., Langford, A. O., Fuchs, H., and Brown, S. S. (2008). Measurement of glyoxal using an incoherent broadband cavity enhanced absorption spectrometer. Atmospheric Chemistry and Physics, 8(24):7779–7793.

Wenig, M. O., Cede, A., Bucsela, E., Celarier, E., Boersma, K., Veefkind, J., Brinksma, E., Gleason, J., and Herman, J. (2008). Validation of omi tropospheric no2 column densities using direct-sun mode brewer measurements at nasa goddard space flight center. Journal of Geophysical Research: Atmospheres, 113(D16).

Wesely, M. and Hicks, B. (2000). A review of the current status of knowledge on dry deposition. Atmospheric environment, 34(12-14):2261–2282.

Westerdahl, D., Fruin, S., Sax, T., Fine, P. M., and Sioutas, C. (2005). Mobile platform measurements of ultrafine particles and associated pollutant concentrations on freeways and residential streets in Los Angeles. Atmospheric Environment, 39(20):3597–3610.

Wilkins, E. (1954). Air pollution and the london fog of december, 1952. Journal of the Royal Sanitary Institute, 74(1):1–21.

Zhang, Q., Streets, D. G., Carmichael, G. R., He, K., Huo, H., Kannari, A., Klimont, Z., Park, I., Reddy, S., Fu, J., et al. (2009a). Asian emissions in 2006 for the nasa intex-b mission. Atmospheric Chemistry and Physics, 9(14):5131–5153.

Zhang, Q., Streets, D. G., Carmichael, G. R., He, K. B., Huo, H., Kannari, A., Klimont, Z., Park, I. S., Reddy, S., Fu, J. S., Chen, D., Duan, L., Lei, Y., Wang, L. T., and Yao, Z. L. (2009b). Asian emissions in 2006 for the nasa intex-b mission. Atmospheric Chemistry and Physics, 9(14):5131–5153.

Zhang, R., Tie, X., and Bond, D. W. (2003a). Impacts of anthropogenic and natural nox sources over the us on tropospheric chemistry. Proceedings of the National Academy of Sciences, 100(4):1505–1509.

Zhang, R., Tie, X., and Bond, D. W. (2003b). Impacts of anthropogenic and natural NO_x sources over the U.S. on tropospheric chemistry. Proceedings of the National Academy of Sciences, 100(4):1505–1509.

Zhang, X., Wang, Y., Lin, W., Zhang, Y., Zhang, X., Zhao, P., Yang, Y., Wang, J., Hou, Q., Che, H., et al. (2009c). Changes of atmospheric composition and optical properties over beijing–2008 olympic monitoring campaign. Bulletin of the American Meteorological Society, 90(11):1633–1651.

Zhang, Z., Zhang, S., and Zhang, X. (2005). Recent developments and applications of chemiluminescence sensors. Analytica Chimica Acta, 541(1):37–46. Liquid Phase Chemiluminescence.

Zhu, Y., Chan, K. L., Lam, Y. F., Horbanski, M., Pöhler, D., Boll, J., Lipkowitsch, I., Ye, S., and Wenig, M. (2018). Analysis of spatial and temporal patterns of on-road NO_2 concentrations in Hong Kong. Atmospheric Measurement Techniques Discussions, 2018:1–25.

Acknowledgment

It would not have been possible to finish this thesis without the help and support of many nice people around me, to only some of whom I can give particular mention here.

First and foremost, I offer my sincerest gratitude to my supervisor Prof. Dr. Mark Wenig, who supported and trusted me in this project and introduced me to the exciting world of the DOAS. He has been always there for me throughout my PhD study with his patience, encouragement and brilliant ideas whilst allowing me the room to work in my own way. His wisdom, knowledge, passion in research, commitment to the highest scientific standards motivated me all the time.

Many thanks to Ka Lok Chan and Denis Pöhler for teaching me detailed DOAS instrumental operations and giving me a lot of valuable advices about this study.

I am also indebted and thankful to my colleagues, Markus Garhammer, Anton Lex and Seefeldner Meinhard, who help me a lot on the organization of measurement campaigns and the equipments design.

I would also like to express my gratitude to Prof. Dr-ing. Jia Chen for kindly accepting the appointment as co-supervisor for this thesis.

Special thanks go to our group and office mates, Annette Schütt, Ivo Lipkowitsch, Johannes Boll, and Sheng Ye, for the open discussions, where I always learnt something new.

I am also indebted and thankful to Yuefei Zeng, Heinz Lösslein, and Robert Redl for their kindness and technical supports in computer.

I appreciate Prof. Dr. Jörg Schreiber, Prof. Dr. Joachim Rädler, Prof. Dr. Jochen Weller, and Prof. Dr. Hartmut Zohm for joining my committee to evaluate my Ph.D. work.

I am grateful to the financial support of Chinese Scholarship Council, and equally grateful to LMU for supporting my Ph.D. study with a variety of resources.

I would like to thank all my friends for sharing with me many happy moments and regulating the balance between work and life.

Last, but not least I would like to thank my family for their constant support, encouragement and endless love throughout as always. Especially, I would like to thank Ye Tuo, the person who is always there to support me and share my feelings and experiences with endless patience.

München, 07.2018   *Ying Zhu*